Generation of Photon Pairs in Fiber Microcouplers

Xinru Cheng

A thesis submitted to the
Faculty of Graduate and Postdoctoral Studies
under the supervision of Jeff S. Lundeen
in partial fulfillment of the requirements for the
MSc degree in Physics

Department of Physics
Faculty of Science
University of Ottawa

Abstract

Due to its inherent stability and compactness, integrated optics can allow for experimental complexity not currently achievable with bulk optics. This opens up the possibility for large-scale quantum technological applications, such as quantum communication networks and quantum information processing. Quantum information processing relies on efficient sources of entangled photon pairs. Most demonstrations in integrated photonics so far have featured the on-chip manipulation of photon states using a free-space bulk-optic source of photons [1,2]. This has the drawback of introducing loss due to the spatial mode mismatch between waveguide modes of the chip and modes of the produced photons. In this way, loss limits the number of photons that are simultaneously carried in the integrated optical device, and thus limits the number of qubits. One way to avoid this loss is to generate the photons in another waveguide device. This can be done through, for example, spontaneous four-wave mixing (SFWM). In this third-order nonlinear process, two pump photons spontaneously scatter off each other to create two photons of two new frequencies, satisfying momentum and energy conservation. This has been studied in birefringent optical fibers [3] and photonic crystal fibers [38].

In this work, we investigate the SFWM generation of photons in a waveguide coupler comprised of two touching tapered optical fibers, which we call a microcoupler. The two silica fibers are kept in contact and tapered to be 1 micron in diameter in the 10 cm long uniform interaction region. This device has three main advantages over a standard telecom 2x2 fiber coupler. 1) The small mode area enhances the photon generation rate; 2) The microcoupler supports four modes which is the minimum number required for two-photon entanglement. So in principle the device should be able to produce polarization-entangled photon pairs; 3) The strong waveguide-waveguide coupling and waveguide dispersion (due to the tapering) forces the photons to be far in wavelength from the background light around the pump. We present the 28 allowed phasematching processes for the microcoupler, as well as predict the frequencies of the generated photons. We report the first experimental observation of photon pairs produced via SFWM in a microcoupler. We also analyze the polarization state of the observed photons to figure out which phasematching processes are responsible for generating the photons. We expect to observe more photon pairs in future devices, with the ultimate goal being the generation of polarization-entangled photon pairs for integrated optics.

Contents

1 Introduction

Quantum information science has emerged over the past few decades as an exciting field that could significantly increase the speed and complexity of calculations currently achievable, as well as allow for more insight into the laws of nature on the microscopic scale. The fundamental information carriers in quantum information and quantum computing are called *qubits*, or quantum bits. They have been implemented in many different forms, including trapped atoms [4,5], quantum dots [6], and superconducting electrons [7], to name a few.

An all-optical quantum computer has been proven possible in 2001 [8], which means it is feasible to build a scalable quantum computer using only single-photon sources, linear optical circuits, and single-photon detectors. Linear optical circuits consist of optical elements that transform the field linearly, such as mirrors and beam splitters. Since then, there have been exciting breakthroughs in the development towards a scalable linear optical quantum computer. Heralding the powers of quantum computing using light has unique advantages compared to other material systems. Photons interact weakly with each other and with the environment, compared to other fundamental particles. This translates into robustness to noise, or decoherence, when single photons are used as qubits. This in turn helps preserve the fragile quantum properties of interest. Photonic qubits can also be encoded in multiple degrees of freedom, such as polarization, time-bin, path, and spatial modes.

Out of the various approaches that prepare and manipulate photons for optical quantum computing, integrated quantum optical systems are promising due to their inherent structural compactness and stability. This is a timely alternative to conventional bulk optics, since experiments in the latter area are becoming increasingly complex and less scalable in the past few years. The large device footprints of more complex quantum processing elements, such as networks of quantum gates or hyperentangled photon sources, would make them impractical for future large-scale quantum computing. The pioneering research in integrated quantum optics makes use of a series of analogies between integrated photonics and integrated electronics, in the form of on-chip sources, gates, and detectors, as well as mechanisms to couple from one microchip to another [2, 9]. These experiments are done on the silicon-on-insulator (SOI) platform, and utilize materials and methods from the more mature field of silicon photonics to develop the newer fields of quantum optics and quantum information.

There have been significant advances in integrated optics regarding both photon-processing quantum circuits and single-photon detectors, two out of the three main building blocks for an optical quantum computer. However, most of these integrated photonic experiments still use a free-space bulk photon source [1,2]. The photon pairs are often generated in a nonlinear medium such as a crystal, sent into free space, and then coupled into the integrated optics. The drawback of this bulk-optic source is the loss due to the mismatch between the spatial modes of the generated photons and the waveguide modes of the chip. This loss limits the number of photons in the integrated optical device, and thus limits the number of qubits that can be carried simultaneously. One solution to this problem caused by the mode mismatch is to generate photons in a fiber waveguide. In this case, the photons are generated in the fundamental modes of the fiber which are well matched with the waveguide modes of the optical chips. Photon pair-generation inside a fiber-based device makes use of nonlinear processes such as spontaneous four-wave mixing (SFWM). In spontaneous four-wave mixing, when two pump photons enter a nonlinear medium such as a fiber, two daughter photons of different wavelengths are generated. Photon-pair generation through spontaneous four-wave mixing in a photonic-crystal fiber (PCF) as well as in a standard birefringence fiber have already been studied [3,10]. In theory, for more complex fiber structures, this nonlinear process can also allow for the generation of entangled photon pairs.

When studying the quantum properties of light, we are often interested in using entangled photon pairs as the source. Entanglement, as a phenomenon that distinguishes quantum processes from classical ones, is also of fundamental interest, as it is still not completely understood. When an entangled photon pair is generated, the properties of the two photons are correlated. Simply put, correlation means if we measure the state of one photon, we can predict the state of its partner. Entangled photons exhibit stronger correlation compared to classically correlated photons, and measuring the state of one photon collapses that of the other. Each photon of an entangled pair behaves as a quantum bit, or *qubit*, and is used as the information carrier in quantum communication and quantum computing applications. In contrast with classical communication where one bit of information has a predetermined state, a qubit is in a superposition of two states, undetermined until measured. This allows each single photon to carry more information which hugely improves the speed and efficiency of calculations. It is also of interest to produce a large number of simultaneously entangled photons, as well as to generate single photons entangled in multiple degrees of freedom. A source

of entangled photon pairs is crucial for quantum information applications.

The most common method used to produce entangled photon pairs is called spontaneous down-conversion (SPDC), where one pump photon splits into two daughter photons that are identical in wavelength but with only half of the energy of the pump photon. This process is limited in the sense that the properties of the generated photon pairs are largely pre-determined by the properties of the nonlinear crystal, such as the crystal axis orientation and thickness. In comparison, for spontaneous four-wave mixing, it is possible to engineer the fiber-based device to produce photons with any of the desired properties such as wavelength and polarization. Having an efficient and versatile fiber-based source of entangled photon pairs would open up possibilities for testing many aspects of fundamental quantum optics, as well as allow for realizations of thought-experiments that are otherwise unattainable in bulk optics.

In this work we propose and test a novel design for a fiber-based device that generates single photon pairs for visible wavelengths via spontaneous four-wave mixing. We call this fiber-based waveguide a microcoupler. It is composed of two tapered single mode fibers kept in contact. The modes can couple strongly between the two cores. The small core diameter also promises higher SFWM efficiency. The unique structure of our microcoupler allows for four different modes which is the minimum requirement for entanglement. This is one step further in complexity compared to previous work with a single fiber supporting two polarization modes. Most fiber optics applications are designed for telecom wavelengths, but for quantum optics experiments we are more interested in the spectrum from ultraviolet to near-infrared. This is largely due to the drop off in detection efficiency for current single-photon detectors.

The ultimate goal of the research presented in this thesis is to create an efficient source of entangled photon pairs for integrated optics, as a step towards quantum waveguide networks and quantum information applications.

1.1 Thesis outline

This thesis is presented in six chapters, plus an appendix. In Chapter 2 we present the theoretical aspects of the project, starting from an overview of spontaneous four-wave mixing (SFWM), the mechanism we use to generate photon pairs in the microcoupler. We also use coupled-mode theory to get some intuition on the spatial modes supported by the microcoupler, and iden-

tify the 28 allowed phasematching processes. In Chapter 3 we present the numerical simulations used to calculate the effective refractive index for each mode, as well as highlight the phasematching plots used to predict the wavelengths of the generated photons. The plots for all the allowed phasematching processes are shown in the appendix. Chapter 4 presents the fabrication process, and offers some characterization results of the microcoupler. We predict the peak intensity required for SFWM to be observed in the microcoupler, as well as calculate the mode index splittings. Chapter 5 covers the experiment, describing each part of the apparatus. We also present results of the generated photon pairs, and results of single-photon tomography, which we use to analyze the polarization states of the SFWM photons. Chapter 6 concludes the thesis and offers some suggestions for future work.

1.2 Context and significance

Our work has been inspired by recent achievements on two main platforms: integrated optics and fiber-based devices. During the past decade, integrated optical gates and detectors have been demonstrated on the silicon-on-insulator (SOI) platform [1,2,11,12]. On-chip entanglement was achieved on the same system, as well as interfacing from one chip to another [9].

However, most of the experiments in integrated optics focused on quantum processing gates and detectors, but relied on off-chip photon sources. This is where fiber-based photon sources come into play. The main advantage of using a fiber-based source for integrated optics is that we can reduce the photon loss due to spatial mode mismatch. When using a conventional source for bulk optics, the laser is sent into free-space. The mismatch between the photon modes and the modes of the chip will cause a loss of the heralded single photons, lowering the efficiency before the photons get to the quantum processing gates on the microchip. A fiber-based photon source, on the other hand, generates photons that are in the fundamental mode of the fiber waveguide. These modes are well-matched with the modes of the integrated optical devices, and in effect reduce losses at the start of the photonic circuit. Another advantage of using a fiber based device is that it is relatively easy to engineer to obtain the desired properties of the generated photons, since the field of fiber optics is more mature than integrated photonics.

Based on previous work in photon-pair generation and characterization for both birefringent fibers and photonic crystal fibers [13–15,30], there has been more recent work on various fiber-based devices, with the goal of building an efficient photon source for integrated optics. As mentioned in the previous

section, SFWM is more versatile as the mechanism for generating photon pairs compared to SPDC. Using SFWM as the mechanism, there have been related research using standard birefringent fibers to generate photon pairs and to produce a range of two-photon spectral states - from correlated to completely uncorrelated - with potential applications for integrated optical networks [3]. SFWM is also utilized in birefringent fibers to make a tunable, high-efficiency, heralded singe-photon source, which could be used as a building block for large-scale entanglement generation [16]. Recently, three SFWM processes that conserve both orbital angular momentum (OAM) and parity have been observed in a few-mode, birefringent bowtie fiber. The results are used to characterize the fiber and move towards hybrid two-photon entanglement in the frequency and transverse modes [17, 20, 21]. The fiber used in this work also has an asymmetric (non-circular) cross section, allowing for transverse parity modes similar to our microcoupler.

Very recently, progress has been made regarding an integrated source of path-polarization hyperentangled cluster states [23]. Fidelities comparable to those previously obtained with bulk sources have been reported, and the source has been demonstrated to be an experimental on-chip realization of one-way quantum computation using different degrees of freedom. This device is also an attempt to implement on-chip hybrid multi-qubit multi-photon states for quantum computing. Another recent work features a two channel, degenerate, polarization-entangled source on a chip [24]. The chip is engineered to carry two periodically-poled waveguides and an integrated polarization splitter. High fidelity, polarization-entangled states have been generated and shown to violate Bell's inequality. This device is promising as an alternative to bulk photon sources, and as a step towards integrated circuits for quantum information.

In comparison with the other SFWM photon sources for integrated optics, our device is much simpler in structure while still allowing for future integration with optical chips. Our microcoupler is also easy to fabricate and engineer, since we are tapering commercial single-mode fibers in the lab and are not limited by properties of special fibers like the bowtie fiber. The microcoupler has a unique geometry which carries four modes that in theory can lead to entanglement. The main advantage of this structure is it carries four modes in both the polarization and spatial degrees of freedom. And even though we only used one input and one output port out of the four ports within the scope of this project, it is possible to measure the two outputs simultaneously to produce a wider range of quantum states.

1.3 Contributions of the author and acknowledgements

The purpose of this section is to acknowledge the input of the many collaborators, and to contextualize my contributions to the project.

The microcoupler design was proposed by Chams Baker, who also fabricated the samples. I tested the prototypes and provided feedback on improving the design, and also took part in the fabrication of the two newest microcouplers, the results for which are presented in this thesis.

The theoretical framework of coupled waveguide theory in Chapter 2 used work by Amnon Yariv [25] and Offir Cohen [26] as the main references. It was also based on previous work in birefringent and microstructured photonic crystal fibers from Jeff S. Lundeen [3, 10].

Chams Baker provided some early simulations for the microcoupler as a starting point. I tested the simulations and tried to adapt them for our experiment with the help of Lambert Giner and Chams Baker. Jefferson Flórez worked on an alternative simulation method using the commercial software Comsol, in order to model the novel microcoupler structure numerically. These Comsol simulation results were used in solving the phasematching equations for the structure. The phasematching theory is based on the book by Govind P. Agrawal [27]. I adapted the theory for our structure with guidance from Jeff S. Lundeen. The solutions to the 28 phasematching processes allowed for the microcoupler were obtained and analyzed with help from Lambert Giner, who also looked at some of the possible cases that allow for entanglement. Jefferson Flórez also helped with troubleshooting the phasematching code. I performed the analysis on the single-photon polarization tomography results with help from Jeff S. Lundeen and Lambert Giner to determine what phasematching processes were most likely responsible for the behaviour we observed. The scanning electron microscope (SEM) images were taken with the help of Sebastian A. Schulz.

The experimental results presented in this thesis were acquired at the femtosecond lab of the National Research Council (NRC), located at 100 Sussex Drive, Ottawa, Canada. I designed and set up the experiment with the help of Lambert Giner. The experimental setup was built on a previous experiment studying spontaneous four-wave mixing in birefringent fibers performed by Davor Curic. Duncan G. England and Philip J. Bustard of NRC provided valuable support and advice throughout the testing and data acquisition processes. I acquired the experimental data and performed most of the analysis.

This thesis was completed under the supervision of Jeff S. Lundeen. The project was a collaboration with Chams Baker of Xiaoyi Bao's fiber optics group at the University of Ottawa. It was also a collaboration with Benjamin J. Sussman's group, in particular Duncan G. England and Philip J. Bustard from the National Research Council. I would like to thank all the aforementioned collaborators for their help. I would also like to thank Jeff S. Lundeen for his patience and support.

2 Theory of waveguide photon-pair generation

This chapter aims to explain the theory involved in this thesis project, and serves to help understand the unique fiber-based structure used for photon-pair generation. The waveguide structure is called a *microcoupler*. In essence, it consists of two tapered single-mode fibers kept in contact. More details about the simulation, fabrication, and characterization of the microcoupler are presented in Chapters 3, 4, and 5, respectively.

This theory chapter starts with an overview of spontaneous four-wave mixing (SFWM), the nonlinear process that is used to generate photon pairs in the microcoupler. Spontaneous four-wave mixing in standard birefringent fibers is then presented as a well-studied example. Chapter 2.3 deals with coupled-mode theory, and is based on work by Yariv [25]. The microcoupler has a novel structure of two identical parallel waveguides kept in contact, which to our knowledge has no analytical solution. In order to get some intuition for the structure, we need to start from the existing theory for two isolated parallel waveguides and make approximations. The simulations are explained in the next chapter.

Chapter 2.4 explains what phasematching processes are allowed for the microcoupler. The selection rule is two-fold: restrictions on the allowed processes are due to the overlap of spatial modes, as well as the nonlinear optical susceptibility. This chapter ends with a conclusion section restating the main theoretical results that guide us throughout the project.

2.1 Spontaneous four-wave mixing: overview

Spontaneous four-wave mixing is a third order parametric nonlinear process. By parametric we mean the initial and final quantum mechanical states of the material system are identical. In other words, this process does not involve population transfer from one real level to another. Instead, population removed from the ground state resides in a virtual level for a time interval determined by the uncertainty principle [28]. The general form of the nonlinear polarization for a third-order nonlinear process is as follows

$$\widetilde{P}^{(3)}(t) = \epsilon_0 \chi^{(3)} \widetilde{E}^3(t), \tag{1}$$

where $\widetilde{P}^{(3)}$ is the third-order nonlinear polarization, $\widetilde{E}$ is the electric field strength, ϵ_0 is the permittivity of free space, and $\chi^{(3)}$ is the third-order non-

linear susceptibility. The electric field can depend on different frequency components

$$\widetilde{E}(t) = E_1 e^{-i\omega_1 t} + E_2 e^{-i\omega_2 t} + E_3 e^{-i\omega_3 t} + E_1^* e^{i\omega_1 t} + E_2^* e^{i\omega_2 t} + E_3^* e^{i\omega_3 t}. \quad (2)$$

As the name suggests, spontaneous four-wave mixing is a process with up to four different frequencies involved. Two photons enter the third-order nonlinear material and are converted into a pair of photons of different frequencies. We label the two photons entering the nonlinear medium as the pump photons $(p1, p2)$. The generated photon with the larger frequency is the anti-Stokes band, by convention called the signal (s), and the other generated photon is the Stokes band, or the idler (i). In order to achieve energy and momentum conservation, the process of mixing the involved frequencies must satisfy

$$\omega_{p1} + \omega_{p2} = \omega_s + \omega_i \quad (3)$$

$$\Delta k = k_{p1} + k_{p2} - k_s - k_i = 0. \quad (4)$$

This is because energy must be conserved in this process, and it is most likely to happen when the wave-vector mismatch Δk is equal to 0.

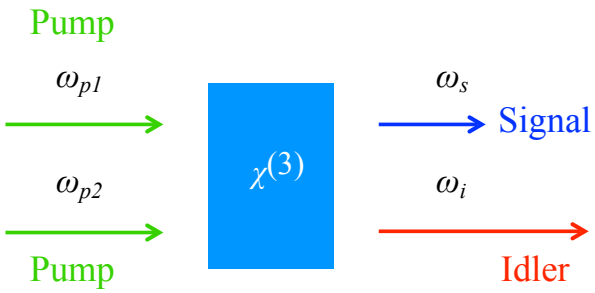

Figure 1: Schematic of the spontaneous four-wave mixing process. Two pump photons of frequency ω_{p1} and ω_{p2} enter a third-order nonlinear material and are converted into a signal photon and an idler photon of frequencies ω_s and ω_i, respectively. Throughout this project we only consider the case where the two pump photons are of equal frequency. The microcoupler is the $\chi^{(3)}$ material.

2.1.1 SFWM efficiency

The efficiency of photon-pair generation from spontaneous four-wave mixing depends on various factors, including the length of the waveguide L and the

peak intensity I_{peak}. If we define a parameter R, representing the generation rate, we have [29]

$$R \propto (I_{peak})^2 L. \tag{5}$$

Since the peak intensity is in turn proportional to the pulse energy E_{pulse}

$$I_{peak} \propto (\frac{1}{\Delta t})(\frac{1}{r^2})E_{pulse}, \tag{6}$$

where Δt is the pulse duration and r is the core radius of the waveguide, we have

$$\begin{aligned} R &\propto ((\tfrac{1}{\Delta t})(\tfrac{1}{r^2})E_{pulse})^2 L \\ &\propto \tfrac{1}{(\Delta t)^2}(\tfrac{1}{r^4})(E_{pulse})^2 L. \end{aligned} \tag{7}$$

So the efficiency for SFWM in a waveguide depends on the core diameter and length of the waveguide, as well as the pulse energy and pulse duration. This also explains our motivation for studying the microcoupler. We would like a source with a high photon generation rate, or high SFWM efficiency. Since the efficiency is inversely proportional to r^4, having a structure with a small core diameter is advantageous. The microcoupler has a diameter of 1 μm. We also pump it using a Ti:Sapph laser which has a short pulse duration ($\Delta t = 100$ fs), which would also increase the SFWM efficiency.

2.2 Spontaneous four-wave mixing in fibers

Before examining SFWM in the microcoupler, we study the simpler example of SFWM in a standard polarization-maintaining (PM) fiber. The standard PM fiber is birefringent and supports two orthogonal polarization modes, while the microcoupler supports four modes. In this section we show the solution to the phasematching equation for a birefringent fiber, and show that we can predict the wavelengths of the photon pairs generated via SFWM. In order to solve the phasematching equation for the birefringent fiber, we need an expression for its birefringence, which is equivalent to the splitting between the two polarization modes. This derivation is shown in Chapter 2.2.2, while a similar expression is used later in Chapter 4.3.2 to calculate the spatial mode splittings for the microcoupler.

2.2.1 SFWM in a standard birefringent fiber

For spontaneous four-wave mixing in fibers, Eq. (4) for the wave-vector mismatch shown in the section above needs to be modified into Eq. (8) below,

while the equation for energy conservation in terms of frequency (Eq. (3)) stays the same [27, 30]

$$\Delta k = k_{p1}(\omega_{p1}) + k_{p2}(\omega_{p2}) - k_s(\omega_s) - k_i(\omega_i) + (1-B)\gamma(P_{p1} + P_{p2} + 2\sqrt{P_{p1}P_{p2}}) = 0. \tag{8}$$

Here the subscripts correspond to the different modes of the four photons involved in this process, γ is the nonlinear parameter of the fiber, B relates to the pump polarization relative to the signal and the idler photons, P_{p1} and P_{p2} are peak powers of the pump photons $p1$ and $p2$ [3]. The first four terms in Eq. (8) are the frequency-dependent wave vectors, corresponding to the wave vectors in Eq. (4) from the previous section. The last term represents the Kerr effect and the cross-Kerr effect [28].

When both Eqs. (3) and (9) are satisfied in the birefringent fiber for the selected pump frequencies, the configuration is considered to be phase-matched. Different phasematching configurations have been studied for both birefringent and microstructured photonic-crystal fibers (PCFs) [10]. For simplicity, in this example we choose a configuration that has been examined in a standard birefringent fiber [30]. In this case we have a single pump pulse ($\omega_{p1} = \omega_{p2} = \omega_p$) that is polarized along one of the two principal axes of the birefringent fiber. The generated signal and idler photons are polarized along the axis orthogonal to the pump. In this cross-polarized birefringent phasematching configuration, the wave-vector mismatch, written explicitly in terms of the fiber birefringence Δn, is

$$\begin{aligned} \Delta k &= 2k_p(\omega_p) - k_s(\omega_s) - k_i(\omega_i) + 2\Delta n\tfrac{\omega_p}{c} + \tfrac{2}{3}\gamma P \\ &= 2\tfrac{\omega_p}{c}n(\omega_p) - \tfrac{\omega_s}{c}n(\omega_s) - \tfrac{\omega_i}{c}n(\omega_i) + 2\Delta n\tfrac{\omega_p}{c} + \tfrac{2}{3}\gamma P, \end{aligned} \tag{9}$$

where we assumed the pump is polarized along the slow axis. The constant offset Δn is added to the slow axis, with both principal axes of the fiber modelled to have the same material dispersion $n(\omega)$. The factor $B = 2/3$ comes from the self-phase modulation and cross-phase modulation between the modes, and P is the peak power of the pump pulse [27]. We have made the approximations that in this cross-polarized phasematching configuration, phasematching is realized far from the zero-dispersion wavelength, the material dispersion dominates [30], and also the birefringence Δn changes little over the wavelength range of interest [3]. When solving the phasematching equation later on, we also assume the self- and cross-phase modulation terms are negligible, thus dropping the final term in Eq. (9).

2.2.2 Theory for fiber birefringence measurement

A birefringent fiber supports two orthogonal polarization modes along the two fiber axes, each with its own wavelength-dependent index of refraction, n_x and n_y. The index of refraction is the ratio between the speed of light in vacuum and the speed of light in a medium. When light with mixed polarization is sent into the fiber, we will get interference from light in the two polarization modes because they are each delayed by a different phase.

We can calculate the birefringence $\Delta n = \Delta n_{xy}$, or the difference in refractive indices between the two polarization modes, if we measure the spacing between the interference fringes. We measure this wavelength difference, $\Delta\lambda$, between two adjacent interference fringes using an optical spectrum analyzer (OSA). The experimental procedure is explained in Chapter 4. Both λ and n are varying in this situation because we are also looking at peaks located at different wavelengths on the OSA. In order to solve for Δn in terms of the known parameters such as pump wavelength and the measured fringe spacing, we start with an expression for phase accumulation, and then introduce the interference of light.

Phase is directly proportional to the index of refraction of the medium. Adding a piece of glass in the path of a beam in free space adds a phase delay and slows it down. Phase is also proportional to the propagation length, L. The longer the light propagates in a medium, the more phase is accumulated. Thus we have

$$\phi = \frac{2\pi n}{\lambda_p} L, \tag{10}$$

where λ_p is the wavelength of the pump. Note that the phase ϕ is inversely proportional to λ_p. With interference, one full fringe on the OSA represents a phase delay of 2π.

Light of each type of polarization has its own phase accumulation in the medium. In other words, there is a phase difference between light of the two interfering wavelengths for each polarization:

$$\Delta\phi = L(2\pi\frac{n_x}{\lambda_1} - 2\pi\frac{n_x}{\lambda_2}), \tag{11}$$

and

$$\Delta\phi' = L(2\pi\frac{n_y}{\lambda_1} - 2\pi\frac{n_y}{\lambda_2}), \tag{12}$$

where λ_1 and λ_2 are the wavelengths of the peaks of the two adjacent fringes. Subtracting Eq. (12) from Eq. (11), we get a phase difference of one full

fringe (2π)

$$\begin{aligned} 2\pi &= 2\pi L(\tfrac{1}{\lambda_1-\lambda_2}(n_x - n_y)) \\ \tfrac{1}{\Delta n_{xy} L} &= \tfrac{1}{\lambda_1-\lambda_2}. \end{aligned} \tag{13}$$

Here we make the approximation that the two wavelengths are close together, and $\lambda_1 = \lambda_{pump}$, which is to say the fringe spacing is small compared to the pump wavelength:

$$\frac{1}{\lambda_{pump} - \lambda_2} \approx \frac{\Delta\lambda}{(\lambda_p)^2 + \lambda_p \Delta\lambda} \approx \frac{\Delta\lambda}{(\lambda_p)^2}. \tag{14}$$

Thus we have the relationship between the fiber birefringence $\Delta n_{xy} = \Delta n$, and the interference fringe spacing $\Delta\lambda$

$$\Delta\lambda = \frac{\lambda_p^2}{\Delta n_{xy} L}, \tag{15}$$

and

$$\Delta n_{xy} = \frac{\lambda_p^2}{\Delta\lambda L}, \tag{16}$$

where L is the interaction length, or the length of the birefringent fiber.

After we solve for the birefringence, we can substitute it into the fiber phasematching equation, Eq. (9). We can then solve for $\Delta k = 0$ for the different possible phasematching situations, and obtain predictions for the wavelengths of the generated photons.

2.2.3 Phasematching solution for a birefringent fiber

The purpose of this sub-section is to show an example of the phasematching solution plot for a standard birefringent fiber. This can be used as a comparison for the more complex case of the microcoupler phasematching plots, shown in Chapter 3.2 and the appendix.

We have seen, for a birefringent fiber, we can measure the fringe spacing $\Delta\lambda$ and calculate its birefringence Δn, which we can in turn substitute into Eq. (9). This would allow us to predict which phasematching configurations are possible, and where we expect to observe the generated photon pairs. An example of the phasematching solution plot for a birefringent fiber is shown in Fig. 2. Using plots like this one, we can predict frequencies of the signal and idler photons generated by SFWM in this birefringent fiber. The vertical axis plots the splitting between the signal (or idler) frequency ω_s (ω_i) and the

pump frequency ω_p. The signal photon is in the upper half of the plot, above the $\Delta\omega = 0$, and the idler photon is in the lower half. The signal and idler frequencies are symmetric from the pump frequency by energy conservation. From this plot we can see the chosen birefringent fiber is a good candidate for generating SFWM photons using a pump at 800 nm, because the signal and idler photons are predicted to be far away from the pump. For the microcoupler we hope to get such large frequency splittings, as well.

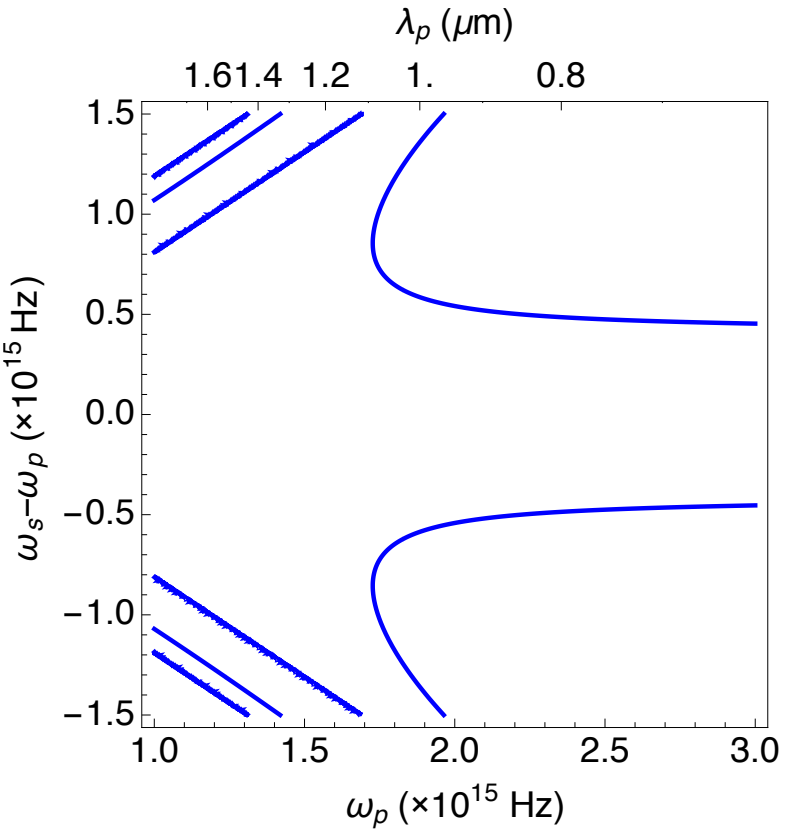

Figure 2: Plot of the solution to the phasematching equation for a standard birefringent fiber. The phasematching equation is $\beta_H + \beta_H = \beta_V + \beta_V - 2\Delta n\frac{\omega_p}{c}$. *The vertical axis corresponds to the frequency splitting between the signal photon and the pump. The lower horizontal axis plots the pump frequency* ω_p *multiplied by* 10^{15} Hz, *and the upper horizontal axis plots the pump wavelength* λ_p *in* μm. *The solid curve represents all the solutions to the phasematching equation, and we have two solutions for the pump wavelength equal to 0.8* μm. *The signal photon is predicted to be at 664 nm and the idler at 1022 nm.*

In order to obtain Fig. 2, the Sellmeier coefficients for fused silica are used to calculate the refractive index of the core [27]. This core index is then used

to calculate the propagation constant β, equivalent to the wavevector k in Eq. (9). For this fiber, the birefringence Δn is calculated to be 4.3×10^{-4} [3]. After generating the plot, we find the magnitude of the frequency splitting $\Delta\omega$ from the plot, and calculate the wavelength of the generated photons. The splitting $\Delta\omega$ is the difference between the pump frequency and the signal or idler frequency. Similar phasematching plots for the microcoupler are examined in more detail in Chapter 3 and the appendix.

For the birefringent fiber case, predicting the wavelengths of the generated photons from the phasematching plot is relatively simple, mainly because there are only two polarization modes in the fiber. However, due to the unique structure of the microcoupler and the fact that it supports four modes in two degrees of freedom (polarization and spatial), we need a model more complex than the standard birefringent fiber. The remainder of this chapter shows our approach to modelling the microcoupler in order to understand its SFWM and phasematching possibilities.

2.3 Coupled-mode theory

As mentioned in the beginning of this chapter, we cannot solve for the effective refractive indices for the modes of the microcoupler analytically due to its unique geometry. We need to adapt existing theory to model our microcoupler structure. The microcoupler consists of two identical single mode fibers (SMFs) held together during fabrication. The uniform interaction region, or effective length, is 10 cm long, and the diameter of the taper is 1 μm. A schematic for the microcoupler is shown in Fig. 3. The microcoupler fabrication process is described in Chapter 4.

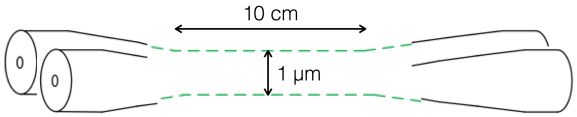

Figure 3: Schematic of the microcoupler structure (not-to-scale). The tapered region is shown with dashed lines. The effective length is 10 cm long. We assume this region has a constant diameter of 1 μm. In our model we neglect the transition region on either end of the effective length, where the core diameter is changing rapidly. The figure is modified from [31].

To our knowledge there is no analytical solution for this type of structure

where the two waveguides are kept in contact throughout the effective length. Existing theory on coupled waveguides assume the two waveguides are isolated, or separated far enough to be in the weak coupling regime [32–34]. The motivation for making a microcoupler with the two waveguides in contact, thus being in the strong coupling regime, is mainly to achieve large mode splittings. Having large splittings between the signal and idler modes due to strong coupling ensures the generated signal and idler photons are far away from the pump and the Raman noise. An example of the standard Raman spectrum is shown in Fig. 4. If we are in the weak coupling regime, the generated photons due to the spatial mode splittings could be between the pump and Raman, and get filtered out. We would prefer to have the idler photon outside of the Raman band, rather than between the pump and the Raman. Thus we designed the microcoupler to have two touching waveguides to be in the strong coupling regime throughout the effective interaction length.

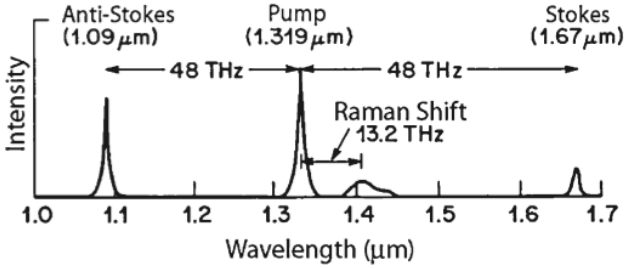

Figure 4: Example output spectrum showing the Raman band generated along with the signal (anti-Stokes) and idler (Stokes) photons in an early demonstration of four-wave mixing in a single-mode fiber pumped at 1.319 μm. In this case the signal and idler photons are generated far from the pump and Raman band, which would be ideal. This figure was taken from [27], original data from [35].

In the next few sections the standard coupled-mode theory for two isolated, parallel waveguides is utilized with perturbation theory to get some physical intuition for the spatial modes of the microcoupler. We will take the geometry for strong coupling into consideration when simulating the microcoupler numerically in the next chapter.

2.3.1 Coupling of two parallel waveguides

The general requirement for a waveguide of EM radiation is a flow of energy along the guiding structure and not perpendicular to it. A dielectric cylinder can act as a waveguide if its index of refraction is large enough

($n_{core} > n_{surroundings}$). Higher index of refraction in the core of a guiding structure acts like a converging lens (light bends towards higher n). A guided mode is supported by the dielectric structure when the converging effect cancels out spreading due to diffraction.

Because the microcoupler has two identical cores next to each other, we can model the composite structure as two parallel cylindrical waveguides. The composite structure of two waveguides carries four modes in two degrees of freedom: polarization and spatial mode. In the weak coupling regime where conventional coupled-mode theory is most accurate, the two waveguides are approximated to be infinitely far apart. Their modes propagate independently, each with its own propagation constant [32]. When two waveguides are brought close together, the modes they carry will couple to each other. This is because in this geometry the modes are no longer confined to each waveguide, and the evanescent field of each waveguide can leak over to the other side, as well as interact with the evanescent field of the other core. This leads to mode coupling and splitting. Mathematically, the amplitude of each mode is modified by the presence of the mode in the other core. This effect shows up as the exchange coupling or mutual coupling coefficients in the coupled amplitude equations.

For the microcoupler, the two waveguides are kept in contact in the composite structure, leading to stronger coupling and larger mode splittings. The delocalized modes over the composite structure can be seen as a superposition of the modes in the two cores, as a result of this interaction of evanescent fields. This mode splitting and coupling is also analogous to the quantum double oscillator model, where the four modes are eigenvectors of the Hamiltonian of the composite system. We can write wavefunctions of the superpositions of the fundamental modes in each oscillator [36], and the result has the same form as the symmetric and antisymmetric composite modes of the microcoupler, which we are going to derive in the rest of this section and the next.

We consider one of the two cylindrical dielectric waveguides, assuming it is homogeneous along the z-axis. Starting from Maxwell's equations, we can reach the scalar wave equation

$$\nabla_t^2 \mathcal{E} + [(\frac{\omega}{c})^2 n^2(x,y) - \beta^2]\mathcal{E} = 0. \tag{17}$$

The equation above can be viewed as an eigenvalue problem with the electric field $\mathcal{E}$ as the eigenfunctions and β^2 as the eigenvalues, where β is the

propagation constant of the mode. The eigenfunctions $\mathcal{E}$ must satisfy: 1) continuity at interfaces, 2) boundary conditions at infinity [25].

For a system of two parallel waveguides separated by a finite distance, the modes may be coupled if there is a physical overlap of the mode wavefunctions. We use coupled-mode theory to treat the coupling between the modes. As mentioned before, even though assuming two separated waveguides in the weak coupling regime would not provide accurate results of our structure, we would like to adapt the existing model to get an approximation of our structure to qualitatively understand how phasematching will work. More specifically, we are going to derive the electric field wavefunctions of the symmetric and antisymmetric modes of the composite structure, as well as the propagation constant for each. This will provide more intuition on the symmetric and antisymmetric modes unique to this geometry, before we move on to examine the allowed phasematching processes in Chapter 2.4.

The electric field for general wave propagation in this coupled-waveguide structure can be approximated by:

$$\mathbf{E}(x,y,z,t) = C_a\mathcal{E}_a(x,y)\exp[i(\omega t - \beta_a z)] + C_b\mathcal{E}_b(x,y)\exp[i(\omega t - \beta_b z], \quad (18)$$

where β_a and β_b are the propagation constants for the fundamental modes of each of the two waveguides. Later we will treat the case of two identical waveguides where $\beta_a = \beta_b$. In writing C_a and C_b as constants, we have assumed the amplitudes of the fundamental modes do not vary with propagation distance z. Eq. (18) is valid when the two waveguides are not too close to each other, and the two fundamental modes ($\mathcal{E}_a(x,y)\exp[i(\omega t - \beta_a z)], \mathcal{E}_b(x,y)\exp[i(\omega t - \beta_b z]$) are the only two confined modes of the waveguides. This expression for the composite mode is sufficient for our model of the microcoupler as a starting point. Even though in our system the two identical fiber waveguides are almost touching, this model could still provide some insight on understanding the structure we are studying.

We treat the coupling between the modes with coupled-mode theory and perturbative analysis, based on work by A. Yariv [25]. We are interested in finding the wavelength-dependent effective propagation wavevector $\beta(\lambda)$ for the composite modes. From the propagation constants we will be able to find the allowed phasematching combinations, and predict the wavelength of the photon pairs produced via spontaneous four-wave mixing in the microcoupler.

2.3.2 Refractive index distribution of a composite waveguide

For a composite waveguide with two cores labelled a and b, the index profile of the composite structure can be written as

$$n^2(x,y) = n_s^2(x,y) + \Delta n_a^2(x,y) + \Delta n_b^2(x,y), \tag{19}$$

where $n_s^2(x,y)$ is the refractive index distribution of the region outside the cores of the two waveguides. Since the two cores are identical, they have the same mode profile

$$n_\alpha^2(x,y) = n_s^2(x,y) + \Delta n_\alpha^2(x,y), \tag{20}$$

where Δn_α^2 represents the added contribution of waveguide α ($\alpha = a, b$). It is defined as

$$\begin{aligned} \Delta n_a^2(x,y) &= n_a^2 - n_s^2 \qquad \text{core } a \\ &= 0. \qquad\qquad \text{elsewhere} \end{aligned} \tag{21}$$

So the individual waveguide modes satisfy the following equation [25]

$$(\frac{\partial^2}{\partial x^2} + \frac{\partial^2}{\partial y^2} + \frac{\omega^2}{c^2}[n_s^2(x,y) + \Delta n_\alpha^2(x,y)])\mathcal{E}_\alpha(x,y) = \beta_\alpha^2 \mathcal{E}_\alpha(x,y). \tag{22}$$

Because the presence of one waveguide imposes a dielectric perturbation Δn_α^2 on the propagation of modes in the other waveguide, the electric field of the composite mode as given by Eq.(18) must obey the wave equation

$$(\frac{\partial^2}{\partial x^2} + \frac{\partial^2}{\partial y^2} + \frac{\partial^2}{\partial z^2} + \frac{\omega^2}{c^2}[n_s^2(x,y) + 2\Delta n_\alpha^2(x,y)])\mathbf{E} = 0. \tag{23}$$

Note the factor of two before the dielectric perturbation term, Δn_α^2. Here we have replaced one of the perturbation terms in Eq. (19), since the added contribution from one waveguide to another identical waveguide is equal to the contribution from the second waveguide to the first.

We are interested in calculating the propagation constants of the composite structure. We can use perturbation analysis to find approximate solutions to the wave equation and thus find an approximation of the composite modes of propagation in the waveguide. An example of this kind of perturbation analysis is carried out in the next section.

2.3.3 Approximate solutions using perturbation theory

In order to find the propagation constant β for composite modes, we rewrite Eq. (18) as the following

$$\mathbf{E}(x,y)e^{-i\beta z} = [C_a\mathcal{E}_a(x,y) + C_b\mathcal{E}_b(x,y)]e^{-i\beta z}, \tag{24}$$

where β is the propagation constant for the composite waveguide. We then substitute the equation above into the wave equation, Eq. (23), and use Eq. (22) to obtain [25]

$$C_a(\beta_a^2 + \frac{\omega^2}{c^2}\Delta n_b^2(x,y) - \beta^2)\mathcal{E}_a + C_b(\beta_b^2 + \frac{\omega^2}{c^2}\Delta n_a^2(x,y) - \beta^2)\mathcal{E}_b = 0. \quad (25)$$

Taking the scalar product of the equation above with $\mathcal{E}_a^*(x,y)$ and $\mathcal{E}_b^*(x,y)$, respectively, and integrating over the entire xy plane leads to a linear equation for C_a and C_b:

$$\begin{bmatrix} \beta_a^2 - \beta^2 + K_a & J_a + I^*(\beta_b^2 - \beta^2) \\ J_b + I(\beta_a^2 - \beta^2) & \beta_b^2 - \beta^2 + K_b \end{bmatrix} \begin{bmatrix} C_a \\ C_b \end{bmatrix} = 0 \quad (26)$$

where $I = \iint \mathcal{E}_b^* \cdot \mathcal{E}_a \,\mathrm{d}x\,\mathrm{d}y$ is the overlap integral. K_a and K_b represent the dielectric perturbation of one waveguide due to the presence of the other, while J_a and J_b are the exchange coupling between the two waveguides. Both parameters are related to the dielectric perturbation $\Delta n_\alpha^2 (\alpha = a, b)$ previously defined in Equation (21). These constants are in the form of

$$J_\alpha = (\frac{\omega}{c})^2 \iint \mathcal{E}_\alpha^* \cdot \Delta n_\alpha^2(x,y)\mathcal{E}_\alpha \,\mathrm{d}x\,\mathrm{d}y. \quad (27)$$

The eigenvalues β_1 and β_2 are solutions to the secular equation

$$\begin{vmatrix} \beta_a^2 - \beta^2 + K_a & J_a + I^*(\beta_b^2 - \beta^2) \\ J_b + I(\beta_a^2 - \beta^2) & \beta_b^2 - \beta^2 + K_b \end{vmatrix} = 0. \quad (28)$$

The wavefuctions corresponding to the propagation constants can be found by solving for the two constants C_a and C_b [25].

For our case of two identical waveguides making up the microcoupler, $K_a = K_b = K, J_a = J_b = J$. So the propagation constants and wavefunctions of the composite structure of two parallel waveguides are [25]

$$\begin{aligned} \beta_1^2 &= \beta_0^2 + \tfrac{K+J}{1+I} \\ \beta_2^2 &= \beta_0^2 + \tfrac{K-J}{1-I} \\ \mathbf{E}_1 &= \tfrac{1}{\sqrt{2(1+I)}}(\mathcal{E}_a + \mathcal{E}_b) \\ \mathbf{E}_2 &= \tfrac{1}{\sqrt{2(1-I)}}(\mathcal{E}_a - \mathcal{E}_b). \end{aligned} \quad (29)$$

The mode with wavefunction $\mathbf{E}_1$ and propagation constant β_1 is the composite mode with a symmetric wavefunction. The mode with wavefunction $\mathbf{E}_2$

and propagation constant β_2 is another composite mode with an antisymmetric wavefunction. These two wavefunctions are orthogonal.

So far we have obtained expressions for the propagation constants as well as the even and odd modes, as shown in Eq. (29) above. The main purpose of using the coupled-mode theory for two parallel waveguides in this section was to get some intuition for the even and odd modes in our microcoupler. As previously mentioned, the microcoupler is composed of two tapered single mode fibers (SMFs) kept in contact, and the standard coupled-mode theory does not describe it exactly, nor does any other analytical model we are aware of. We have made the approximation according to standard coupled-mode theory that the two cores are not close enough to allow for strong coupling. The strong coupling between modes of the two adjacent cores is taken into account in our numerical simulations, discussed in Chapter 3.

2.4 Phasematching processes allowed for microcoupler

The purpose of this section is to explain how we arrived at the 28 allowed phasematching processes for the microcoupler. Because the microcoupler supports four modes, there are a lot more possible phasematching processes allowed compared to a standard birefringent fiber. There are two main factors imposing restrictions on what phasematching processes are allowed for the microcoupler: the overlap of the spatial modes, and the nonlinear optical susceptibility. We examine each of these restrictions in the following subsections, and show the resulting 28 phasematching processes at the end of this section, in Table 1. In reaching this result, we make use of the scalar theory of SFWM [27], as well as the nonzero terms of the nonlinear optical susceptibility [28].

2.4.1 Restriction due to the overlap of spatial modes

In this section we use the coupled amplitude equations of the scalar theory of SFWM, in order to find out how many phasematching configurations are allowed for the microcoupler due to the overlap of the spatial modes.

Starting with the third-order polarization equation at the beginning of this chapter, Eq. (1), and the definition of the general third-order electric field in Eq. (2), we rewrite the electric field for our case of four-wave mixing as

$$\mathbf{E} = \frac{1}{2}\hat{x}\sum_{j=1}^{4} E_j \exp[\mathrm{i}(\beta_j z - \omega_j t)] + \text{c.c.}, \tag{30}$$

where corresponding to Eq. (3) at the beginning of this chapter, $\omega_{p1} = \omega_1, \omega_{p2} = \omega_2, \omega_3 = \omega_s, \omega_4 = \omega_i$. We can write the sum of the electric fields of the four frequencies in this way because the two waveguides of the microcoupler are identical. We then substitute definitions for the total electric field and polarization for a single core into the scalar wave equation (Eq. (17)). A full-vector theory would be preferred in a more rigorous context since SFWM is polarization-dependent. But for the purposes of our experiment, here we only consider the the scalar case in which all four fields are linearly polarized along a principal axis x of a birefringent fiber [27].

Again, here we assume an undepleted pump since its intensity is much larger than that of the signal or the idler. We neglect time-dependence under quasi-continous-wave (quasi-CW) conditions. The spatial dependence is included using

$$E_j(\mathbf{r}) = F_j(x, y)A_j(z), \tag{31}$$

$F_j(x, y)$ being the spatial distribution of the fiber mode in which the jth field propagates inside the fiber ($j = 1 - 4$) [37].

Integrating over the spatial mode profiles, we can arrive at the following set of four coupled equations [27]. Eqs. (32) to (35) describe the evolution of the amplitude $A_j(z)$ four each of the four modes supported by the microcoupler

$$\frac{dA_1}{dz} = \frac{\mathrm{i}n_2\omega_1}{c}[(f_{11}|A_1|^2 + 2\sum_{k\neq 1} f_{1k}|A_k|^2)A_1 + 2f_{1234}A_2^*A_3A_4e^{\mathrm{i}\Delta kz}] \tag{32}$$

$$\frac{dA_2}{dz} = \frac{\mathrm{i}n_2\omega_2}{c}[(f_{22}|A_2|^2 + 2\sum_{k\neq 2} f_{2k}|A_k|^2)A_2 + 2f_{2134}A_1^*A_3A_4e^{\mathrm{i}\Delta kz}] \tag{33}$$

$$\frac{dA_3}{dz} = \frac{\mathrm{i}n_2\omega_3}{c}[(f_{33}|A_3|^2 + 2\sum_{k\neq 3} f_{3k}|A_k|^2)A_3 + 2f_{3412}A_1A_2A_4^*e^{-\mathrm{i}\Delta kz}] \tag{34}$$

$$\frac{dA_4}{dz} = \frac{\mathrm{i}n_2\omega_4}{c}[(f_{44}|A_4|^2 + 2\sum_{k\neq 4} f_{4k}|A_k|^2)A_4 + 2f_{4312}A_1A_2A_3^*e^{-\mathrm{i}\Delta kz}]. \tag{35}$$

Here we have assumed the self-phase modulation and cross-phase modulation terms are negligible in Eq. (8), relabelling the frequencies and essentially going back to the definition of the wave vector mismatch in Eq. (4). We have

also neglected the frequency dependence of the nonlinear coefficient $\chi^{(3)}$. The overlap integral is given by [37]

$$f_{ijkl} = \frac{\langle F_i^* F_j^* F_k F_l \rangle}{[\langle |F_i|^2 \rangle \langle |F_j|^2 \rangle \langle |F_k|^2 \rangle \langle |F_l|^2 \rangle]^{1/2}}. \tag{36}$$

The overlap integral is nonzero only for certain combinations of modes with the proper symmetry. Here we use a parity argument with this overlap integral to figure out the criteria for allowed phasematching configurations in the microcoupler.

We know the modes of the microcoupler are real, so we can safely disregard the complex conjugates. The integral of an odd function is equal to 0, so to get a nonzero overlap function, the product $F_i F_j F_k F_l$ in the numerator has to be even. Starting with the case where we assume all modes have the same polarization, we can go through the possible combinations of the two spatial modes for the four frequencies involved. The two spatial modes are labelled *even* and *odd*, or symmetric and antisymmetric. In addition to the simplest case where all four modes are the same (all *even* or all *odd*), the two pump modes can be both *even* or both *odd*. In order for the entire product to turn out even, the two daughter photons must also have the same parity (both *odd* or both *even*). We can also have the two pump modes being one *odd* and one *even*, with two daughter photons also one *odd* and one *even*, so that the total product is even and the result nonzero.

In summary, we found that only the symmetry that has an even number of each of the *even* and *odd* modes allows for a nonzero overlap integral. In other words, only the phasematching processes where there are 0, 2, or 4 occurrences of the *even* mode would be allowed in the microcoupler.

2.4.2 Restriction due to the nonlinear optical susceptibility

In addition to the nonzero overlap integral determined by the combination of spatial modes, as shown in Eq. (36), the number of allowed phasematching processes is also restricted by the number of nonzero elements in the nonlinear optical susceptibility.

The third-order nonlinear optical susceptibility $\chi^{(3)}_{ijkl}$ is a fourth-rank tensor described by 81 separate elements. For isotropic materials such as glass, the spatial symmetry of the material reduces the number of independent elements. This is because each of the coordinate axes, x, y, z, must be equivalent

in an isotropic material. For fused silica, there are 21 nonzero elements, of which only 3 are independent [28]:

$$\begin{aligned} yyzz = zzyy = zzxx = xxzz = xxyy = yyxx, \\ yzyz = zyzy = zxzx = xzxz = xyxy = yxyx, \\ yzzy = zyyz = zxxz = xzzx = xyyx = yxxy, \\ xxxx = yyyy = zzzz. \end{aligned} \tag{37}$$

For our microcoupler, we are only interested in the x and y axes because the incident beam propagates on the z-axis, perpendicular to the x-y plane. We assume the electric field distribution stays constant along the z-direction. We can now neglect the elements containing z in Eq. (37), and are left with

$$\begin{aligned} xxyy = yyxx, \\ xyxy = yxyx, \\ xyyx = yxxy, \\ xxxx = yyyy. \end{aligned} \tag{38}$$

Thus we are restricted to 8 nonzero elements for the nonlinear optical susceptibility $\chi^{(3)}_{ijkl}$, in addition to the selection rule from the nonzero overlap integral.

While going through all the permutations with both criteria, we also discard the redundant cases. This is possible because throughout this project we assume the two pump photons to be equal in wavelength, so we can interchange them and still count it as one unique process. For example, $xe + yo \rightarrow yo + xe$ is counted as the same process as $yo + xe \rightarrow yo + xe$, where o and e stand for the *odd* and *even* (or symmetric and antisymmetric) modes. We found out there are 28 unique phasematching processes allowed in the microcoupler. They are shown in Table 1.

2.5 Conclusion

In this chapter, we covered the main theoretical aspects of the project. Following an overview of spontaneous four-wave mixing (SFWM), we used the standard birefringent fiber as an example. Because we could not find an analytic solution for the microcoupler structure, we used standard coupled-mode theory with perturbation theory in order to get some intuition on the composite modes. The main approximation was we assumed the two waveguides are far apart in coupled-mode theory, when they are actually in contact. We

	Pump1	Pump2	Signal	Idler
1	y-o	y-o	y-o	y-o
2	y-o	y-o	y-e	y-e
3	y-e	y-e	y-e	y-e
4	y-e	y-e	y-o	y-o
5	y-o	y-e	y-e	y-o
6	x-o	x-o	x-o	x-o
7	x-o	x-o	x-e	x-e
8	x-e	x-e	x-e	x-e
9	x-e	x-e	x-o	x-o
10	x-o	x-e	x-e	x-o
11	y-o	y-o	x-o	x-o
12	y-o	y-o	x-e	x-e
13	y-e	y-e	x-e	x-e
14	y-e	y-e	x-o	x-o
13	y-o	y-e	x-e	x-o
16	x-o	x-o	y-o	y-o
17	x-o	x-o	y-e	y-e
18	x-e	x-e	y-e	y-e
19	x-e	x-e	y-o	y-o
20	x-o	x-e	y-e	y-o
21	y-o	x-o	x-o	y-o
22	y-o	x-o	x-e	y-e
23	y-e	x-e	x-e	y-e
24	y-e	x-e	x-o	y-o
25	y-o	x-e	x-e	y-o
26	y-o	x-e	x-o	y-e
27	y-e	x-o	x-o	y-e
28	y-e	x-o	x-e	y-o

*Table 1: This table shows all of the 28 phasematching processes allowed in the microcoupler. The last four columns correspond to the four photons involved: two pump photons (Pump*1 *and Pump*2*), the signal, and the idler. Each row represents a possible phasematching process. The possible modes for each photon are abbreviated: x and y represent the two orthogonal polarizations, and o and e stand for the odd and even (or symmetric and antisymmetric) modes. For example, row 28 represents the phasematching situation where the two pump photons are in the modes y-even and x-odd, respectively. The signal photon is in the mode x-even, and the idler photon has the mode y-odd. The 28 processes are grouped in the following order: (1) All four photons are y-polarized; (2) All four photons are x-polarized; (3) Pump photons are y-polarized, generated photons are x-polarized; (4) Pump photons are x-polarized, generated photons are y-polarized; (5) Pump photons are orthogonally polarized, generated photons are orthogonally polarized.*

designed the microcoupler to be in the strong coupling regime because we wanted large mode splittings which would allow the generated photons to be far away in wavelength from the pump and Raman spectrum. The numerical simulations for the microcoupler in the strong coupling regime are examined in Chapter 3.
In Chapter 2.4, we also investigate the phasematching processes allowed by the geometry of the microcoupler, and conclude there are 28 allowed processes. The two main factors restricting the processes allowed are the overlap of spatial modes and the nonlinear optical susceptibility.

3 Numerical simulations for microcoupler

As mentioned at the start of the preceding chapter, we expect the four modes supported by the microcoupler to have different effective indices of refraction. This is because the asymmetry in the structure causes different boundary conditions along the x and y directions across the microcoupler cross-section, leading to the splitting of birefringent modes. This results in a difference in the refractive indices for the x- and y-polarized modes. On the other hand, the fundamental modes carried in each of the two adjacent waveguides can couple to each other by evanescent fields, causing each of the single waveguide modes to split into two delocalized modes over the composite structure. This leads to another difference in refractive indices between the spatial modes of the composite structure. The index profile of the composite waveguide structure can be seen as a superposition of the modes in each waveguide, accounting for the effect of the overlapping evanescent fields. The modes of the composite structure are sometimes called *supermodes*, to distinguish them from the single waveguide modes. This is shown mathematically in in Eqs. (19)–(21) in Chapter 2.3, for the general case of two parallel waveguides separated by a distance. For the microcoupler, the two waveguides are kept in contact and have stronger coupling between the two cores. This is because we would like to get larger spatial mode splittings that would ensure SFWM photons are generated far away from the pump and outside of the Raman. For the microcoupler we also have more splittings between modes of different degrees of freedom, for example, $\Delta n = n_{y,odd} - n_{x,even}$.

In this chapter we use numerical simulations to calculate the effective refractive index of each of the four modes supported by the microcoupler - *x-even, x-odd, y-even, y-odd*. An overview of the simulation process is presented in Chapter 3.1. We also calculate the differences between refractive indices, Δn, in order to solve for the phasematching equation. Chapter 3.2 describes how we solve the phasematching equation and plot the solutions of each of the 28 possible phasematching combinations. It also explains how to interpret the 28 contour plots we obtain from the solutions. The main goal for generating the phasematching contours is to predict the wavelengths of the photon pairs generated via spontaneous four-wave mixing (SFWM). Because we have many different phasematching situations possible, we expect multiple sets of photon pairs to be generated simultaneously. The phasematching solutions help us find out which photons are predicted at wavelengths practical for detection in our experiment. We are also interested in seeing if two phasematching processes from different combinations of modes can produce photon pairs at the same wavelengths, which could lead to entangled pho-

tons. Chapter 3.3 provides analysis of the solutions, and highlights results from varying parameters such as the core diameter of the microcoupler in search of entanglement. The final section concludes this chapter and summarizes the main theoretical results.

3.1 Calculation of the microcoupler mode dispersion

We calculate the effective refractive index (i.e., the effective mode index n_{eff}) of each of the four modes, *x-even, x-odd, y-even, y-odd*, using the commercial mode solver software Comsol. Simulating the microcoupler structure in this software consists of three main steps: designing the structure to be simulated, choosing the material for each component, and calculating the effective refractive index for each mode.

3.1.1 Building the structure for simulation

The simulation region is defined to be a rectangle of size $11d \times 10d$, where d is the diameter of the microcoupler. A rectangular region is the easiest option to resemble our microcoupler geometry, using an elliptical region would also be suitable. The key feature of the simulation region is the horizontal side needs to be longer than the vertical side, since the line connecting the centers of the two cores is along the horizontal direction. Inside the simulation region, we model the microcoupler structure as two identical cylinders, each one 0.5 μm in radius. The two cylinders have parallel axes and are touching. We assume the microcoupler taper has a uniform interaction region with a constant diameter of 1 μm. The the length of the cylinders are unimportant for our simulation purposes, as long as they are identical, since we assume the modes do not change with propagation. The region enclosing the waveguides is defined with refractive index $n = n_{air} = 1$. The material for the cylinders is chosen to have the refractive index of fused silica, which is calculated via the Sellmeier equation [26].

3.1.2 Solving for the effective mode index

After defining the microcoupler structure, we want to solve for the effective refractive index of each mode. Comsol solves differential equations using the finite element method. The entire rectangular simulation region is discretized with a chosen mesh pattern, and the program solves boundary conditions for each piece of the mesh. We build a nonuniform mesh over the simulation

region, containing both cylinders, as well as the surrounding region with a refractive index of $n = 1$. A nonuniform mesh is selected with the trade-off between precision and calculation time taken into account. In other words, in the regions of interest we want higher precision to make sure we are not missing any features, and we can speed up the calculation when using the solver far away from the structure we want to simulate. The nonuniform mesh is defined so that it is denser around the point of contact between the two waveguides, where we expect the strongest mode coupling. The mesh is looser and each element much bigger in locations away from the waveguides, where we don't expect the modes to exist. This nonuniform mesh we use is shown in Fig. 5.

Next we use the program to perform a parametric sweep, and solve for effective mode index, n_{eff} versus frequency. The simulation data we have goes from 300 nm to 2 μm, in 1 nm intervals. The mode dispersion plot we get from this parametric sweep is shown in Fig. 6. The simulation takes 8 h 57 min 55 s on our simulation computer with Intel Core i5-6400 CPU and 64 GB of RAM.

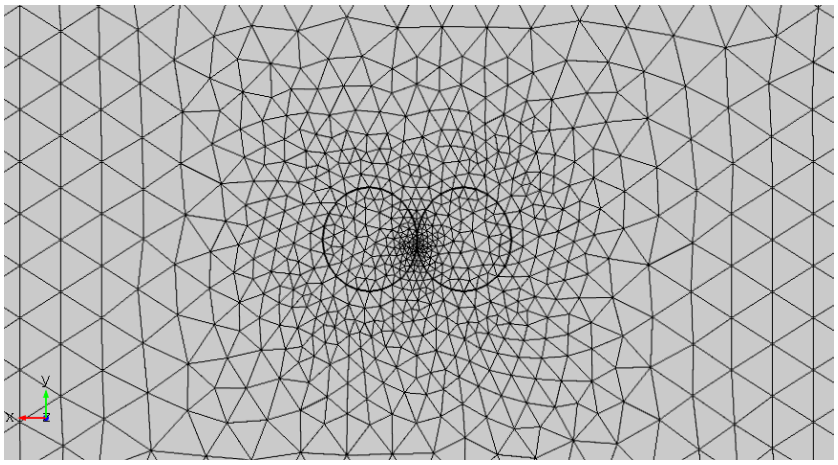

Figure 5: A screenshot from Comsol of the nonuniform mesh we use to calculate the effective refractive indices for each physical mode supported by the structure, zooming in on the microcoupler. In our simulations we model the microcoupler as two identical cylinders kept in contact. The mesh has the greatest density and smallest element size at the point of contact between the two cores. The mesh has a largest element size far away from the microcoupler, near the boundary of the defined simulation region. The nonuniform mesh we use has a maximum element size of 0.5 μm and a minimum mesh element size of 0.005 μm. For the 1 μm-diameter microcoupler, the simulation region is 11 μm by 10 μm. The complete mesh consists of 41480 triangular elements.

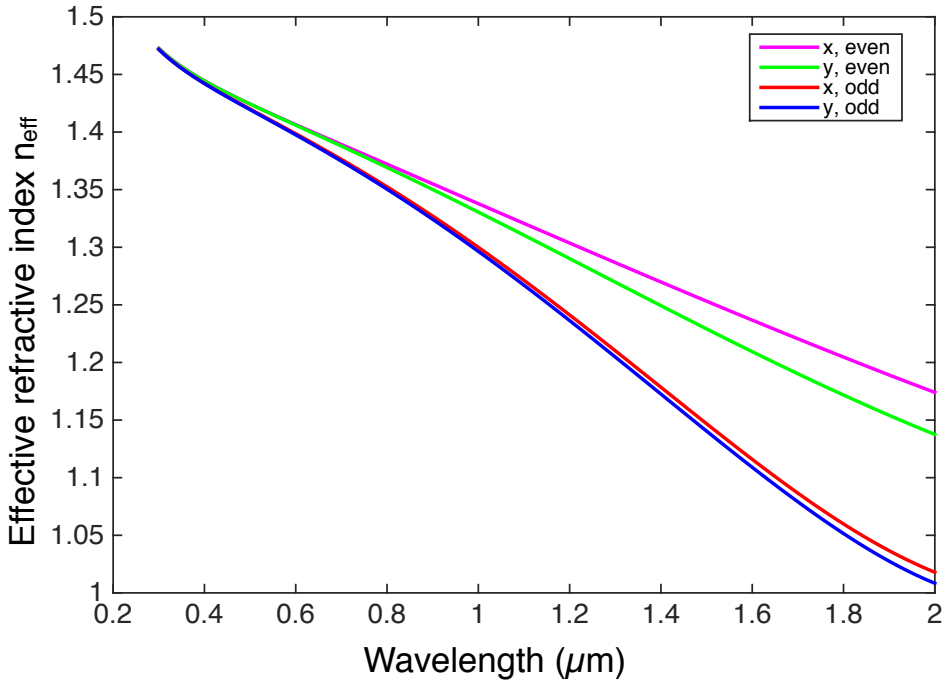

Figure 6: Simulation result for the effective index of refraction, n_{eff}, of each of the four modes, plotted against the pump wavelength. In the order of decreasing magnitude for n_{eff}, the four lowest-order modes of the microcoupler are: x-even, y-even, x-odd, and y-odd. The electric field distributions for these four modes are shown in Fig. 7.

In Fig. 6, we observe the effective refractive indices for the four modes are close in magnitude for shorter pump wavelengths. The splittings become a lot more significant at wavelengths longer than 1 μm. The even-odd mode splittings, or the differences in refractive indices between an even mode and an odd mode, also start to become more evident once we enter the visible wavelength range. The spatial mode splitting is also much larger than the polarization splitting. The reason we see this increase in the even-odd splitting with increasing wavelength could be due to the two modes in the waveguides merging into one, as the pump wavelength becomes comparable with the core diameter. Also, as the pump wavelength gets larger, the single waveguide modes get larger and have a larger evanescent tail. Hence, the overlap of the single waveguide modes will increase. This will result in a larger splitting.

In the next section we will use the data from this plot to solve the 28 different phasematching equations, to see what values the generated SFWM

photon pairs are predicted to have in wavelength. The size of the splittings, shown here among different pairs of modes, are related to the coupling strength and dictate how far apart the generated photons are in wavelength.

3.1.3 Electric field distributions of the microcoupler modes

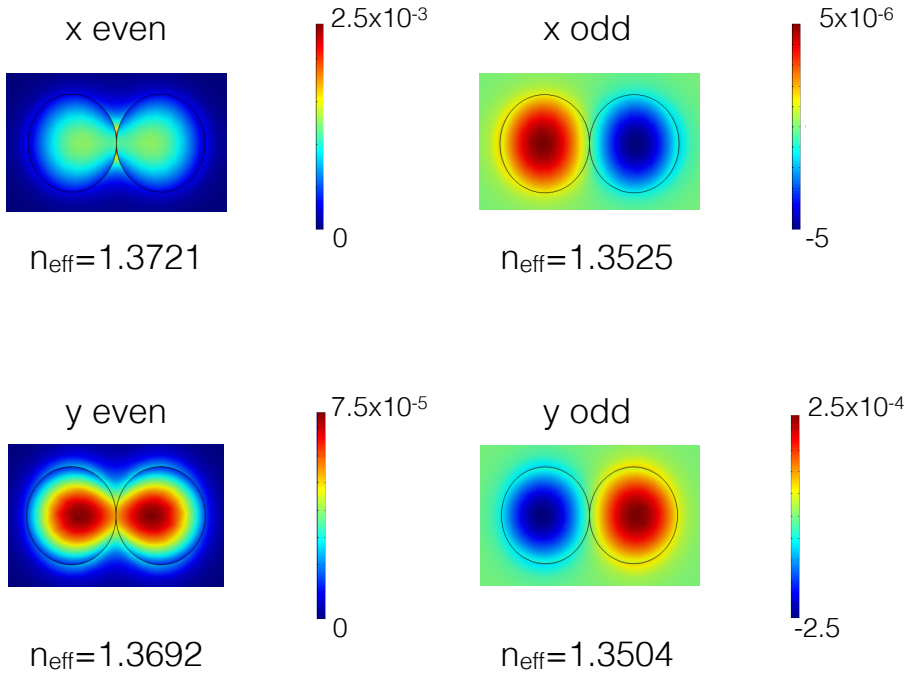

Figure 7: The mode profile distributions of the four modes supported by the microcoupler, using simulation results for a pump wavelength at 800 nm. The black circles represent the outline of each waveguide. The colours show the value of the x-component of the electric field for the two figures in the top row (modes x-even and x-odd), and the colours represent the value of the y-component of the electric field for the two figures on the bottom row (modes y-even and y-odd).

The electric field distributions for each of the four modes are shown in Fig. 7, taken at the pump wavelength of 800 nm. During the simulation, Comsol returns the four modes with the greatest n_{eff} values, and plots the x and y electric field components for each mode. The plots can be seen as cross sections of the microcoupler, with the propagation direction going into the page. To label the modes, we compare the x- and y-components of the electric field distribution. When the x-component is much greater than

the y-component, we label the mode x-polarized. If the electric field vector distribution is symmetric about the vertical axis of the microcoupler, it is labelled as an even mode. If it's antisymmetric, and the distribution in the two waveguides are opposites of each other (out-of-phase by π), it is an odd mode.

In our simulations we ask the program to return the four modes with the greatest effective indices, since we only expect the four fundamental modes of the microcoupler to play a part in phasematching. However, it is also possible that we have excited higher-order modes during our experiment. We can use the same program to solve for more modes, although that comparison is outside of the scope of this thesis. It is also worth mentioning that we use a pump laser at 800 nm in this project, motivated by our goal of generating polarization-entangled photon pairs in the visible wavelength range from a femtosecond Ti:Sapph laser. It would also be of interest to test how the microcoupler performs at longer pump wavelengths, where the mode splittings are greater.

3.2 Phasematching contour plots

Using the results from the Comsol simulations presented in Fig. 6, we solve the phasematching equation, Eq. (4), for the 28 different combinations of modes mentioned in Chapter 2. The plots of the solutions to Eq. (4) make up the focus of this section.

The phasematching plots are generated using Mathematica. After importing the Comsol simulation results of the wavelength-dependent effective refractive indices for the four modes, we perform an interpolation of each dataset. The interpolation function is a piecewise third order Hermite polynomial. We then rewrite the effective refractive index n_{eff} in terms of the propagation constant β for each mode, using $\beta = k = 2\pi n/\lambda$ and $\omega = 2\pi/\lambda$.

The next step in making the phasematching plots is defining a simulation domain. This is necessary to avoid automatic extrapolation of the interpolated effective index function when the program tries to find solutions outside of the region where we have Comsol simulation data. The Comsol simulations calculated the effective indices for wavelengths between 300 nm (λ_1) and 2000 nm (λ_2). We restrict the domain for the plot to a diamond shape

restricted by boundaries as follows:

$$\begin{aligned} edge_1(\lambda) &= \lambda - \lambda_1, \text{ from } \lambda_1 \text{ to } \tfrac{\lambda_1+\lambda_2}{2}, \\ edge_2(\lambda) &= -\lambda + \lambda_1, \text{ from } \lambda_1 \text{ to } \tfrac{\lambda_1+\lambda_2}{2}, \\ edge_3(\lambda) &= -\lambda + \lambda_2, \text{ from } \tfrac{\lambda_1+\lambda_2}{2} \text{ to } \lambda_2, \\ edge_4(\lambda) &= \lambda - \lambda_2, \text{ from } \tfrac{\lambda_1+\lambda_2}{2} \text{ to } \lambda_2. \end{aligned} \tag{39}$$

Next we define the phasematching equation in terms of $\beta(\omega)$ which we calculated from the $n_{eff}(\lambda)$ data earlier. We write 28 of these equations for the 28 unique phasematching situations predicted by theory, and make a plot for each. We chose to run the simulation in Comsol over a broad range of pump wavelengths because the idler and signal can be far from the pump so we need n_{eff} over a wide range of pump wavelengths. We are also looking at generating photon pairs using microcouplers with a tunable pump laser as a future option. The simulation domain is visualized as a diamond shape with black dashed lines as the outline.

The pump frequency is plotted on the horizontal axis. The splitting between either one of the signal and idler frequencies and the pump frequency is labelled as $\Delta\omega = |\omega_s - \omega_p|$. When $\omega_s = \omega_p - \Delta\omega, \omega_i = \omega_p + \Delta\omega$, and vice versa. The signal and idler frequencies are symmetric over the horizontal dashed line where $\Delta\omega = 0$. On the dashed line, the signal and idler are within the pump bandwidth, and cannot be observed.

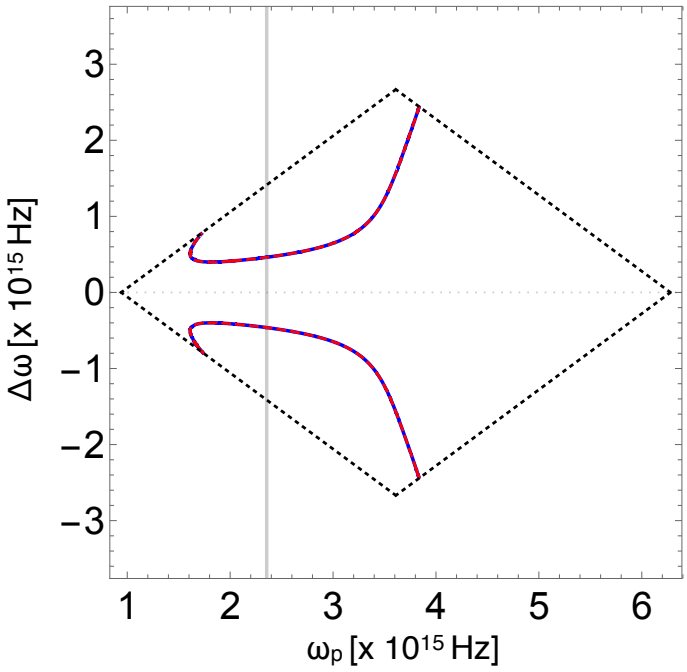

Figure 8: A phasematching contour plot for the microcoupler of core diameter 1 μm. This phasematching process involves two y-odd pump photons as the input, and generates signal and idler photons both in the x-odd mode. The horizontal axis shows the pump frequency, multiplied by 10^{15} Hz. The vertical axis shows the splitting $\Delta\omega = |\omega_s - \omega_p|$ between the pump and the generated photon, also multiplied by 10^{15} Hz. On the horizontal dashed line where $\Delta\omega$ is zero, the generated photons are the same frequency as the pump. The signal and idler frequencies are symmetric about this dashed line. The solid vertical line shows the pump frequency for our 800 nm pump. In this case there are two solutions at pump frequency, 668.75 nm and 995.34 nm. The pink solid line plots $\omega_s = \omega_p + \Delta\omega$, while the blue dotted line plots $\omega_s = \omega_p - \Delta\omega$.

The full set of 22 unique phasematching processes that give solutions for the 1 μm-diameter microcoupler is shown in the appendix.

3.3 Analysis of phasematching solutions

Once we have generated the 28 phasematching plots, we are able to find the predicted signal and idler photon wavelengths for a variety of pump wavelengths. We would like to learn more about how these predictions will change when certain parameters are varied. We also want to find out whether some of the allowed phasematching processes can occur simultaneously in the microcoupler, using the same pump wavelength. The situation we are most

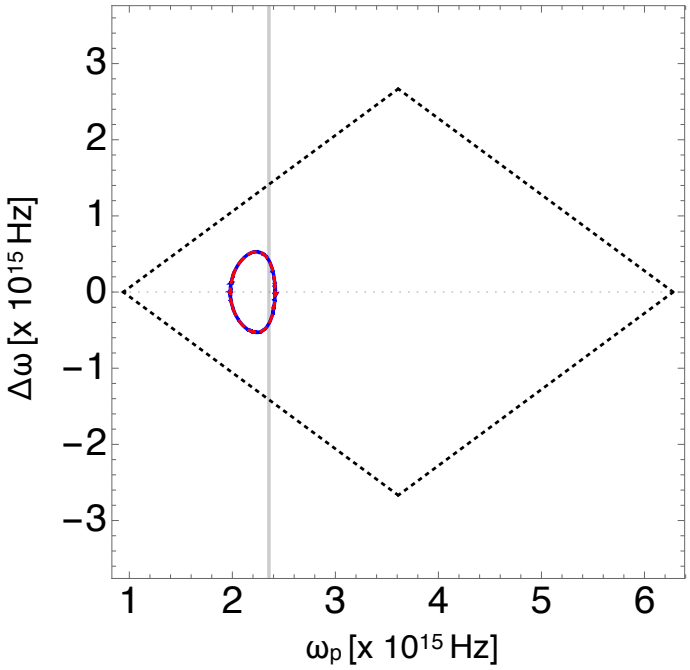

Figure 9: A phasematching contour plot for the microcoupler of core diameter 1 μm. The four modes involved in this phasematching process are all x-even. The horizontal axis shows the pump frequency, multiplied by 10^{15} Hz. The vertical axis shows the splitting $\Delta\omega$ between the pump and the generated photon, also multiplied by 10^{15} Hz. The solid vertical line represents the pump frequency for our 800 nm pump. In this case there are two solutions at pump frequency, 680.01 nm and 971.34 nm. The pink solid line plots $\omega_s = \omega_p + \Delta\omega$, while the blue dotted line plots $\omega_s = \omega_p - \Delta\omega$. We expect the two contours to overlap because the solutions are symmetric.

interested in is when certain phasematching processes occur simultaneously and generate photon pairs at the same wavelength. In this case we would have generated entangled photons, if the photons generated via the two processes are indistinguishable in either polarization or spatial modes. For example, if two phasematching processes generate a horizontally-polarized signal photon at 650 nm, we would not be able to distinguish the two signal photons at the same detector. More specifically, we would like to be able to generate polarization-entangled photon pairs because they are useful in quantum optics experiments.

To start with, we overlaid some phasematching plots to see if they have intersection points at wavelengths we could detect. We checked 10 pairs of solutions to see if there are intersection points. What we find was for a core diameter of 1.0 μm, the intersection points mostly occur for pump wavelengths lower than 400 nm. We have a tunable Ti:S pump that can be used from 650 nm to 1080 nm. It might not be practical even if we can get another laser because light below 400 nm can be absorbed by the silica waveguide itself. And since there are 28 phasematching plots, there are $27! \approx 1.09 \times 10^{28}$ total possibilities in combining each pair of them, which will take a long time to go through. The process of reading the plots to select which two are more likely to lead to entanglement is also not automated. In the interest of time, we decide to do the experiment first and then check if we detect photon pairs near intersection points for certain processes.

3.3.1 Measuring the core diameter with Scanning Electron Microscopy

A more immediate concern for us is the uncertainty in the core diameter of the microcoupler taper. At this time we do not have an ideal method for measuring the diameter of the fabricated microcoupler. We know using the same tapering setup to fabricate similar structures for telecom fibers leads to an uncertainty of less than 5 % in the diameter [31]. We have taken images of a broken microcoupler taper using a scanning electron microscope, and some of the results are shown in Fig. 10. However, during the imaging process we encountered multiple issues such as charging of the dielectric, as well as difficulty in preparing the taper sample for imaging. We do not have a method for marking different sections of the taper as the taper is very fragile, thus the segment we image could be from the transition region near the end of the taper instead of the waist.

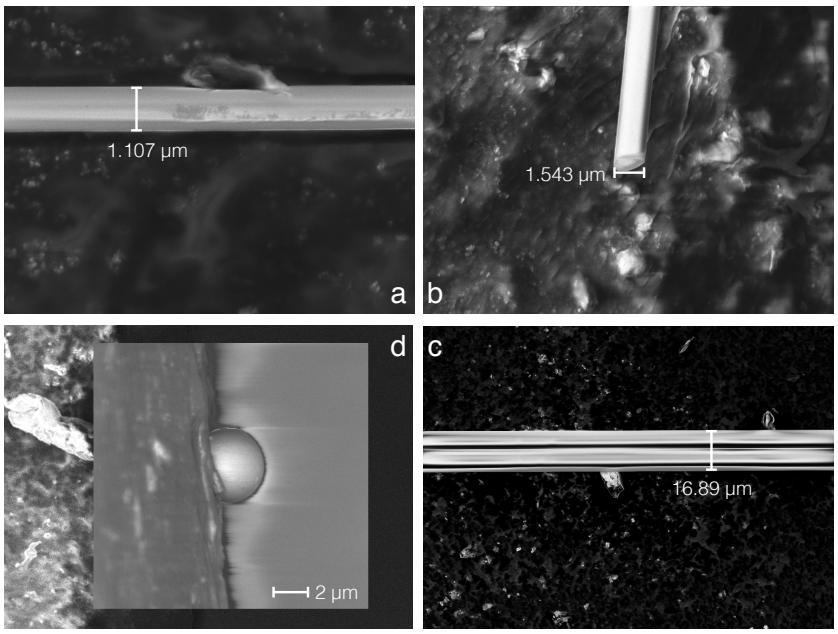

Figure 10: Scanning electron microscope (SEM) image of different parts of broken microcoupler segments. The accelerating voltage is 5 kV, working distance (WD) 5 mm, aperture size 30 µm. Clockwise from the top-left corner: a. Top view with 6.86×10^3 *times the magnification. The diameter is measured to be 1.107 µm. b. The diameter is measured to be 1.543 µm at the broken interface, with magnification* 5.57×10^3 *X. c. The cross section of a broken microcoupler segment. The piece is embedded in the carbon tape so we cannot get a good measurement on the diameter. The magnification was* 5.04×10^3 *X. d. Top view of the segment with magnification 668X, where the diameter is measured to be 16.89 µm. This is likely the transition region near the ends of the taper where the diameter is larger. The two adjacent fiber cores are visible.*

Due to concerns about the uncertainty in the core diameter affecting our predictions, we are interested in checking how much variation there would be in the simulation results if the core diameter is varied as an input. In Fig. 11 we present a few examples comparing phasematching contour plots for the same processes, with the microcoupler core diameter the only parameter altered.

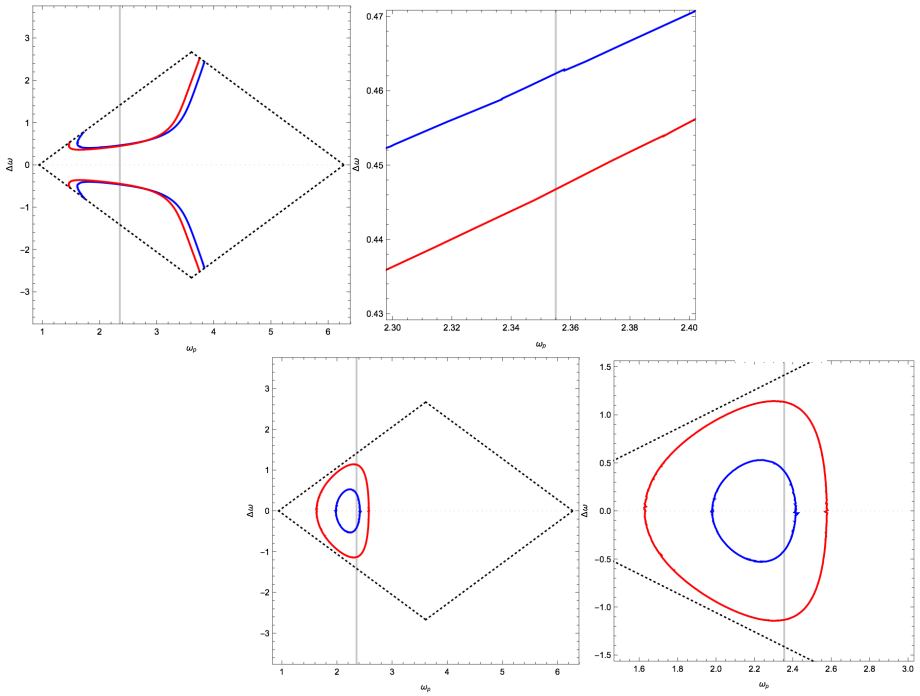

Figure 11: Simulation data for the two phasematching processes shown in Figs. 8 and 9, with the same axes but changing the core diameter. The vertical line still signifies the pump frequency. The original simulation result for a core diameter of 1 μm is shown in blue, while another set of data for core diameter of 1.1 μm is shown in red. The two figures on the right are zooming in on the intersections between the curves and the vertical line representing the 800 nm pump. The two processes are y-odd + y-odd $\rightarrow$ x-odd + x-odd on top, and all x-even on the bottom. The original solutions for our 800 nm pump are at 688.75 nm and 995.34 nm, and 680.0 nm and 971.3 nm, respectively. The new solutions are 672.4 nm and 987.3 nm, and 539.9 nm and 1544.0 nm. These plots show varying the core diameter can have a significant effect on our predictions for the generated photon pairs.

3.3.2 Alternative methods for core diameter measurement

More recently, we learned about better methods for measuring the diameter of the microcoupler. One option is using an optical microscope. Another option is depositing gold or platinum on the taper, before measuring it using an SEM. At the time of writing, it is possible to do the destructive measurement on the actual microcoupler prototype we used to get experimental results. This step is beyond the scope of this thesis, but would be one of the first steps suggested for future work on the microcoupler.

3.4 Conclusion

In conclusion, an overview of the numerical simulation method based on the unique microcoupler structure is presented in this chapter. We simulated the microcoupler structure as two identical cylinders in parallel, and solved for the four modes with the largest effective refractive indices as a function of wavelength. The four modes carried by the microcoupler, *x-even, x-odd, y-even, y-odd*, have different refractive indices as expected from mode splittings due to the geometry.

We also explain the purpose of the phasematching solution plots and how they were generated. We solved the 28 unique phasematching situations predicted in Chapter 2 for a microcoupler diameter of 1 μm, and generated a plot for each case that has a solution at this diameter. For each given pump frequency in a phasematching plot, we can read off the frequency difference between the pump and the generated photons, $\Delta\omega$, from the plot, and calculate the corresponding signal and idler wavelength. This prediction helps us decide where to look for the generated photon pairs on the spectrometer. As shown in the next chapter, not all the daughter photon wavelengths predicted by phasematching are practical experimentally. This is because some photon pairs would occur too close to the pump spectrum and be filtered out, or too far away from the pump and end up outside the detection range of our spectrometer. The prediction results also provide directions in improving the design of the microcoupler.

The experimental aspects of this thesis will be described in more detail in the next two chapters. Chapter 4 describes the major experimental considerations that took place when fabricating and characterizing the microcoupler. Chapter 5 details the various stages of the experimental process of photon-pair generation.

4 Microcoupler characterization

Having talked about how we model the microcoupler in the previous chapter, we now take a closer look at the microcoupler itself. This chapter describes the design and fabrication of the microcoupler, before going on to characterize its properties of interest. Having a better understanding of the microcoupler design and properties helps put the experiment in Chapter 5 in context.

The first section of this chapter describes the microcoupler structure in detail, including the fabrication process. It also describes the reasoning behind a few experimental decisions that we made. Because we can fabricate microcouplers of different designs using the same setup, we are interested in estimating how much input power is required for each microcoupler design. Chapter 4.2 contains the derivations for estimating the average input power required for generating a measurable number of photon pairs. Later on we used this estimated power limit as a guide when testing another microcoupler with a bigger diameter. Another test we did before generating photon pairs was trying to characterize the polarization mode splittings of the microcoupler, using a method similar to measuring the birefringence of a birefringent fiber. This test is described in Chapter 4.3.

4.1 Design and fabrication

The fabrication process for the microcouplers took place in Xiaoyi Bao's fiber optics lab at the Advanced Research Complex, 25 Templeton Street, University of Ottawa. The tapering setup was built by Chams Baker who also performed the fabrication during which I helped.

As mentioned before, the microcoupler is composed of two single mode fibers (SMFs) tapered while kept in contact. We designed it to have a minimum diameter of 1 μm. What we call the effective length, which is the extent of the uniform interaction region with 1 μm diameter, is 10 cm long. We made the microcoupler out of SM600 fiber manufactured by Fibercore. It has a numerical aperture (NA) ranging from 0.10 to 0.14, mode field diameter (MFD) from 3.6 to 5.3 μm at 633 nm, core diameter of 125 μm.

The actual microcoupler structure has two transition regions, one on each side of the uniform region, as a result of the tapering process. In the transition region, the diameter of each core changes rapidly from the diameter of a standard SMF (125 μm cladding diameter according to Thorlabs spec sheet) to 1 μm. This transition region is ignored in our theoretical model for the

microcoupler in Chapter 3.

4.1.1 Fabrication: sample preparation

The fabrication process has three main steps: sample preparation, tapering, and packaging. During the sample preparation step, two identical SM600 fibers are cleaved, cleaned, then fixed on the tapering setup. One piece of fiber is significantly longer than the other. A diode laser for monitoring the power transmission is coupled into one end of the longer fiber. The output end of the same fiber is sent to a detector. In this case we used a photo resistor with an ohmmeter as the read out, but a power meter would be suitable also. The shorter fiber is twisted around the long fiber once, so that they would stay close together while heated from below. The fibers are held in place at both ends on the plexiglass mount specially made for the tapering setup. The bottom of the mounts are automated and the motors are controlled via a LabVIEW virtual instrument (VI) interface. The longer fiber is also secured on the same mounts.

4.1.2 Fabrication: tapering

During the tapering process, a hydrogen flame heats the two fibers from below. An automated LabVIEW program moves the flame back and forth on a motorized stage, and also moves the mounts at both ends of the two fibers slowly apart. The program adjusts to gradually heat over a longer region, as the fibers get stretched longer. Meanwhile the power transmission through one fiber is monitored on the same LabVIEW program. The program plots the power in one core against the extension. The extension is defined as how much the two mounts have moved away from their initial position before the fiber was heated and stretched. An example of the LabVIEW fabrication data is shown in Fig. 12 for a microcoupler of diameter 7 μm.

The power transfer cycles seen in Fig. 12 result from the mode coupling between two cores of the microcoupler. These oscillations are a direct representation of the constructive and destructive interference between the symmetric and anti-symmetric composite modes. The oscillation frequency is based on the difference in effective indices between the modes. Thus we can use this data to estimate the size of the mode splittings. Since we are only monitoring one of the two output ports, the oscillating pattern shows the power entering and leaving the monitored core, as it beats back-and-forth

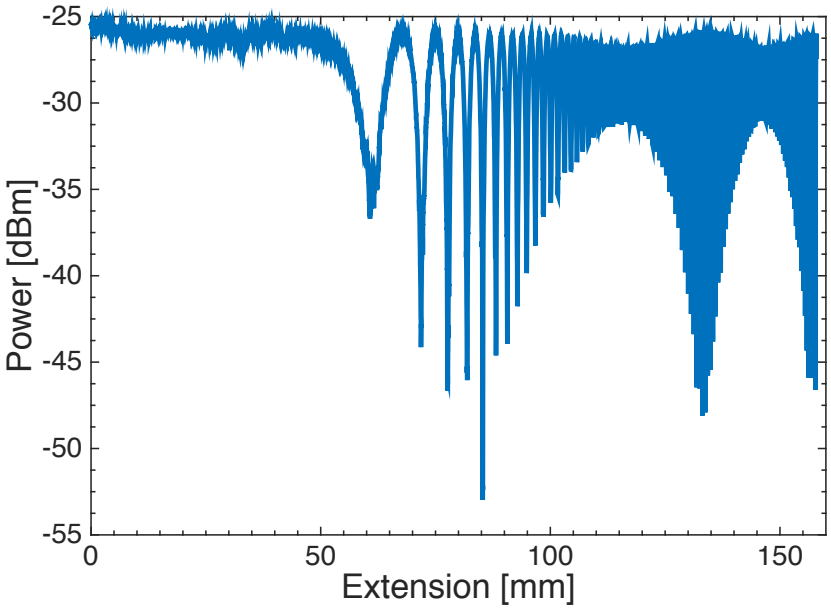

Figure 12: Real-time fabrication data from the automated LabVIEW program for a 7.3 μm microcoupler. The vertical axis is the power in one waveguide measured in decibels (dB), the horizontal axis is the extension of the tapered region, measured in millimeters (mm). The effective interaction length of this microcoupler is 83.3 mm. This fabrication data is obtained in collaboration with Chams Baker.

between the two cores. This plot also helps us monitor the taper in real-time, since the power transfer would be zero if the taper breaks.

For the first batch of microcoupler prototypes, we monitored the power transmission through the tapered SM600 fiber with a 633 nm diode laser. However, when testing the first microcoupler in our experimental setup with our Ti:Sapph laser at 800 nm, the transmission was poor. When we tested a Thorlabs SMF 630 (made of the same SM600 fiber used for the microcoupler), the difference in the transmission for 633 nm and 800 nm lasers is negligible. It is likely that for the smaller core diameter of the two waveguides in the microcoupler, longer wavelengths are not as well-guided. We decided to monitor the transmission with a laser close to 800 nm instead. Keeping the rest of the fabrication setup the same, if the selected 1 μm core size does not transmit 800 nm light well, we would need to change the design. For this second batch of 1 μm microcoupler, we used a diode laser at 810 nm to monitor the power transmission, and the total transmission was over 90 %. The experimental results presented in the next chapter were taken on

a microcoupler of the second batch, fabricated using the 810 nm laser.

The tapering process is also monitored against theoretical calculations. The prediction of particular interest to our SFWM experiment is the diameter of one core versus the extension. The tapering process is terminated when the tapered fibers have reached the desired core diameter. An example of the relationship between the core diameter and the taper extension for the 1 μm microcoupler is shown in Fig. 13.

Since the cutoff is decided based on the core diameter, the power transmission ratio between two output ports on the same side of the microcoupler is random. This is partially due to the fact that only one output port is monitored during fabrication. It is possible to control the transmission ratio if we stop the tapering process and cut the fiber at certain positions on the power transmission plot (Fig. 12). For example, choosing to end the taper at a power transmission peak would result in almost 100 % transmission in one output port. The transmission ratio between the two output ports is not immediately a concern because we are only using one output port to detect the generation of SFWM photons. In our experiment the transmission of all the combinations of input/output ports are measured, and the two ports with the highest transmission ratio are selected as the input and output. However, controlling the transmission ratio of the two microcoupler output ports during fabrication might be worth investigating for future work, especially if both output ports are to be measured simultaneously when looking for entanglement of the generated photons.

4.1.3 Fabrication: packaging

It is worth noting that the entire tapering setup is kept inside a plexiglass box to minimize contamination from dust. Having dust particles attach to the fragile taper region makes the microcoupler a lot easier to break. This could partially be due to the dust particles weighing the taper region down, but is more likely due to the particle heating up when a laser beam is sent through the microcoupler. In the latter case, the dust particle would heat up, causing the taper to melt and break.

The vulnerability to dust also makes the packaging process after tapering somewhat difficult. Ideally, once the flame is turned off the taper should immediately be enclosed with the custom-made plexiglass packaging. In reality, there is a wait time anywhere from a few seconds to under a minute during

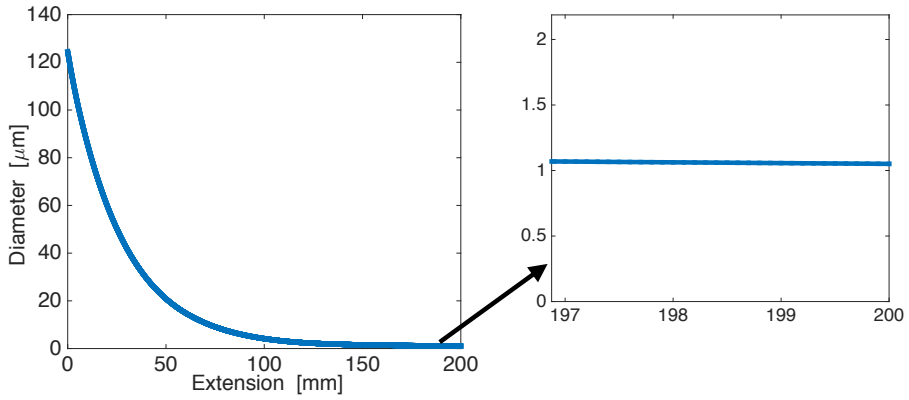

Figure 13: An example of theoretical calculations used during the fabrication of the microcoupler. This plot shows the calculated core diameter versus taper extension. The zoomed-in version is shown on the right. It predicts at a taper extension length of 200 mm, the core diameter of each tapered waveguide of the microcoupler is 1.05 μm.

which the packaging is prepared and moved into the tapering setup. One reason why it is more likely for the taper to collect dust particles immediately after the tapering process ends, rather than earlier, is that when the taper is heated from underneath, heat would blow away dust that is falling down towards the taper due to gravity. And since the fabrication process does not take place in a clean room, it is almost unavoidable for the taper to catch dust when the microcoupler is being packaged, cleaved and moved outside of the box protecting the entire tapering setup.

Thus the packaging process, which is not automated at the moment, is the most error-prone step in our microcoupler fabrication process. We have seen improvements in the microcoupler performance such as higher transmission and sturdier microcouplers when the fabrication process is improved. Some of the improvements include moving to a cleaner lab, starting to prepare the packaging right before turning off the hydrogen flame, and better organization around the tapering setup.

4.2 Peak intensity required for SFWM in microcoupler

One of the main properties of the microcoupler we need to characterize before proceeding to design the experiment is how much input power can be sent in. In fact, we need to estimate the average input power each time we switch to a microcoupler of different design. Since it takes time to fabricate each microcoupler, we do not want to start by testing the microcoupler until it breaks to find the damage threshold. In addition to the damage threshold of the structure itself, we are also concerned with how much input power is needed in order for SFWM to be observed in such a structure. Even though theoretically the photon-pair generation process does not have a threshold, in practice the generated photons can be too low in intensity to show up on the detection equipment. In our particular case of using a spectrometer, the signal and idler peaks could be hidden in the noise floor or obscured by the Raman noise.

In order to get an estimate of the minimum input power needed for the observation of SFWM, we compared the microcoupler with a photonic crystal fiber (PCF) on which SFWM was observed [38]. We selected this comparison because the PCF used has a core diameter of 1.75 μm which is similar to our first microcoupler sample (1 μm in diameter for each core). In the rest of this section we calculate an estimate of the average input power, P_{avg}, needed for the microcoupler based on how much peak intensity was required for SFWM to be detected in the PCF.

4.2.1 Peak intensity required for SFWM in a PCF

As in the general SFWM case in Chapter 2, Eq. (5), we start by defining a parameter R related to the peak intensity and the effective length of the fiber, $R \propto (I_{peak})^2 L$. R is proportional to the pair generation rate [29]. The peak intensity is proportional to:

$$I_{peak} \propto (\frac{1}{\Delta t})(\frac{1}{r^2})E_{pulse}, \tag{40}$$

while

$$E_{pulse} \propto \frac{P_{avg}}{\Gamma_{rep}}, \tag{41}$$

where Δt is the pulse duration, E_{pulse} is the pulse energy, r is the waveguide radius, and Γ_{rep} is the repetition rate of the laser.

The PCF used for comparison is 40 cm in length. The laser used has a pulse duration of 50 fs, with repetition rate 76 MHz, and an average input power of 1 mW [38]. Substituting these parameters into the equations above, we can get an estimate for the peak intensity and R:

$$\begin{aligned} I_{peak} &\propto (\tfrac{1}{50\ \text{fs}})(\tfrac{1}{(1\ \mu m)^2})(\tfrac{1\ \text{mW}}{76\ \text{MHz}}), \\ &\approx 2.6 \times 10^{15}\ \text{W/m}^2 \end{aligned} \tag{42}$$

and

$$\begin{aligned} R &\propto (2.6 \times 10^{15}\ \text{W/m}^2)^2 \times (0.4\text{m}) \\ &\approx 3 \times 10^{30}\ \text{W}^2/\text{m}^3 \end{aligned} \tag{43}$$

As mentioned earlier, our goal in making this estimation is to find out what average power we need to send to the microcoupler to reach the same R-value, or the same generation rate, at which SFWM photons have already been observed. The reason we choose to vary the input power first is that it is experimentally easier than varying the core size or interaction length of the microcoupler by a large amount. For a microcoupler with larger core size, we will need more input power (P_{avg}) to reach the same peak intensity (I_{peak}), and the same generation rate (3×10^{30} W/m in this case). The minimum power required for a microcoupler 7 μm in diameter is calculated later in this section.

As shown, the generation rate of SFWM photons depends on the core size or mode size of the waveguide, the pulse length of the pump, the average input intensity, the fiber length or taper(interaction) length.

Now we solve for the average power required for the 1μm microcoupler to reach the same photon-pair generation rate. From Eqs. (40) and (41), we have

$$\begin{aligned} P_{avg} &\propto E_{pulse}\Gamma_{rep}, \\ P_{avg} &\propto I_{peak}\Delta t' r^2 \Gamma_{rep}. \end{aligned} \tag{44}$$

Our microcoupler has 10 cm of interaction length. The peak intensity required to get the same generation rate is

$$\begin{aligned} I_{peak} &\propto \sqrt{R/L} \\ &\approx \sqrt{(3 \times 10^{30}\ \text{W}^2/\text{m}^3)/(0.1\ \text{m})} \\ &\approx 5.5 \times 10^{15}\ \text{W/m}^2. \end{aligned} \tag{45}$$

Our laser pulse duration is 100 fs, with repetition rate 80 MHz. If we assume zero group velocity dispersion for now ($\Delta t' \approx \Delta t$), we can find the

minimum average power required for SFWM to be observed in this microcoupler with radius 0.5 μm:

$$P_{avg} \approx (5.5 \times 10^{15}\ \mathrm{W/m^2})(100\ \mathrm{fs})(0.5 \times 10^{-6}\ \mathrm{m})^2(80 \times 10^{6}\ \mathrm{s^{-1}})$$
$$P_{avg} \approx 11\ \mathrm{mW}, \tag{46}$$

which is a practical input power for our experiment.

4.2.2 Effects of pulse dispersion on peak intensity estimation

In reality, we cannot achieve zero group velocity dispersion. This is because before the pump laser pulse enters the interaction region of the microcoupler, it needs to first enter a finite length of fiber. Each of the four ports on the microcoupler has a segment of single mode fiber outside of the tapered region. After the fabrication and packaging process, the fiber segment on the input port is spliced onto another connectorized single mode fiber for easy fiber coupling during use. Both fibers are of the same type (SM600). The same splicing procedure is repeated for the other three input or output ports. There is a minimum length of the splice required due to mechanical limitations in operating the splicer. The total length of the splice on the input port of the microcoupler is close to 30 cm, which includes both the segment of the fiber originally on the microcoupler, and the short fiber with a connector on one end. In addition, we also needed a short fiber segment that is connectorized on both ends to optimize the coupling into the microcoupler. We spliced two ends of a commercial fiber to get this 15 cm segment. The purpose of this short fiber will be described more in Chapter 5 which details the experimental procedure. We calculated the dispersion of the pump pulse in this additional fiber before the interaction region of the microcoupler. The prediction is shown in Fig. 14.

This dispersion changes the pulse duration of the pump when it reaches the uniform interaction region, or the effective length of the microcoupler with minimum core diameter. The pulse duration in free space, Δt, is 100 fs. But according to Fig. 14, after dispersion due to 50 cm of fiber, $\Delta t'$ becomes 630 fs. We have experimented with the splicing process and around 50 cm of total additional fiber is the minimum length we can get with our equipment. In the experiment we also try to mitigate this dispersion by making the pump bandwidth narrower.

Using the predicted pulse duration value after dispersion and keeping other parameters the same, we calculate the minimum average input power

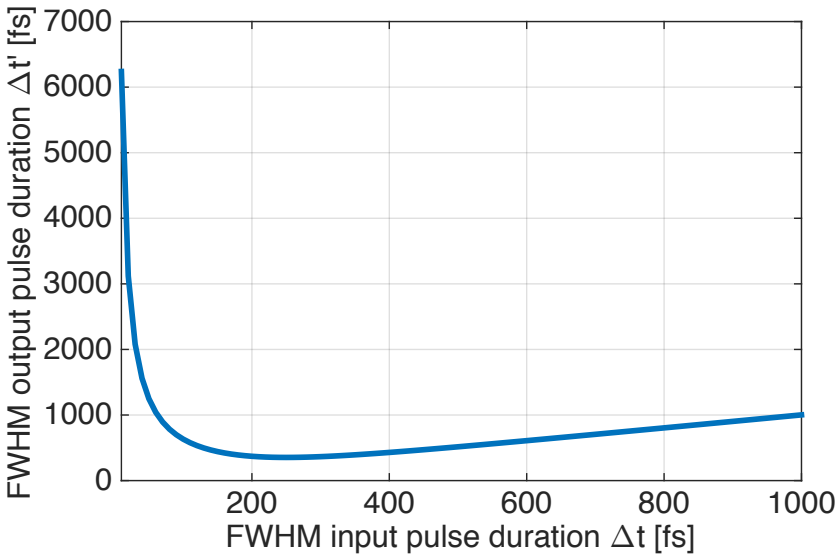

Figure 14: Estimated dispersion in 0.5m of SM600 single-mode fiber, assuming group delay dispersion $\phi(2) = 45000$ fs^{2}m^{-1} and a Gaussian pulse shape. For an input pulse duration of 100 fs, we estimate the output pulse duration to be 630 fs, after the 0.5 m of additional fiber before the microcoupler.

again, in comparison with the result in Eq. (46):

$$\begin{aligned} P_{avg} &\approx (5.5 \times 10^{15})(632 \text{ fs})(0.5 \times 10^{-6} \text{ m})^2(80 \times 10^6 \text{ s}^{-1}) \\ P_{avg} &\approx 69.5 \text{ mW}. \end{aligned} \tag{47}$$

This value turned out almost 7 times greater than the average input power for the PCF we used to get an estimate [38], but is still a realistic value for our experiment. The main factors that lead to a requirement for a higher average power in this comparison include shorter interaction length of the microcoupler, and more dispersion due to the additional fiber before the interaction region.

4.3 Mode splitting measurement

In Chapters 2 and 3 it was shown that the coupling and splitting among the four modes supported by the microcoupler is its most promising feature. We are interested in the splitting between these modes in both the polarization and spatial degrees of freedom, because we would like to generate

polarization- and spatial mode-entangled photon pairs using the microcoupler. Starting with polarization, the degree of freedom we are more familiar with experimentally, we can measure the splitting between the two birefringent polarization modes.

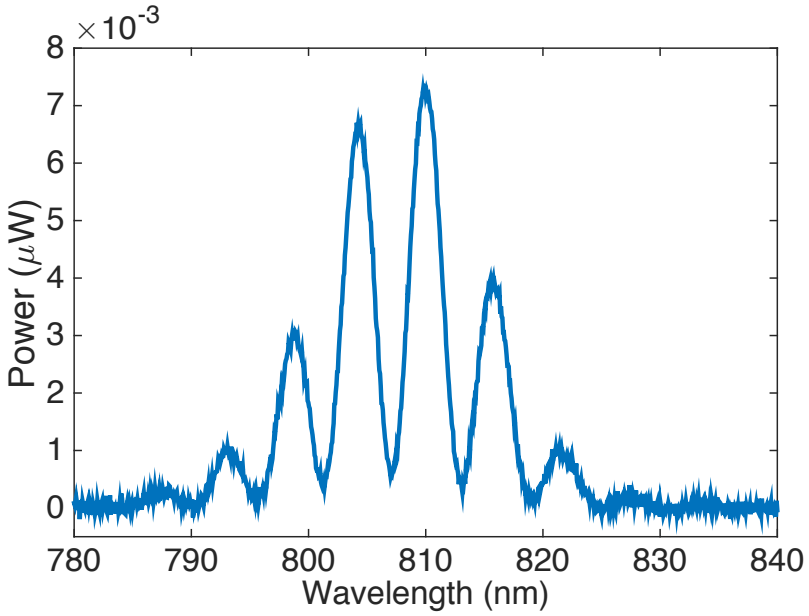

Figure 15: Polarization interference fringes measured on a standard birefringent fiber, in order to calculate its birefringence. The setup consists of a half-wave plate (HWP), birefrigent fiber, followed by another half-wave plate and a PBS to mix the two polarization modes. We set the HWPs to send in 45-degree polarized light. This is because we need to mix the two orthogonal polarizations in order to get maximum interference fringe visibility. We detect the spectrum after the microcoupler using an optical spectrum analyzer (OSA). The fringes are due to interference between the horizontal (H) and vertical (V) polarization components. The spacing, $\Delta\lambda$, between the two adjacent fringes is 5.64 nm. The fiber used is a polarization-maintaining (PM) fiber manufactured by Newport. The fiber has a length of 20 cm, with measurements taken at input power 10.1 mW, using a Yokogawa AQ6370C optical spectrum analyzer with resolution 0.02 nm.

4.3.1 Polarization mode splittings of the 1 μm microcoupler

In Chapter 2.2.2 we derived how to find the birefringence, Δn_{xy}, of a standard birefringent fiber using measurements of its interference fringe spacing

$\Delta\lambda$. Sample data of the interference fringes of a birefringent fiber is shown in Fig. 15. We measured the interference fringe spacing of a commercial polarization-maintaining (PM) fiber, and calculated its birefringence. We repeat the method used for the birefringent fiber for the 1 μm microcoupler, to find its polarization mode splitting Δn_{xy}.

We can apply this method when we are only considering the case where the two polarization modes involved have the same spatial mode. For example, $\Delta n_{xy} = n_{x,odd} - n_{y,odd}$, or $\Delta n_{xy} = n_{y,even} - n_{x,even}$. In these cases the interference fringes we observe would be due to the two polarization modes only. Furthermore, this method applies only when we assume the effective refractive index does not change quickly with frequency, so that we can set the group index equal to the phase index. The definition for the group index is shown in Eq. (48). We calculate the group index, n_g, from the measurement of interference fringe spacings, while the phase index $n(\omega)$ for each mode is obtained from the Comsol simulation results as the effective mode index.

$$\begin{aligned} n_g = \frac{c}{v_g} = c\frac{\partial k}{\partial \omega} = \frac{\partial}{\partial \omega}(\omega\ n(\omega)) \\ = n(\omega) + \omega\frac{\partial n}{\partial \omega}. \end{aligned} \tag{48}$$

To measure the birefringent mode splittings of the microcoupler, we want to observe interference fringes between the x and y polarizations. We know the Glan polarizer only transmits horizontal or vertical polarization. So immediately after the Glan polarizer and before the microcoupler, the pump polarization is linear. We then rotate the polarization by 45 degrees using a half-wave plate, to send in a mixture of the two orthogonal polarizations. We put a polarizing beam splitter (PBS) at the output of the microcoupler to mix the modes, in order to get maximum visibility in the interference fringes. This polarizer functions as the HWP and PBS after the birefringent fiber in the previous measurement in Fig. 15. We also add a quarter-wave plate before the microcoupler to compensate for the effects on the polarization caused by the additional fibers spliced to the microcoupler. In reality, these fibers can rotate the polarization from linear to elliptical, and the orthogonal x and y polarizations in the microcoupler would not exactly correspond to the horizontal (H) and vertical (V) polarization states. The mode splitting measurement result for the 1 μm microcoupler is shown in Fig. 16. Similar to the birefringent fiber, we can use the interference fringe spacing to calculate the mode splitting.

We used the USB2000+VIS-NIR spectrometer from Ocean Optics. It has a resolution of 1.5 nm at full width at half maximum (FWHM), and a detec-

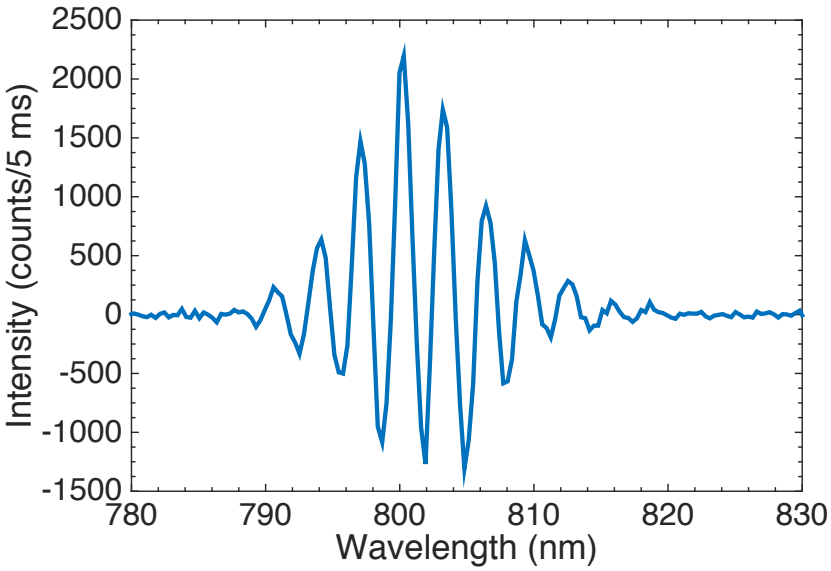

Figure 16: Corrected interference fringes measured on the 1 μm microcoupler, in order to calculate its polarization mode splittings. The setup consists of a half-wave plate (HWP), the microcoupler, a polarizer before neutral density (ND) filters and an Ocean Optics spectrometer. The HWP and polarizer angles are varied to first maximize and then minimize the fringes. We obtain the corrected fringes by subtracting the dataset with minimum fringes from the dataset of maximum fringes. The fringes are due to interference between the x and y polarization components. In this measurement we cannot completely isolate the polarization mode splittings from the inherent spatial mode splittings of the microcoupler geometry. Thus we perform the correction for better visibility of the fringes. The fringe spacing, $\Delta\lambda$, between the two adjacent fringes is 3.13 nm. The data is taken with input power 15 mW, integration time of 5 ms, using an Ocean Optics spectrometer with resolution 1.5 nm FWHM. We expect multiple sets of fringes due to the splittings among the different modes, and the resolution might be too low for our purposes.

tion range from 350 to 1000 nm. We observe one set of interference fringes for the 1μm microcoupler within the 20 nm bandwidth of our pump. The wavelength separation between two closest fringes translates into a splitting between two modes. The fact that we only see one set of fringes is surprising, as we were expecting to see multiple sets of fringes corresponding to many mode splittings predicted in theory. The birefringent fiber only supports two polarization modes, thus it only has one birefringent mode splitting. Since the microcoupler supports four modes across two degrees of freedom, at the very least we should have one set of polarization mode splittings, and another set of spatial mode splittings. For example, $\Delta n_{xy} = n_{x,odd} - n_{y,odd}$, and $\Delta n_{eo} = n_{y,even} - n_{y,odd}$. At this point in the experiment we did not know the relative magnitudes of the four mode indices, as the simulations were in progress.

As shown in Chapter 2.2.2, the mode splitting Δn is inversely proportional to the birefringent fringe spacing $\Delta\lambda$, $\Delta n = (\lambda_p^2)/(\Delta\lambda L)$ (Eq. (16)). Thus one reason we do not observe the spatial mode interference fringes could be they are too far apart and outside of the pump spectrum we are using. This is possible because even though our spectrometer works over a broad spectrum, we are only looking for fringes that modulate the pump spectrum, which spans over 20 nm (10 nm full width at half maximum). Because we only observed 3 nm polarization mode fringes, it is possible that the splitting between the even and odd spatial modes are outside of the 20 nm pump spectrum. This would imply the splitting between the even and odd spatial modes is larger than the splitting between polarization modes. If we had a broadband source, we would have been able to test this possibility more thoroughly. Another possibility for not observing the spatial mode fringes is the coupling between the even and odd modes is too strong, and the large Δn_{eo} leads to interference fringes that are really tightly spaced that our spectrometer could not resolve. This situation is likely because we expected the structure of two touching waveguides to exhibit strong coupling.

4.3.2 Spatial mode splitting prediction using fabrication data for the 7 μm microcoupler

With the equipment we have, we only measured the polarization mode splittings of the 1 μm-diameter microcoupler, not the spatial mode splittings. To test that the microcoupler behaves as we predict, especially to confirm it does support the even and odd modes, we fabricated another microcoupler with larger diameter and weaker coupling between the modes.

The motivation for making the larger microcoupler follows the second hypothesis in the previous subsection, namely decreasing the coupling strength and thus increasing the fringe spacing. This should allow us to observe the fringes from the even and odd spatial modes, which we suspect are too strongly coupled previously, and predict the spatial mode splitting. The new microcoupler is 7.334 μm in diameter, with an effective length of 83.3 mm. We selected these design parameters based on the fabrication data for the 1 μm microcoupler. The reason we used the fabrication data for the 7 μm microcoupler as an example in Chapter 4.1 is because the fabrication data for the 1 μ cannot be resolved, likely because the detector response time was not fast enough, as seen in Fig. 17.

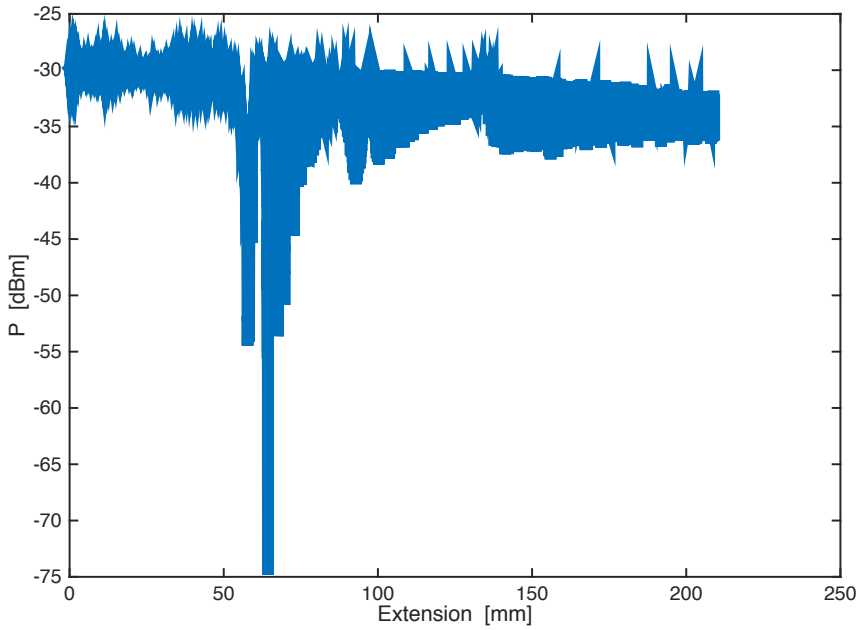

Figure 17: Real-time fabrication data from the automated LabVIEW program for the microcoupler 1 μm in diameter. The vertical axis is the power in one waveguide measured in decibels (dB), the horizontal axis is the extension of the tapered region, measured in millimeters (mm). Comparing with Fig. 12, where we can read the spacing between fringes, it is clear that we cannot resolve the power transfer fringes well for this dataset, as the fringes are oscillating much faster and too close together. This fabrication data is obtained in collaboration with Chams Baker.

Our estimate for the number of power transfer cycles in the 1 μm microcoupler is around 1000. This estimation is from Chams Baker, who fabricated

the microcouplers and has made similar structures with the same setup. For the new microcoupler, we aimed to reduce the number of power transfer cycles by a factor of 10. The 7 μm-diameter microcoupler has 103 power transfer cycles between the two cores which allowed us to get more reliable fabrication data with the same detection equipment. The power transfer data for this microcoupler is shown in Fig. 12, while Fig. 19 shows the theoretical calculations used to estimate the core diameter during fabrication. In Fig. 18 we zoom in on the fabrication data in Fig. 12 to find the coupling length from the power transfer fringes at the waist of the taper. The coupling length for the even and odd modes is defined as the distance between the two adjacent maxima (or minima) in the power transfer versus extension plot. From this fabrication data, we find a coupling length of $(157.7-156.6)\div 3 \approx 0.367$ mm. Using this coupling length prediction we can find a value for the even-odd spatial mode splitting, Δn_{eo}, as well as predict the spacing between the interference fringes of the two spatial modes due to this splitting. We can then measure the fringe spacing experimentally and compare the result with the prediction.

The calculation for finding the even-odd spatial mode splitting (Δn_{eo}) from the coupling length (L_c) is as follows. We start with the phase accumulation equation (Eq. (16)), also used to derive fiber birefringence, or polarization mode splittings

$$\phi = \frac{2\pi n}{\lambda} L, \tag{49}$$

which shows that phase is directly proportional to the index of refraction and the propagation length. It is also inversely proportional to the pump wavelength λ. For interference, the phase difference of one full fringe is equal to 2π. For our microcoupler, in order to get a full power transfer fringe from one core to the other we need a phase difference of π. Let the two cores each have index of refraction n_e and n_o, respectively. The propagation length needed to get a phase difference of π is equal to the coherence length, $L = L_c$:

$$\pi = \frac{2\pi(n_e - n_o)}{\lambda} L_c, \tag{50}$$

where $n_e - n_o = \Delta n_{eo}$.

Now we have a relationship between the mode splitting Δn_{eo} and the coupling length L_c,

$$\Delta n_{eo} = \frac{\lambda}{2L_c}. \tag{51}$$

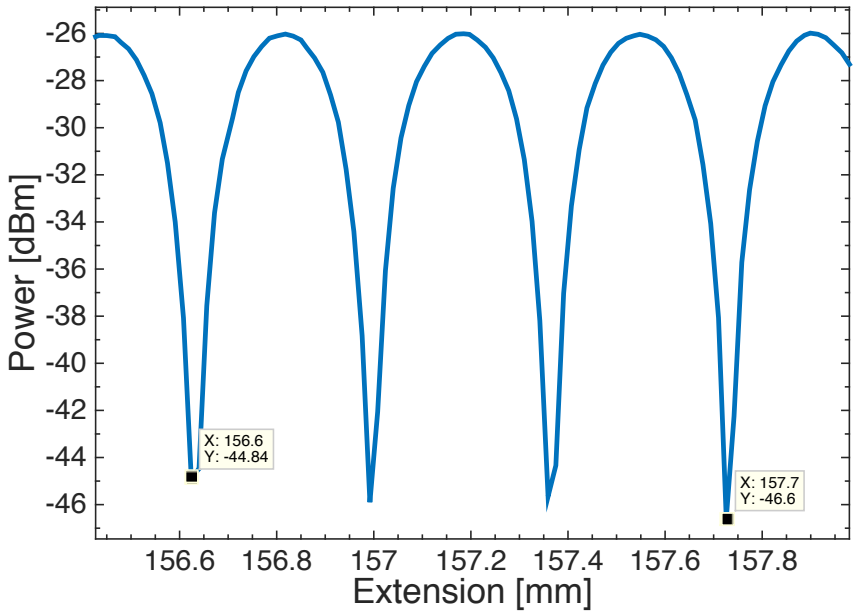

Figure 18: Power transfer between two cores during fabrication of the 7 μm microcoupler. This is the same data as Fig. 12, zooming in on the smallest core diameter of the taper. The vertical axis shows the power inside one of the two waveguides as the tapered region is stretched. The horizontal axis plots the extension of the tapered fiber. The coupling length between the even and odd modes is the separation between two adjacent power transfer peaks. For this microcoupler, we predict a coupling length of $(157.7\ mm - 156.6\ mm) \div 3 \approx 0.367\ mm$.

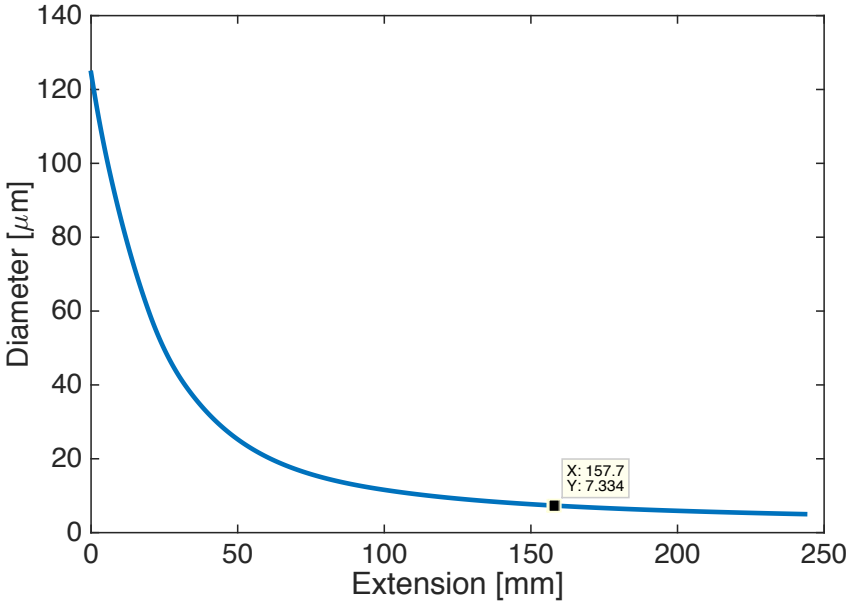

Figure 19: Theoretical calculation result used during the fabrication of the 7 μm microcoupler. This plot shows the calculated core diameter versus taper extension. An enlarged version of the minimum core diameter is shown on the right. Assuming constant diameter throughout the uniform interaction region, this plot predicts the minimum core diameter at the maximum taper extension length. The core diameter over the entire region decreases as the extension increases. The maximum extension length corresponds to the maximum extension of the taper during fabrication, shown in both Figs. 12 and 18. This value marks the point where the tapering process was stopped. At the maximum extension length of 157.7mm, the core diameter of each waveguide is predicted to be 7.334 μm.

We measured a coupling length of 0.367 mm from the fabrication data for the 7μm-diameter coupler in Fig. 18. Substituting this coupling length value into Eq. (51), we have

$$\begin{aligned} \Delta n_{eo} &= \frac{\lambda}{2L_c} \\ &= \frac{800 \text{ nm}}{2\times 0.367 \text{ mm}} \\ &= 1.0899 \times 10^{-3}. \end{aligned} \tag{52}$$

Using this difference in refractive indices between the even and odd modes, we expect a fringe spacing of

$$\begin{aligned} \Delta\lambda &= \frac{\lambda^2}{\Delta n_{xy} L} \\ &= \frac{800 \text{ nm}^2}{1.0899\times 10^{-3}\times 0.833 \text{ m}} \\ &= 7.05 \text{ nm}, \end{aligned} \tag{53}$$

where L is the effective length, or the length of the uniform interaction region, for the 7 μm-diameter microcoupler. It is predicted to be 83.3 mm for a maximum extension of 157.7 mm.

4.3.3 Spatial mode splitting measurement: 7 μm microcoupler

We are able to measure the fringe spacing caused by the spatial mode splitting for the 7 μm microcoupler, and compare the results with the prediction in Eq. (53). The measurement results for the spatial mode interference fringes are presented in Figs. 20 and 21. Fig. 20 shows the interference fringes between the even and odd modes, taken with the Ocean Optics spectrometer. Fig. 21 shows the same fringes with the intensity divided by the pump intensity, to correct for the shifting of the fringes caused by the pump spectrum. From these figures we see that after the correction for the pump spectrum, the spacing between two adjacent interference fringes due to the even and odd modes is 7.5 nm. This shows agreement with our predictions based on the fabrication data. This also tells us the structure of the 7 μm microcoupler is what we expect, in the sense that it does have even and odd mode splittings that can contribute to phasematching.

In summary, this section describes our attempts to obtain experimental data on the mode splittings of the microcoupler. We measure the fringe spacing resulting from interference between the two orthogonal polarizations (x, y) in the 1 μm-diameter microcoupler. This gives us one set of polarization mode splittings. The method used is similar to how we measure and

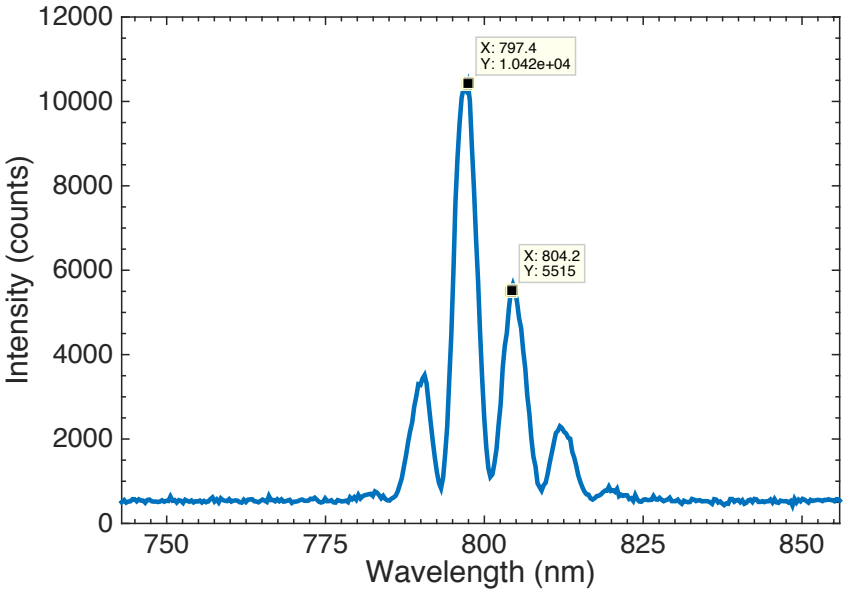

Figure 20: Experimental data of the interference fringes for the 7 μm-diameter microcoupler. In contrast to the birefringent fringes in Fig. 16, we observe these fringes regardless of pump polarization, which is evidence of the even and odd spatial modes present in this microcoupler. We measure a fringe spacing of 804.2 nm - 797.4 nm = 6.8 nm. This data is taken with input power 10 mW, using the Ocean Optics spectrometer.

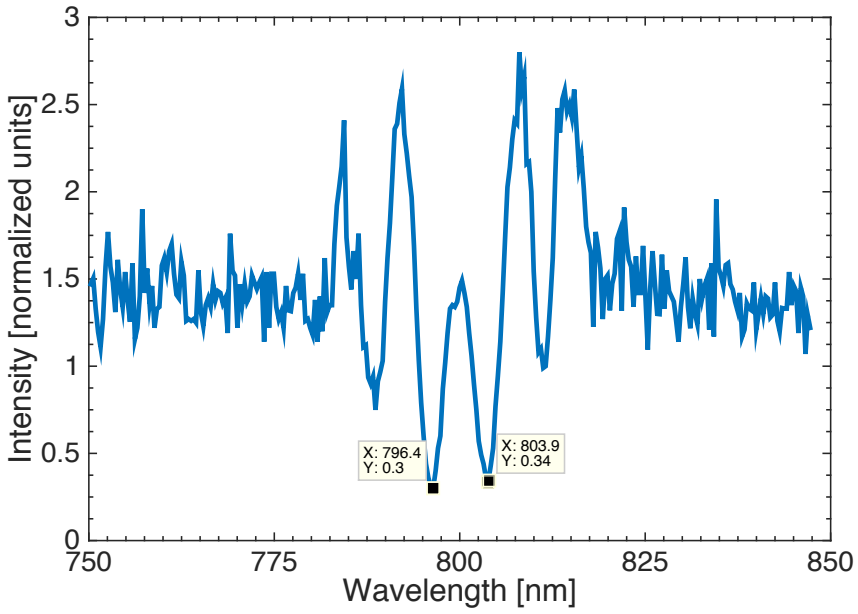

Figure 21: Experimental data of interference fringes for the 7 μm-diameter microcoupler, correcting for the pump spectrum. This is the same set of data as shown in Fig. 20, dividing by the pump spectrum at 10 mW. We estimate the interference fringes between the even and odd modes after correction to be 803.9 nm - 796.4 nm = 7.5 nm.

calculate birefringence for a PM fiber. We made a second microcoupler of larger core size because we wanted to observe the splitting between the even and odd spatial modes. We do not observe the spatial mode splittings in the 1 μm microcoupler, most likely due to the coupling being too strong between the spatial modes. Having a larger core diameter allows for weaker coupling. We use the fabrication data for the 7 μm-diameter microcoupler to predict the coupling length which relates to the splitting between the even and odd spatial modes. We then measure the interference fringes and show that the predicted fringe spacing agrees with our experimental results. The fact that we do not observe both the polarization and spatial mode splittings in the same microcoupler helps us improve the microcoupler design. More specifically, observing the polarization mode splittings in the 1 μm-diameter microcoupler, and the spatial mode splittings in the 7 μm-diameter microcoupler suggests we could make another microcoupler with a diameter that is in-between the two prototypes we tested.

4.4 Conclusion

In the first section of this Chapter, the design and fabrication procedure for the microcoupler have been described. We have also characterized some of the main features of interest of the microcoupler. We estimated the average input power required for SFWM photons generated in the microcoupler to be detected, for microcouplers of two different core diameter values (1 μm and 7 μm). We also measured the polarization mode splittings in a method similar to the birefringence measurement of a standard birefringent fiber. Both microcouplers tested were fabricated in the same setup with SM600 single-mode fibers. The fabrication process is monitored via power transfer between the two cores, using an 810nm diode laser as the input.

Unlike a standard optical fiber, the microcoupler structure does not have an effective length equal to its total length. This is because the length of the tapered region is limited in practice, and fibers need to be spliced to the input and output ends of the microcoupler after the tapering process. We do not expect SFWM to happen in these additional input and output fibers because they have much larger diameter and mode area compared to the tapered fiber. Dispersion of the pump pulse in the input fiber spliced to the microcoupler is the main concern. We try to reduce the effects of dispersion during the experiment by making the splice as short as possible, as well as making the pump bandwidth narrower with bandpass filters. The experiment is described in detail in the next chapter.

5 Photon-pair generation in microcoupler: experiment

Having theoretically modelled the microcoupler and experimentally characterized some of its properties (Chapters 3 and 4), in this chapter we focus on the main goal of the project: generating SFWM photon pairs in the microcoupler. This chapter describes each part of the experimental setup and analyzes the main results.

Once we detect the generated photons and optimize their detection efficiency, we need to confirm their single-photon nature. We perform a few tests to verify the signal we detect are indeed single photon pairs generated via SFWM, rather than noise from the laser or artifacts from the detection equipment. Examples of these tests include pump-power dependence of the generated photons, and coincidence counting using avalanche photodiodes (APDs) as detectors.

Having confirmed the generation of single photon pairs via SFWM, the next step is to study the polarization and spatial mode properties of these generated photon pairs, as well as how they relate to the pump photons. Obtaining this information would help us figure out which phasematching processes occurred in the microcoupler to generate these photon pairs. In addition, learning more about the polarization states of the generated photons will give us information on whether we can produce polarization-entangled photon pairs with this microcoupler. One method to determine photon polarization is called tomography. In this experiment we use single-photon polarization tomography as a first approach, although full reconstruction of the two-photon state using quantum state tomography is also an option.

Details of the experimental design are presented in the first section of this chapter. The second section explains the procedure taken to detect SFWM photon pairs. Chapter 5.4 highlights the main experimental results, as well as the analysis performed on the generated photon pairs. The single photon polarization tomography results are also included as part of the analysis. The final section concludes the chapter by highlighting what we learned from the experiment thus far. Suggestions for future work are given in Chapter 6.

5.1 Experimental design

The experiment took place in the femtosecond lab of the National Research Council (NRC), at 100 Sussex Drive, Ottawa, Canada. I started the setup at NRC in December 2015 with the help of Lambert Giner, based on a previous setup by Davor Curic. Throughout the duration of the experiment, Duncan England and Philip Bustard from NRC provided valuable help and suggestions. The experimental setup is described in sequence, from pump laser to detection of generated photons, split into four parts for convenience: 5.1.1: settings of the pump pulse, 5.1.2: coupling the pump into and out of the microcoupler, 5.2.1: filtering out residual pump for detection. The apparatus of the entire setup is shown in Fig. 22. The methodology for detecting photon pairs is presented in Chapter 5.3.

5.1.1 Pump pulse preparation

Our pump laser is a Spectra-Physics Tsunami Titanium:Sapphire laser. It has a center wavelength of 800 nm, pulse duration 100 fs, repetition rate 80 MHz, according to specifications. Its full width at half maximum is measured to be around 10 nm. It is a laser shared across setups, and the maximum power we can use on this setup is 400 mW.The first half-wave plate (HWP1) and polarizing beam splitter (PBS) shown on the left in Fig. 22 are used to reduce the power sent to the rest of the setup. Since the PBS only transmits one type of polarization, the half-wave plate can be rotated to control how much power is being allowed through the PBS. During our experiment, HWP1 is mostly fixed to allow 100 mW to the rest of the setup. A second half-wave plate (HWP2) reduces the power further, before sending the pump to a Glan polarizer (GP), which contains a PBS and also only transmits one polarization (horizontally polarized). The second HWP is what we use to control the input power for the microcoupler during most of the experiment. After the pump passes through the Glan polarizer, HWP3 selects the pump polarization we want to send to the microcoupler. This half-wave plate is the one we adjust to measure the birefringent splitting, and to test the pump-polarization dependence of the generated photons. A photograph of this part of the setup is shown in Fig. 23.

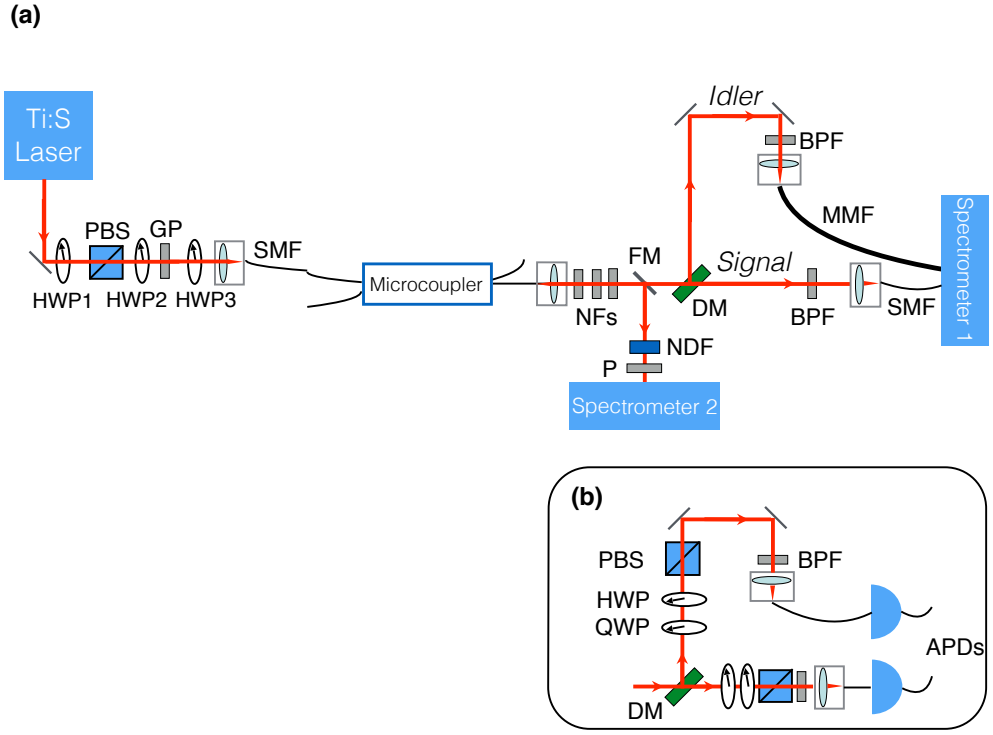

Figure 22: Schematic of the apparatus. HWP: half-wave plate; PBS: polarizing beam splitter; GP: Glan polarizer; SMF: single-mode fiber; NF: notch filter; FM: flip mirror; DM: dichroic mirror; NDF: neutral density filter; P: polarizer; BPF: band-pass filter; MMF: multi-mode fiber; QWP: quarter-wave plate; APD: avalanche photodiode. (a) The general setup used to look for generated SFWM photon pairs. The apparatus can been separated into three main parts: preparing the pump photons, coupling into the microcoupler, filtering out the pump, and detection. Two detection instruments are shown: Spectrometer 1 is an industry-grade spectrometer connected to an EMCCD camera. It is fiber coupled and either the SMF or the MMF can be connected to the spectrometer. It has three gratings and we use the one with the smallest density (600 g/mm) to get the largest detection range of 120 nm when looking for peaks. The spectrometer program is also able to perform background subtraction and averaging of signals over a selected number of frames. Spectrometer 2 is an Ocean Optics portable spectrometer connected to the computer control via USB. We keep it in the setup behind a flip mirror to monitor the pump spectrum as well as make measurements on the mode splittings. (b) Detection setup for single-photon polarization tomography. The apparatus before the dichroic mirror (DM) remains the same as in (a). After the photons exit the dichroic mirror and are separated by wavelength, they go through additional optics in each arm: a polarizing beam splitter, a half-wave plate and a quarter-wave plate. This version of the apparatus will be examined more later in this chapter.

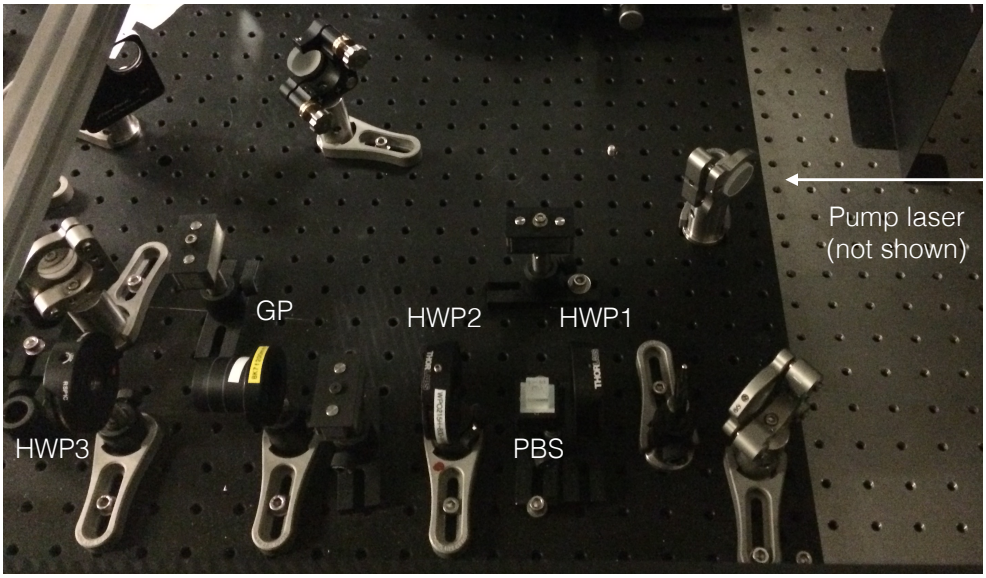

Figure 23: A photograph of the first part of the apparatus, from the shared pump beam to the half-wave plate (HWP) before the microcoupler stage. The purpose of these optics is to control the input power and polarization of the pump. In this picture the laser beam travels from right to left. HWP: half-wave plate; PBS: polarizing beam splitter; GP: Glan polarizer. The pump beam comes from a shared Ti:S laser and has a maximum power of 400mW.

5.1.2 In-coupling considerations

The next part of the apparatus serves to couple the beam into the microcoupler. As mentioned earlier, the microcoupler has four ports, each one spliced with half of a commercial Thorlabs SMF630 fiber. This is the same kind of fiber the microcoupler is made of (SM600). We tested the transmission of the microcoupler before and after the splicing process and found the loss due to splicing negligible. Since all four ports are fiber-spliced, it is easy to couple into and out of the microcoupler by connecting the spliced ports onto a fiber holder on a tri-axis stage. We can then optimize the coupling using the stage and two mirrors in the path of the beam before the stage. As mentioned in Chapter 4.2 when talking about pump pulse dispersion, we introduce a short fiber in addition to the fiber spliced to the microcoupler.

The purpose of adding this fiber is explained in Chapter 5.1.3. This short fiber was fabricated by cutting a commercial Thorlabs SMF630 fiber into three parts, removing the middle part and keeping the connectors on both ends. We then splice the bare fiber ends of the two segments together, in order to get the shortest fiber we can make that has one connector on each end. It is 15 cm long, the minimum length required by the splicer we use. Instead of mounting the fiber-spliced microcoupler input port directly onto the tri-axis stage, we mount one end of the short fiber onto the stage. After optimizing the coupling into the short fiber, we attach the short fiber to the microcoupler by attaching their connectorized ends with an FC-FC fiber-to-fiber coupling adaptor, also called a fiber mating sleeve.

5.1.3 Purpose of additional short fiber

Despite increasing the effect of pulse dispersion, we decide to add the short fiber both to make coupling into the microcoupler easier, and to protect the microcoupler when using high power.

We would like to optimize the coupling efficiency of the setup before it enters the microcoupler, in order to isolate effects due to the microcoupler itself. When we put the microcoupler into the setup for the first time, we have no control over the power transfer from one core to another inside the microcoupler. Because we are only using one input and one output among the four available ports of the microcoupler, at times it could seem like the beam is misaligned because the output power drops, when in fact the power is transferred to the other core at that moment. In other words, optimizing the efficiency when coupling directly into the microcoupler is difficult due to the power transfer happening inside the microcoupler. In addition, when checking the coupling efficiency daily, we would prefer to keep the microcoupler and all its fibers ports fixed, both to avoid breaking them and to prevent possible effects on polarization from moving the fibers. To make the coupling process easier, we mount the short fiber on the tri-axis stage and optimize the coupling of the pump into the short fiber first, instead of putting the microcoupler input fiber directly on the stage.

When sending in higher power to the microcoupler, the input surface of the fiber, which is the interface between air and glass, will get burnt. After adding the short fiber before the microcoupler, the interface at the microcoupler input port is fiber-to-fiber, and would be less likely to burn. Also it would be easier to replace the short fiber than to fabricate a new microcou-

pler.

5.2 Transmission efficiency

We send in 5 mW of input power to the microcoupler, and measure the output after the short fiber with a power meter that has a threaded mount for a fiber adapter plate. We measure one microcoupler output port at-a-time. When calculating the microcoupler coupling efficiency, we combine intensity readings at both outputs. This is because the pump sent in from one input port transfers back-and-forth between the two cores, so the input power is shared between the two outputs. As mentioned in Chapter 4.1.2, the transmission ratio between the two output ports is random for the microcouplers fabricated so far. We can engineer this transmission ratio between two cores. For the 1 μm microcoupler, the transmission efficiency is between 56 and 65 %. The short fiber alone has a daily coupling efficiency above 80 %. It is worth mentioning that when taking data, whether using the spectrometer or the APDs for detection, we only have one microcoupler output connected to the rest of the setup. We only use one microcoupler input and one output for the extent of this project. It would be interesting to measure both outputs simultaneously in the future.

5.2.1 Filtering setup before detection

The main purpose of the next part of the setup is to filter out the residual pump beam before it reaches the detectors. After photon pairs are generated via SFWM inside the microcoupler, they exit the coupler along with the remaining pump beam via the output fiber. One of the two output fibers is mounted on an identical stage as the input fiber stage, with the same collimating lens. Now that the pump beam and generated photons are out of the microcoupler and in free space, we can filter them by wavelength. In order to observe the SFWM photons which are much weaker than the pump and the Raman noise, we put a set of notch filters at the output of the microcoupler to block the pump. We use two Semrock NF03-808E-25 notch filters with optical density (OD) greater than 6 at its center wavelength of 808 nm. The notch bandwidth is 41 nm according to specifications. We also use one 830 nm notch filter from Edmund Optics, which has a bandwidth of 42 nm. It has OD greater than 4 at the center wavelength of 830 nm.

After the notch filters there is a flip mirror (FM) followed by a dichroic

mirror (DM), as shown in Fig. 22. When the flip mirror in front of the dichroic mirror is flipped up, it blocks the dichroic mirror and redirects the beam to a portable Ocean Optics spectrometer (labelled at Spectrometer 2 in Fig. 22). This is the spectrometer we use to take the mode splitting measurement data shown in Chapter 4. We also use it to check the pump spectrum, especially when increasing the input power. When checking the pump spectrum, we need to remove the notch filters and put neutral density filters (NDFs) in front of the spectrometer to protect it. The beam exiting the microcoupler into free space is sent to the neutral density filters and the spectrometer, without being coupled into another fiber. This is because we noticed the spectrometer fiber affecting our measurements by introducing its own interference fringes. The purpose of the polarizer in front of Spectrometer 2 is to mix the two orthogonal polarization modes when measuring the interference fringes for the mode splitting calculation in Chapter 4.3.

5.2.2 Separating the signal and idler arms

When the flip mirror is flipped down, the beam goes straight to the dichroic mirror, which separates the light according to wavelength. The dichroic mirror is acting as a shortpass filter in the sense that the shorter wavelength gets transmitted, and the longer one reflected. More specifically, we used a DMSP805 from Thorlabs which transmits light with wavelength below the cutoff of 805 nm, and reflects light above the cutoff wavelength. This dichroic mirror as well as the tri-axis stages are remnants of a former setup built for photon-pair generation in a birefringent fiber. The reason for splitting the photons at 805 nm is that both the signal and idler arms can be aligned with the 800 nm pump which is both transmitted and reflected. However, it might be preferable to use a shortpass filter with a cutoff wavelength at 700 nm instead, so that all of the pump and the Raman noise are reflected. We built two setups to repeat the birefringent fiber experiment, one with the 805 nm dichroic mirror, the other with a 700 nm shortpass filter, in two different labs. We took this step before testing the microcoupler to ensure the detection setup worked properly, and we could reproduce the results with the 20cm birefringent fiber making photons at 680 nm and 980 nm.

After the dichroic mirror, the beam is split into what we call the signal arm ($\lambda < 805$ nm) and the idler arm ($\lambda > 805$ nm). The signal and idler arms have one tri-axis stage each, with a fiber holder and a collimating lens mounted on top. The signal arm is coupled into a 3 m shielded single-mode fiber (SMF) with a center wavelength of 630 nm. The idler arm is coupled

into a 3 m shielded multimode fiber (MMF). These two fibers can either be connected to the avalanche photodetectors (APDs) and the coincidence counting logic box, or through fiber-to-fiber adapters to a 5 m shielded SMF and a 5 m shielded MMF, respectively. These two longer fibers extend across the room over the setup for a different experiment to reach the spectrometer with an EMCCD camera (Spectrometer 1). The fibers are shielded inside a metal tube and another black plastic tube. Shielded fibers are used to block out room lights and reduce background noise during detection. Because the experiments are performed with a shared pump laser in a lab with multiple experimental setups, the room lights are kept on all the time, unlike most labs using APDs. The methods used for detection of the generated photon pairs are presented in the following section.

5.3 Methodology for detection

An overview of the experimental procedure for detecting the generated SFWM photon pairs is presented in this section. We tried different methods for detection because the intensities of the generated photon pairs from the microcoupler were weaker than we expected. Initially we expected to see the signal and idler photons on an Optical Spectrum Analyzer (OSA) such as the Yokogawa AQ6370C OSA used to measure the birefringent mode splittings in Chaper 4.3. This OSA has a detection range from 600 to 1700 nm, and resolution of 0.02 nm. Based on previous work on detecting SFWM photons in a 20 cm-long birefringent fiber, we were expecting to detect the SFWM photons with input power below 15 mW [3].

We decided to move the experiment to NRC mainly because we needed a spectrometer with an EMCCD (electron multiplying charge-coupled device) camera. The EMCCD is useful because it is more sensitive to light than a CCD camera. When looking for the generated peaks, we also needed to be able to look over a broad range of wavelengths to check for multiple sets of peaks, as well as to ensure the pump and Raman are filtered out. Thus we could not start with the avalanche photodiodes (APDs), even though they are sensitive to single photons, because the signal from the photon pairs would not be distinguishable from the Raman. The spectrometer we used is the Acton SP2300, manufactured by Princeton Instruments. It has a resolution of 0.14 nm for the 1200 g/mm grating, and a detection range from 0 to 1400 nm, according to specifications. The EMCCD camera for the spectrometer is the ProEM 1600. Together they are labelled as Spectrometer 1 in the apparatus in Fig. 22. The spectrometer software also provides helpful features such as averaging the signal over many frames as well as background

subtraction. After filtering out the pump and Raman on Spectrometer 1 and finding SFWM peaks, we use the APDs to verify the signals are indeed from correlated photon pairs, as well as optimize on the alignment for the selected peaks.

5.3.1 Spectrometer settings

The EMCCD camera and Spectrometer 1 are both connected to the same LightField software, where we select the settings for each scan. Some key parameters to vary include the central wavelength for the camera, the integration time, the number of frames to average over, and whether or not to apply background subtraction. Even though there is no threshold for SFWM to occur, we still need a certain amount of power for the generated photon pairs to be distinguished from the noise of our equipment. The SFWM photons are much weaker than the pump that leaks through the filters, so we average the data over many frames while applying background subtraction on each frame. The dataset for the background is taken by first blocking the incoming pump beam at the start of this setup, using identical settings as the scan for photons. The software takes the average by summing up the signal for the number of desired frames, and then dividing by the number of frames at the final frame. The data for SFWM photons shown in the next section are taken after background subtraction, at 20 s of exposure time for each frame, averaging over 50 frames. The spectrometer has 3 gratings on a rotatable turret, and we choose the 600 g/mm grating which allows for the widest detection range of 120 nm. The resolution for this grating is 0.28 nm. Even though the spectrometer input is fiber coupled, we are losing some photons at the slit. We also tried focusing the light from the fiber directly onto the slit to get a better quality image on the camera.

As mentioned in the previous section, we can connect either the single-mode fiber (SMF) or the multimode fiber (MMF) to the spectrometer input, to look for SFWM photons in the signal or idler arm, respectively. Based on predictions for the birefringent fiber of similar core size and length, we expect the idler photon to be at wavelengths around 1 μm, and the idler around 600 nm. Because the detection efficiency is only around 10 % above 1 μm, and also because the Raman noise is easily visible in the idler arm from around 850 nm, we start by looking for the signal photon in the other arm. After optimizing the alignment in the signal arm SMF by back injecting a 633 nm red diode laser, we connect the SMF to the spectrometer.

We can also tilt the filters to block the pump leak. This step is necessary

when we increase the input power by a large amount which causes the pump spectrum to broaden and leak outside of the range of the notch filters already in place. To filter out the additional leak, we use the spectrometer without averaging. We adjust the filter angle while monitoring the spectrum on the spectrometer in real time.

5.3.2 Scanning procedure and artificial peaks

For each set of parameter values, a background scan and an actual scan are needed. For an integration time of 20 s per frame, averaging over 100 frames, a scan takes over 30 minutes. Starting from 650 nm as the central wavelength for the camera, we decrease the central wavelength by 50 nm intervals until 450 nm, then increase either the input power or the integration time, take new background scans, and move up to a larger central wavelength. The wavelength range is 120 nm so the scans taken have regions that overlap, which can help us distinguish artificial peaks due to background subtraction or the spectrometer itself. This is because if the peak is from real SFWM photons, its location would not move when the camera moves to a different central wavelength. We also check for artificial peaks by switching to a different grating to see if any features are persistent.

For instance, for the 7 μm microcoupler, when the pump is not completely filtered out at higher power, we notice small peaks on the lower wavelength side of the notch filter bandwidth (775 nm). These smaller peaks only show up after averaging and background subtraction. Meanwhile, we get 11 equally-spaced peaks in the total wavelength range we are sweeping (390 nm to 710 nm). They shift by about 10 nm when the central wavelength is changed by 50 nm. More importantly, these peaks disappear when a different spectrometer grating is used. We figured out that these peaks are artificial and likely due to a ghosting effect. The pump leaking through the notch filters can scatter onto other parts of the grating inside the spectrometer. We try to eliminate these artificial peaks that can overshadow our SFWM signal peaks by filtering out the pump completely even after averaging and background subtraction. We also tilt the filters each time the input power increases by more than 50 mW for the 7 μm microcoupler. The additional pump leakage is not a problem for the 1 μm microcoupler because we operated at low power, and only see significant pump broadening due to self-phase modulation (SPM) above 50 mW.

After we find a signal peak that is not an artifact due to the spectrome-

ter or background subtraction, we want to check its power and polarization dependence. The generated SFWM photons increase quadratically with the increase in pump power, while the Raman noise increases linearly with pump power, as shown in Eq. (5). Seeing this quadratic dependence is a piece of evidence that the photons detected are generated by SFWM. An example of the quadratic dependence on pump power of a signal photon we detected is shown in Fig. 24. In this plot, the intensity of the detected SFWM peak is quadratic with the input power. It is not a pure quadratic fit likely due to the Raman background, which increases linearly with input power.

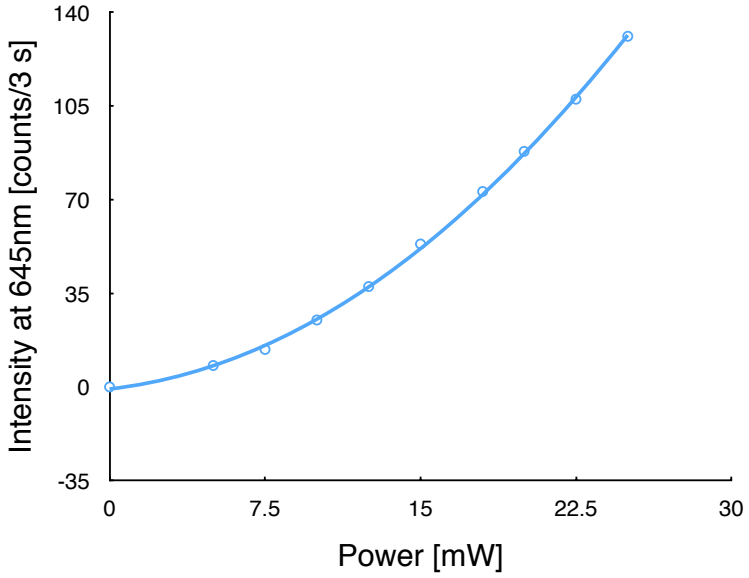

Figure 24: Pump power dependence data of a detected signal photon peak at 645 nm, taken with background subtraction and an exposure time of 3000 ms per frame, averaging over 100 frames. The vertical axis shows the intensity of the peak (I) in counts per 3 seconds, the horizontal axis shows the average power measured at the microcoupler before each scan in mW (P). After fitting the data to a second order polynomial, we get a quadratic fit with the equation is $I = 0.1769P^2 + 0.8665P - 0.769$. *In this plot, the intensity of the detected SFWM peak has a quadratic relationship with the input power. This is evidence of the observed 645 nm peak being generated via SFWM. It is not a pure quadratic fit likely due to the Raman background, which increases linearly with input power, giving us the linear term in the equation.*

We also want to study the pump polarization dependence of the signal peak in order to find out which phasematching process generated this signal photon, and where in wavelength its partner is. One direct method of seeing how the pump polarization changes the generated photons is to change the pump polarization before the microcoupler with HWP3, while monitoring the generated peak on the spectrometer. In practice we took scans for different pump polarization angles because each scan involved averaging over many frames as well as background subtraction. We also use single photon polarization tomography to learn more about the polarization properties of the signal and idler photons. This analysis for the polarization of the generated photons is presented in the next section.

5.3.3 Checking for photon pairs using APDs

In addition to the dependence on pump power and pump polarization, we also need information on whether the generated photons are really SFWM pairs. To test that we use our third mechanism for detection: coincidence counting with avalanche photodiodes (APDs) as detectors. The APDs we use are of the SPCM-AQRH model, fabricated by Excelitas. These silicon avalanche photodiodes detect single photons over the wavelength range of 400 nm to 1060 nm. The peak photon detection efficiency is over 70% at 700 nm over a 180 m diameter circular active area. The hardware is interfaced with two LabVIEW programs, one controls the coincidence counting logic and shows real-time single photon counts; the other creates a histogram of coincidence counts versus time delay between the two channels. When the APDs on both the signal and idler arms record the arrival of a photon and click simultaneously, it is marked as a coincidence event.

An example of a histogram is shown in Fig. 25. This was taken for a photon pair with the signal at 645 nm and idler at 1053 nm, with input power 7.5 mW and accumulation time of 10 s. The vertical axis shows the coincidence counts in 10 seconds according to the APDs, and the horizontal axis represents the time delay between the signal and idler arms. The highest peak is due to the generated photon pair, because the probability for simultaneously detecting the two is correlated. This is the strongest evidence that we have SFWM photons. The peak value for this scan is 130 counts per 10 s.

We find the value of the accidentals from the lower peaks. The accidentals are the accidental coincidence counts in our coincidence window due to

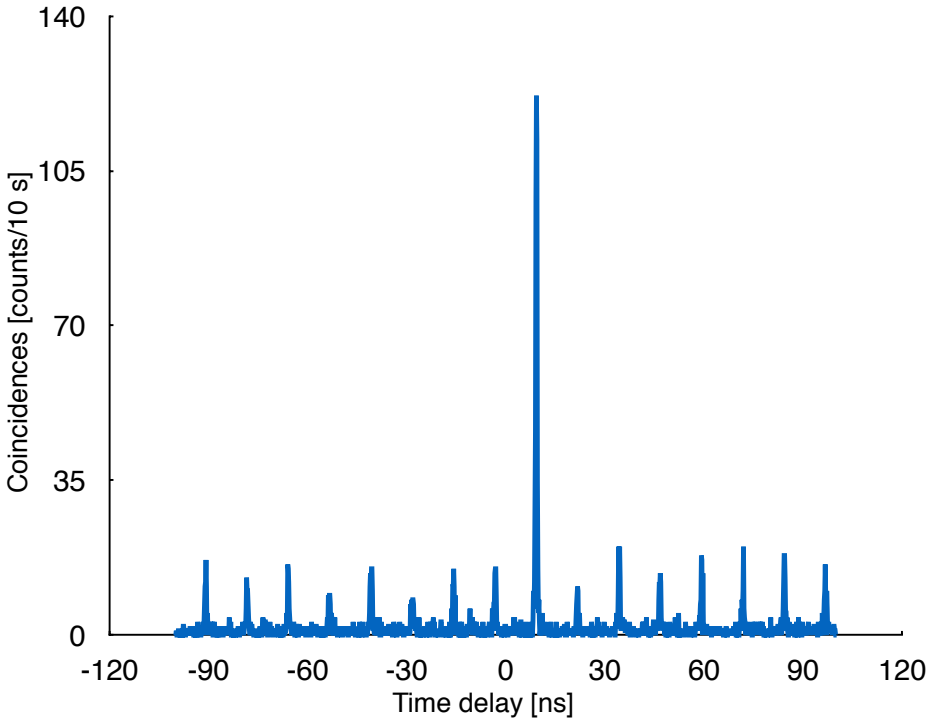

Figure 25: A sample histogram showing coincidences between the signal and idler photons generated via SFWM in a 1 μm-diameter microcoupler. This was taken for a photon pair with the signal at 645 nm and idler at 1053 nm, with an input power of 7.5 mW and an accumulation time of 10 s. The vertical axis shows the coincidence counts during 10 s according to the APDs, and the horizontal axis shows the time delay between the signal and idler arms in nanoseconds. The highest peak represents the correlated SFWM photon pair, the smaller peaks are accidentals most likely due to Raman noise. The highest peak for this scan is 130 counts per 10 s of run time, and the accidentals average to 20 counts per 10 s. The coincidence-to-accidental ratio is 5.5. The spacing between neighbouring peaks is 12.5 ns, resulting from our pulsed pump laser with a repetition rate of 80 MHz. The highest peak is shifted from a time delay of 0 due to optical and electronic delays in the system.

uncorrelated photons. They are part of the background. These counts can be due to Raman noise in the idler arm arriving at the detectors at the same time as photons of the signal arm. The accidentals are below 20 counts per 10 s on average. The accidental counts are lower because these photons are uncorrelated. That is, they are not produced in pairs. If we did not generate SFWM photon pairs which are correlated, the histogram would only have evenly-spaced accidental peaks of the same average height. The spacing between neighbouring peaks is 12.5 ns, which corresponds to the repetition rate of the pulsed pump laser we are using. The coincidence-to-accidental ratio is $(130-20)/20 = 5.5$. This is not very high for a couple of reasons. We are only using one output of the microcoupler so at least half of the photons are lost. The efficiency of the APDs also drop off at wavelengths larger than 1 μm, where we expect the idler photon for this microcoupler.

5.3.4 Filtering out pump and Raman before APDs

When using the APDs for detection, we need to be especially careful about filtering out both the pump and the Raman. This is not only because the APDs are sensitive at the single-photon level, but also because they detect a broad spectrum of light and cannot look at a small range of wavelengths at a time as the spectrometer and camera. After finding the signal photons on the spectrometer, we put an additional short pass filter at 700 nm in the signal arm to reflect wavelengths above 700 nm, thus blocking any pump leak below 800 nm. This is a Thorlabs FESH0700 filter, with OD greater than 5 for wavelengths longer than the 700 nm cutoff. We also put a Thorlabs FELH0900 filter in the idler arm. This is a long pass filter with a cutoff at 900 nm, with OD greater than 5 below 900 nm, blocking wavelengths below the cutoff. Even though we were not successful in seeing the idler peak on the spectrometer due to the low detection efficiency at that wavelength, we can calculate the idler wavelength given the signal wavelength observed, via energy conservation. This helps us decide what filters to use for coincidence counting with the APDs, since we want to optimize the transmission of the generated photon pairs while blocking as much Raman as possible on the idler arm. Once we have coincidence readings on the program integrated with the APDs, we can optimize the coupling as well as tilt the filters based on the coincidence counts in real-time. The results and analysis, including the single-photon polarization tomography, are presented in the next section.

5.4 Analysis of generated SFWM photons

In this section we present results of photon-pair generation via SFWM in the 1 μm-diameter microcoupler. After observing the peaks on the spectrometer, we perform single-photon polarization tomography to get more information on the polarization states of the signal and idler. We detected two peaks in the signal arm. We were able to calculate the polarization overlap between these two photons using the single-photon polarization tomography data. Unfortunately, we did not have enough time to optimize the signal on the APDs for these two peaks at the time of writing. The single-photon tomography data was taken on Spectrometer 1 with the EMCCD camera. Ideally we would like to repeat the same set of measurements using the coincidence counts on the APDs as the signal.

5.4.1 Detected SFWM photons

Using the detection methods described in Chapter 5.3, we were able to detect two peaks on the spectrometer with the EMCCD camera (Spectrometer 1) on the signal arm. The two peaks detected are shown in Fig. 26. For these scans we used an input power of 20 mW, averaging over 50 frames with an exposure time of 20 s per frame, with background subtraction and at 50 times the gain on the camera. If we had more time it would be better to repeat the scan with longer integration time and more averaging. The two peaks remain in place at 648 nm and 660 nm when we change the spectrometer grating and the center wavelength for the camera, so they are unlikely to be artifacts of the spectrometer itself.

5.4.2 Pump-polarization dependence

After confirming they are not artifacts from the spectrometer, we observed the change in the magnitude of the peaks while changing the pump polarization entering the microcoupler. We do this by rotating the half-wave plate before the microcoupler (HWP3 in Fig. 22), and taking a background-subtracted scan for each pump polarization angle. We compared the pump polarization dependence of the two signal peaks, shown in Fig. 27. This polarization dependence analysis was performed by Lambert Giner. We see both peaks can be fitted to a sinusoidal function, and peak 1 has a slightly better agreement. The fact that the maxima of the two series are apart by about 48 degrees suggests the pump photons generating the two signal photons are likely off by 45 degrees in polarization.

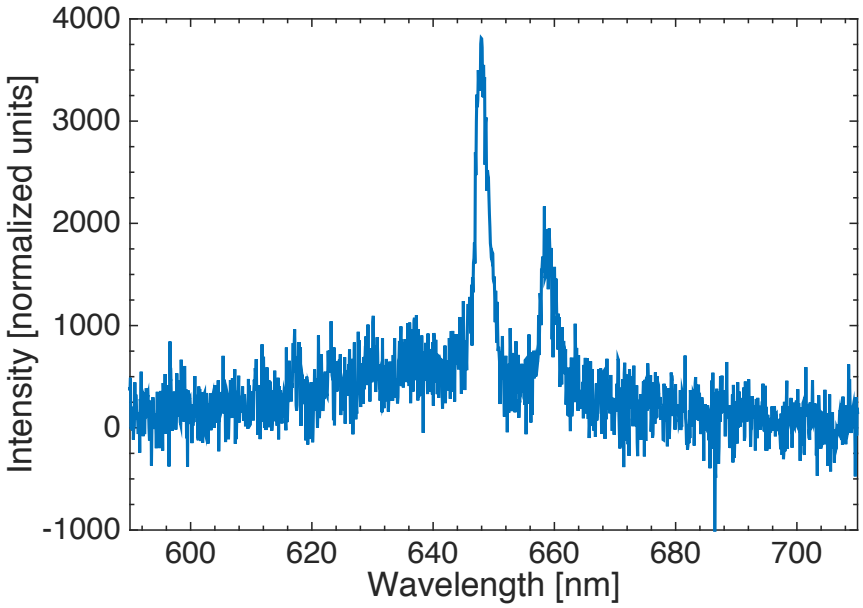

Figure 26: Experimental data of two peaks detected on the signal arm of the experimental setup. The data was taken with Spectrometer 1 and the EMCCD camera, using the 600 g/mm grating which leads to a detection range of 120 nm. The power at the microcoupler input was 20 mW, averaging over 50 frames with an exposure time of 20 s on each frame, subtracting the background. The first peak is at 648 nm and the second one at 660 nm. This dataset has been processed by taking a moving average of every five data points.

One possibility is one signal photon is created by two x photons or two y photons, while the other is created by two pump photons that are orthogonal in polarization, with a phasematching equation such as $x + y \rightarrow x + y$. However, we do not find any predictions at signal wavelengths close to the observed wavelengths for the second case of orthogonal pump photons. It is also worth noting that in Fig. 27, the minima of the two series, which show the pump polarization angle that gave the lowest signal peak intensity, are still far from zero counts. This is especially evident for Peak 2 where the minimum is at an intensity more than half of the maximum. Since the data is already taken with background subtraction, another possibility is we have another underlying phasematching process that is occurring simultaneously with the observed two processes. An additional issue is the fiber at the microcoupler input can rotate the pump polarization before the pump pulse reaches the uniform tapered region. This would also affect our pump polarization dependence data, since the polarization angles we use to find the relationship between the pump photons of each of the two processes may not be equal to the actual angles inside the microcoupler.

Even though the scans are time-consuming, taking more scans at smaller polarization increments is also an option. The next step would be to confirm this dependence on the APDs where we can detect both the signal and the idler photons simultaneously, whereas we can only plug in one fiber to the spectrometer.

5.4.3 Single-photon polarization tomography: experiment

Unlike the method of full quantum state tomography, which reconstructs the two-photon state from 16 measurements, single-photon tomography does not give us all the information about the two-photon state. We also assume the two photons are not correlated. However, single-photon tomography requires fewer measurements, and yet still offers information on whether the signal and idler have the same polarization. It allows us to compare the signal and idler polarizations with the pump polarization. This will help us eliminate some options in determining which phasematching process created the photon pairs we observed.

A schematic for the modifications to the apparatus in order to perform single-photon tomography is shown in Fig. 28. The wave plate settings for performing single-photon tomography is shown in Table 2. These settings are first applied to the idler arm, while the signal arm is held constant, with only a HWP and PBS before the detector fiber. The wave plates are changed

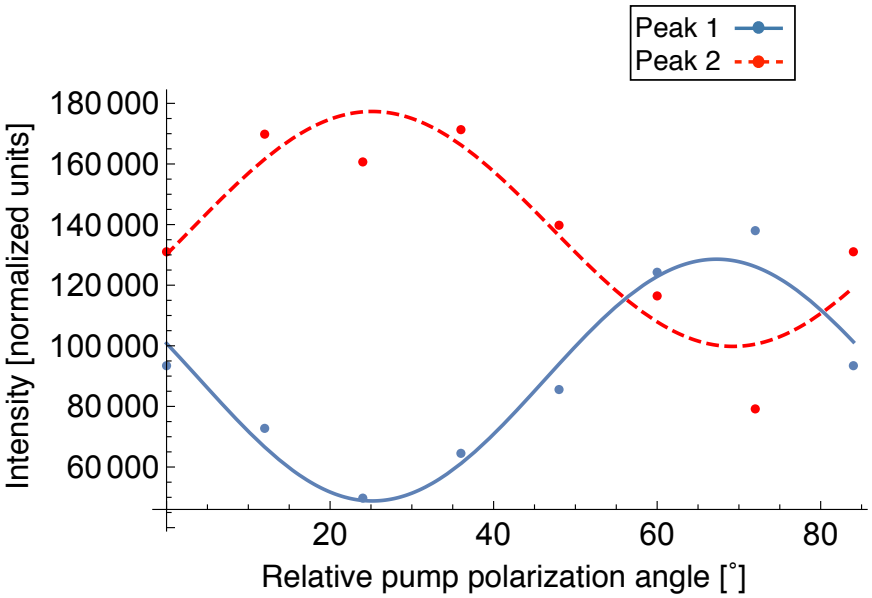

Figure 27: Plot showing the pump polarization dependence of the detected peaks. Peak 1 is the 648 nm peak, and Peak 2 is at 660 nm. The vertical axis plots the normalized intensity of each peak on the spectrometer, and the horizontal axis plots the relative pump polarization angle, shifted to start from 0 degrees. The data was taken at 12-degree polarization increments. Both data sets are fit to a cosine function. The pump polarization angle that leads to the maximum intensity for both peaks are out-of-phase by 48 degrees, which means pump photons of different polarization states led to the two signal peaks.

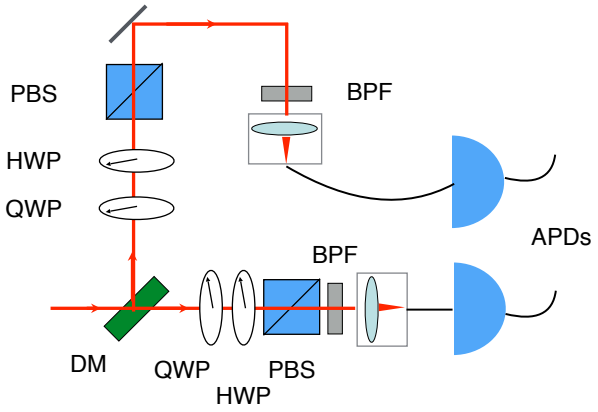

Figure 28: Schematic of the apparatus after the microcoupler output, modified from Fig. 22 for tomography. QWP: quarter-wave plate; HWP: half-wave plate; PBS: polarizing beam splitter; DM: dichroic mirror; BPF: band-pass filter; APD: avalanche photodiode. The apparatus before the dichroic mirror (DM) remains the same as in (a). After the photons exit the dichroic mirror and are separated by wavelength, they go through additional optics in each arm: a polarizing beam splitter, a half-wave plate and a quarter-wave plate.

	QWP (°)	HWP (°)
R	45	0
L	-45	0
H	-	0
V	-	45
D	-	22.5
A	-	-22.5

Table 2: This table shows the wave plate settings for single-photon polarization tomography. QWP: quarter-wave plate; HWP: half-wave plate. The six projected polarization states are: right-circular (R), left-circular (L), horizontal (H), vertical (V), diagonal (D), and anti-diagonal (A). The QWP is only needed for the first two circularly-polarized cases. It is removed before projecting the four remaining linearly-polarized states. This is because from past experience within the research group we know the QWP will add random rotations to the transmitted linear polarization, affecting results. These settings are first applied to the signal arm, the same setting is then repeated for the idler arm.

in this order because we want to minimize effects of the QWP on the linear

polarization measurements. More specifically, we remove the QWP from the setup once we finish projecting the left-circularly-polarized state L. After one set of single-photon tomography data is taken for the signal arm, the HWP is rotated back to when it gives maximum transmission (H or V), before we repeat the process on the idler arm.

During the actual experiment, we performed an overlap analysis for each of the two signal peaks instead. This is mainly due to limitations in time. Since we observed the two signal peaks on the signal arm, we wanted to check the polarization of these two peaks before moving to the idler arm, where the detection efficiency for the predicted photons is much lower (around 10 % for 1 μm wavelength). Also with the current apparatus we do not have a good method for isolating the two idler peaks for the APDs. The overlap analysis on the two signal peaks shown in the following section will still help us figure out which phasematching processes are responsible for these signal photons.

5.4.4 Single-photon polarization tomography: overlap analysis

We obtain one dataset of the six projected polarization states shown in Table 2 for each of the two signal photons. To analyze the polarization of the two signal peaks without fully reconstructing the photon states, we make use of an overlap parameter. This polarization overlap is essentially a tool to measure how different the two polarization states are. When the Stokes vectors representing the polarization of the two states are aligned, the overlap is equal to 1. When the two vectors are anti-aligned, the overlap is equal to 0.

To calculate this overlap, we first need to define the Stokes parameters using the outcome of the six projective measurements. Each of the Stokes parameters correspond to two projective measurements:

$$\begin{aligned} S_0 &= P_H + P_V \\ S_1 &= P_H - P_V \\ S_2 &= P_D - P_A \\ S_3 &= P_R - P_L, \end{aligned} \tag{54}$$

where P_H is the probability of measuring the photon in state H, or horizontally polarized. We calculate this probability as $P_H = \frac{R_H}{R_H + R_V}$, where R_α is the rate of generated photons measured for polarization state α. This holds because the polarization states H and V form a complete basis. When using experimental data of the projective measurements, we substitute the intensity of the measured peaks at each projected polarization for the generation

rate R, $R_V \propto I_V$.

The Stokes vector is

$$\vec{S} = \begin{pmatrix} S_0 \\ S_1 \\ S_2 \\ S_3 \end{pmatrix}. \tag{55}$$

We define the overlap parameter as

$$(1 + \vec{S}_{peak1} \cdot \vec{S}_{peak2})/2, \tag{56}$$

where $\vec{S}_{peak1}$ and $\vec{S}_{peak2}$ are the normalized Stokes vectors for the two signal peaks, respectively.

For this analysis we used data taken on Spectrometer 1 with the EMCCD camera. The scans were taken averaging over 25 frames with 15 seconds of exposure time per frame, at 100 times the gain and subtracting the background. The pump polarization was set to maximize the first peak (648 nm) on the spectrometer. We perform a moving average over 11 points to reduce the noise in the spectrometer data, and integrate over each peak to find the intensity of the two peaks at each of the six projected polarizations. After calculating the Stokes parameters defined in Eq. (54), we normalize the Stokes vectors using

$$\vec{S}_{peak\alpha} = \vec{S}_{p\alpha} / \sqrt{{S_{p\alpha 1}}^2 + {S_{p\alpha 2}}^2 + {S_{p\alpha 3}}^2}, \tag{57}$$

where α can be peak 1 or 2. The Stokes parameters for the two peaks are given in Table 3.

	S_1	S_2	S_3
Peak 1 at 648 nm	0.5042	-0.2122	-0.4071
Peak 2 at 660 nm	0.4614	0.1009	-0.4747

Table 3: Table showing the values of the Stokes parameters for the two detected photons. Peak 1 is detected at 648 nm and Peak 2 at 660 nm. The columns correspond to Stokes parameters S_1, S_2, S_3; S_0 is equal to 1. The values shown are rounded off to four decimal places, but the calculations are performed using results with 16 significant figures.

We then calculate the dot product of the normalized vectors, and find the overlap using Eq. (56). We obtain an over lap of 0.942, which is close to 1, meaning the Stokes vectors of the two peaks are close to being aligned. This

suggests that the two signal photons observed are likely to have the same polarization.
Combining this result with the pump polarization dependence of each peak in Fig. 27, it seems we are detecting two SFWM processes with orthogonal pump polarization. In addition, because the two signal photons have an overlap close to 1, at least one of the two generated photons from the two pairs have the same polarization. We are able to eliminate many allowed phasematching processes to satisfy both requirements and also to generate photons at wavelengths close to the ones we observed. The two candidates we found that are most likely to have generated the photons observed have phasematching equations *y-odd* + *y-odd* → *x-odd* + *x-odd* and *x-even* + *x-even* → *x-even* + *x-even*. The plots for these two phasematching processes are shown in Figs. 8 and 9, as well as Figs. 34 and 37 in the appendix. These two processes occur at orthogonal pump polarizations, and both have an x-polarized signal photon. They produce photon pairs at 668.75 nm and 995.34 nm, and 680.01 nm and 971.34 nm, respectively. The wavelength separation between the two predicted signal peaks is 11.26 nm, while the measured separation is about (660 - 648) nm = 12 nm, which shows fairly good agreement.

5.5 Conclusion

In summary, in this chapter we examine different aspects of the experimental design, and present the experimental data of the two SFWM peaks generated in our 1 μm microcoupler. This is the first observation of SFWM in such a microcoupler structure.

In order to get more information about the polarization of the generated photon pairs, we performed single-photon polarization tomography on each of the two signal photon peaks. At the time of writing we could not separate the two idler photons, both of which are at wavelengths above 1 μm where the detectors have low efficiency. So instead of finding the overlap between the signal and idler photons, we calculated the overlap between the two observed peaks. This would allow us to see whether the two signal photons from different processes have the same polarization, or orthogonal polarization. We defined an overlap parameter to measure the difference between the two polarization states, and obtained an overlap of 0.942, suggesting the two signal photons are of the same polarization. In addition, we found the two signal photons seem to have different pump-polarization dependence. The pump polarization for which the two signal peaks reach maxima are 48 degrees apart. This suggests we have one phasematching process with or-

thogonal pump photons, and the other process with both pump photons in the same polarization.

More experimental data is needed to conclude exactly which of the 28 phasematching processes led to the observed photons. Some immediate next steps include doing single-photon tomography using optimized APD coincidence counts, and checking the pump polarization dependence of the idler peaks.

6 Conclusion and future work

6.1 Conclusion

In this thesis project we have fabricated, simulated, and tested a novel fiber-based device called a microcoupler. We are interested in using it as a SFWM photon source for integrated optics, with the ultimate goal of creating an efficient source of entangled photon pairs for quantum waveguide networks. The main advantage of the structure is it supports four modes in the polarization and spatial mode degrees of freedom, which meets the minimum requirement for entanglement. Supporting more modes also allows for more phasematching processes. In theory the structure supports 28 phasematching processes. We used numerical simulations to predict the frequencies of the generated SFWM photons for these processes. We presented the first observation of SFWM photons in this structure and analyzed the polarization of the detected photons.

6.2 Suggestions for future work

At the time of writing more experiments are being performed on the microcoupler. We also varied the microcoupler core diameter in our numerical simulations, to see how much the predicted photon frequencies would change, We are also interested in finding out whether a different core size would allow for more entanglement between simultaneously occurring phasematching processes. For future work it might be worth changing the core diameter when fabricating a new microcoupler, which could allow for entanglement as well as more photon pairs being generated simultaneously at locations that are easy to detect. When increasing the diameter, we ran into the issue of the 7 μm microcoupler requiring too much input power. It is possible to splice specially-made high power fiber connectors to the new coupler with core diameters larger than 1 μm to prevent the input port from burning.

In terms of the microcoupler design, it is also of interest to improve the fabrication process for the future. Since we ignored the transition region on either end of the uniform interaction region in the microcoupler in our simulations, it would be more accurate to smoothen the transition region during the tapering process. Having a lot of additional fiber before the uniform interaction region can also lead to issues such as pump pulse dispersion and rotation of the pump polarization. If we could reduce the length of the additional fiber (such as with a different fiber splicing technique), that should also improve our results.

Appendix A

Phasematching plots for the 1 μm-diameter microcoupler

In this appendix we present all of the phasematching solutions from simulation results for the microcoupler 1.0 μm in diameter. Out of the 28 phasematching processes allowed (shown in Chapter 2.4.1), 21 cases have solutions at this diameter. Out of these cases, six processes generate photon pairs at wavelengths we can detect in the lab using a pump laser at 800 nm. We show all of the 21 cases here for comparison. They are divided into groups based on the polarization of the four photons involved in SFWM: 1) all four photons are x-polarized; 2) all four photons are y-polarized; 3) the two pump photons are y-polarized, while the signal and idler photons are x-polarized; 4) the two pump photons are x-polarized, while the signal and idler photons are y-polarized; 5) the two pump photons are orthogonally polarized, the signal and idler photons are also orthogonally polarized.

For each plot, we present the phasematching equation, highlight solutions at the 800 nm pump wavelength if they exist, and briefly describe the unique features of the plot. For all of the phasematching plots shown, the grey vertical line marks the 800 nm pump wavelength. The horizontal axis shows the pump frequency, multiplied by 10^{15} Hz. The vertical axis shows the splitting $\Delta\omega$ between the pump and the generated photon, also multiplied by 10^{15} Hz. All the plots are symmetric over the horizontal line of $\Delta\omega = 0$. On this line, the splitting between the signal or idler frequencies and the pump frequency is zero.

All four photons are y-polarized

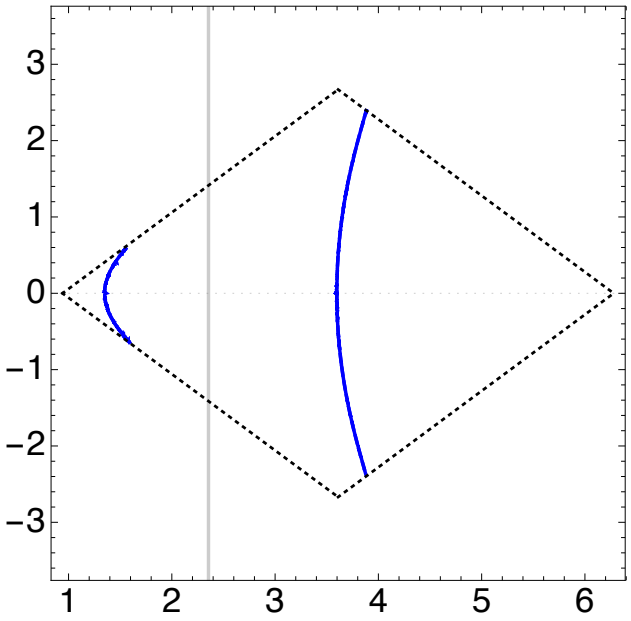

Figure 29: The phasematching equation is y-odd + y-odd → y-odd + y-odd. The curve representing the solutions are two separated arcs along the vertical direction, with different curvatures. There are no solutions at the pump wavelength of 800 nm for this process.

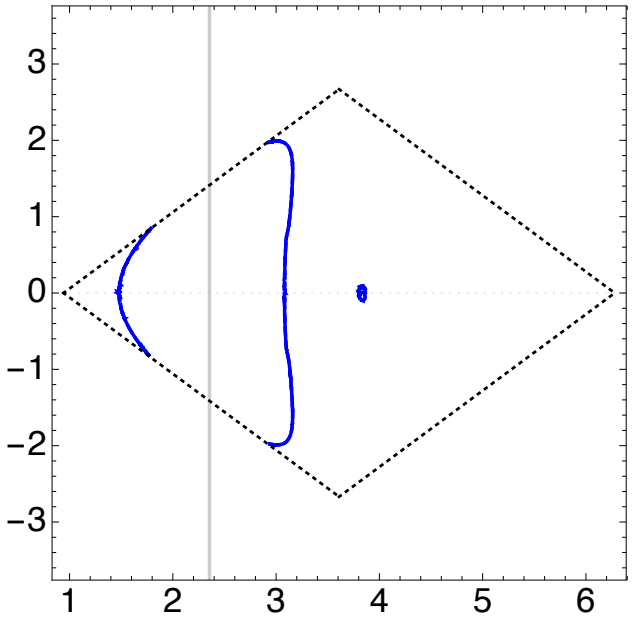

Figure 30: The phasematching equation is y-even + y-even → y-even + y-even. The plot representing the solutions consists of two curved lines along the vertical direction which are disconnected within the simulation region. There are also two small circles symmetric over the line representing $\Delta\omega = 0$, or zero splitting between the pump and the signal or idler wavelengths.There are no solutions at the pump wavelength of 800 nm for this process.

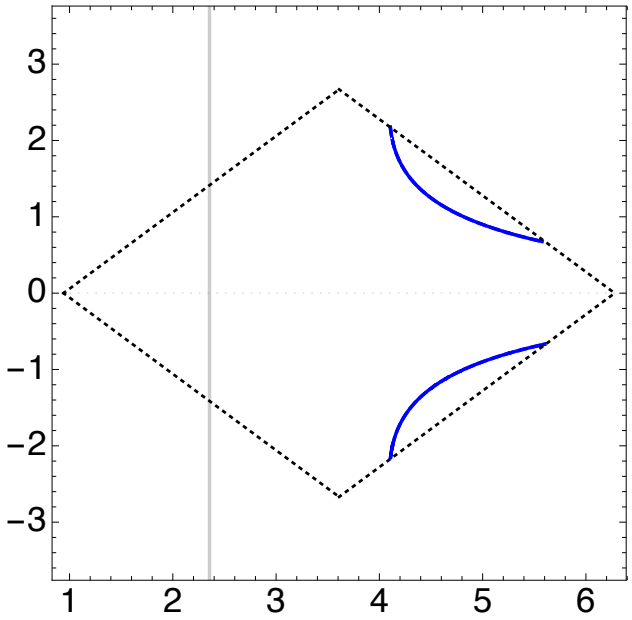

Figure 31: There is no solution at the pump wavelength of 800 nm for this process. The phasematching equation is y-even + y-even → y-odd + y-odd. The plot representing the solutions consists of two disconnected arcs rotated from vertical direction, near the maximum pump frequency.

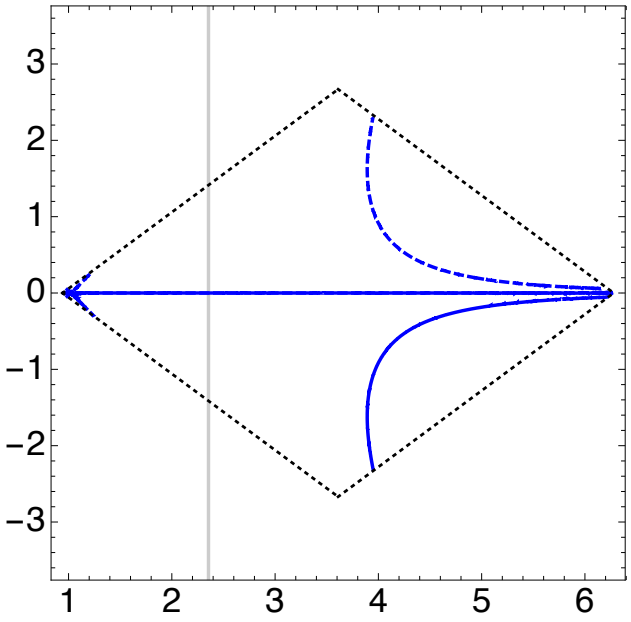

Figure 32: The phasematching equation is y-odd + y-even → y-even + y-odd. The plot has an arrow-like shape at the minimum pump frequency within the simulation region. There are also two large arcs spanning close to half of the pump frequency range. There are solutions for 800 nm pump on the horizontal line representing $\Delta\omega = 0$*. The signal and idler photons on this line would be at the same wavelength as the pump photon, so we cannot observe them.*

All four photons are x-polarized

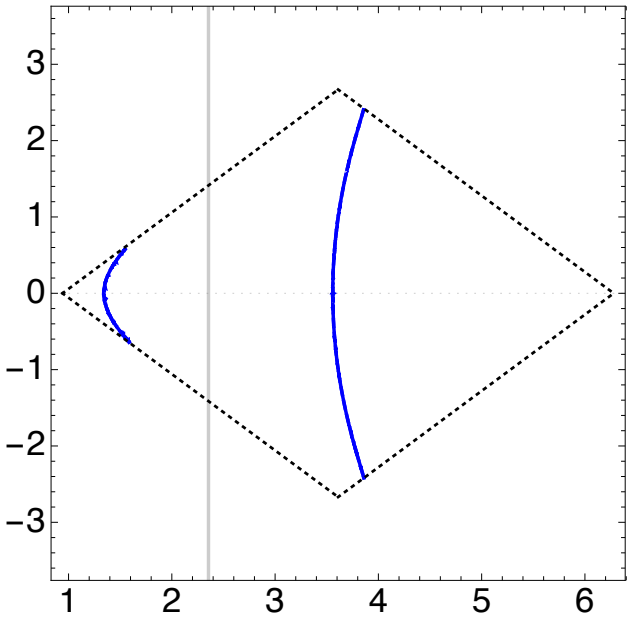

Figure 33: The phasematching equation is x-odd + x-odd → x-odd + x-odd. The plot representing the solutions consists of two separated arcs along the vertical direction, with different curvatures. The plot has the same shape as the first case, Fig. 29, where all four photons are of mode y-odd. There are no solutions at a pump wavelength of 800 nm.

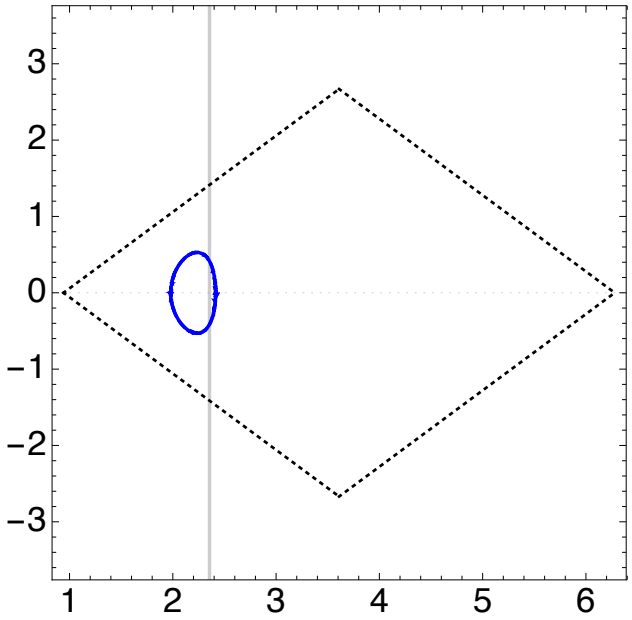

Figure 34: This is one of the six cases with solutions at a pump wavelength of 800 nm. The four modes involved in this phasematching process are all x-even. The phasematching equation is x-even + x-even → x-even + x-even. The curve representing the solutions is a lopsided ellipse that crosses the vertical line of the 800 nm pump twice. The two solutions are: $\lambda_s = 680.01$ nm and $\lambda_s = 971.34$ nm. The prediction of this photon pair is promising because the two photons are at wavelengths far away enough from the pump, and are still within the detection range. In fact this is one of two cases matching our experimental result most closely in wavelength.

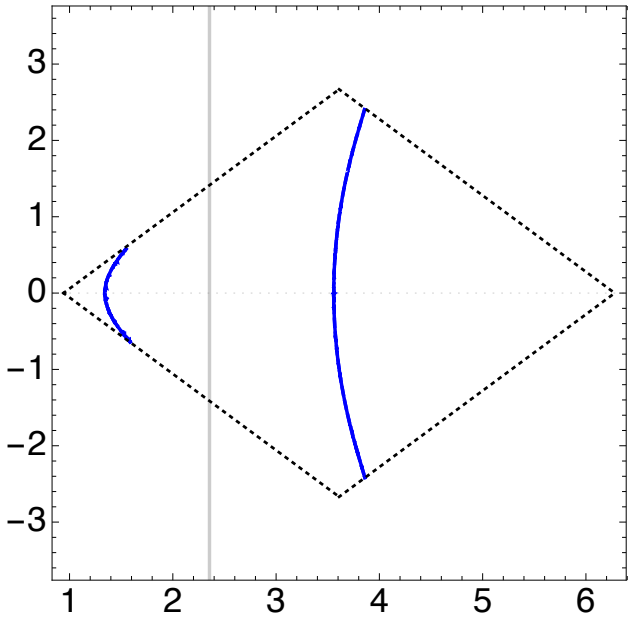

Figure 35: The phasematching equation is x-even + x-even → x-odd + x-odd. The plot representing the solutions consists of two disconnected arcs rotated from the vertical direction, near the maximum pump frequency. It has the same shape as the earlier case, Fig. 31, where the phasematching equation is y-even + y-even → y-odd + y-odd. Again, there are no solutions for the 800 nm pump.

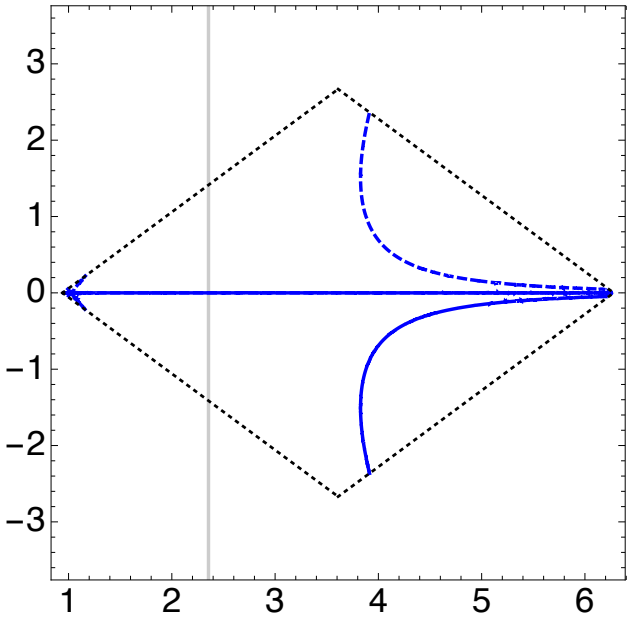

Figure 36: The phasematching equation is x-odd + x-even → x-even + x-odd. The plot has an arrow-like shape at the minimum pump frequency within the simulation region. There are also two large arcs spanning close to half of the pump frequency range. There are solutions on the horizontal line representing $\Delta\omega = 0$. The signal and idler photons on this line would be at the same wavelength as the pump photon, so we cannot observe them. The plot resembles Fig. 32, which has the same spatial modes but opposite polarization. There are no solutions at the pump wavelength of 800 nm for this process.

Pump photons are y-polarized, generated photons are x-polarized

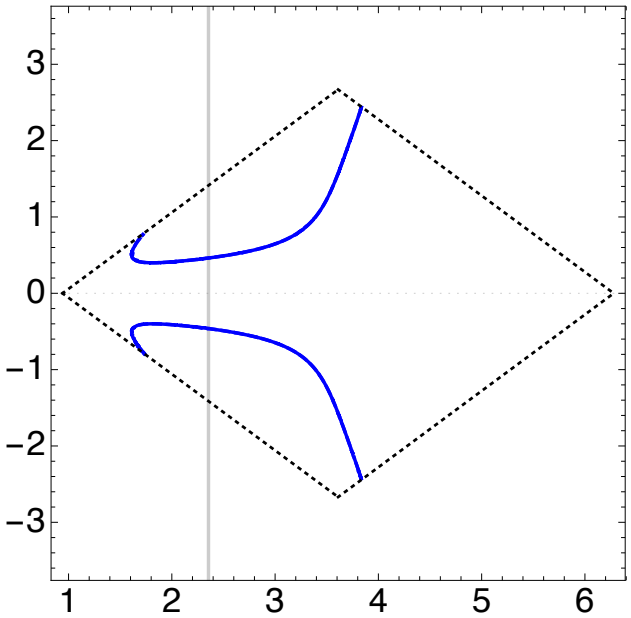

Figure 37: This is the second one of the six cases with solutions at a pump wavelength of 800 nm. The phasematching equation is y-odd + y-odd → x-odd + x-odd. The curve that includes all the solutions map out a wing-like shape symmetric over the $\Delta\omega = 0$ horizontal line. The two shapes are closer together at lower pump frequency and move away from each other at higher frequency. The two solutions are: $\lambda_s = 668.75\ nm$ and $\lambda_s = 995.34\ nm$. The two predicted photons are at wavelengths far away enough from the pump, and are also within the detection range. This is another case where the predicted photons match our experimental result closely.

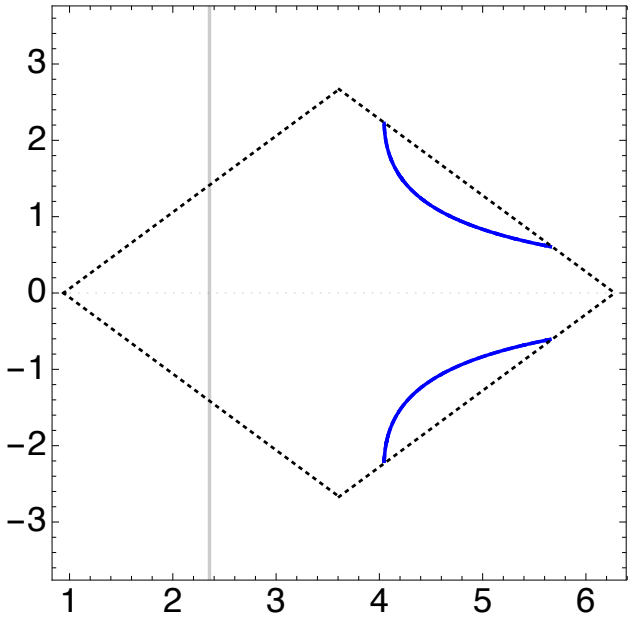

Figure 38: The phasematching equation is y-even + y-even → x-odd + x-odd. The plot representing the solutions consists of two disconnected arcs rotated from the vertical direction, near the maximum pump frequency. The shape of the plot resembles that of Fig. 31, which also has the pump photons in the even mode and the generated photons in the odd mode. There are no solutions at the pump wavelength of 800 nm for this process.

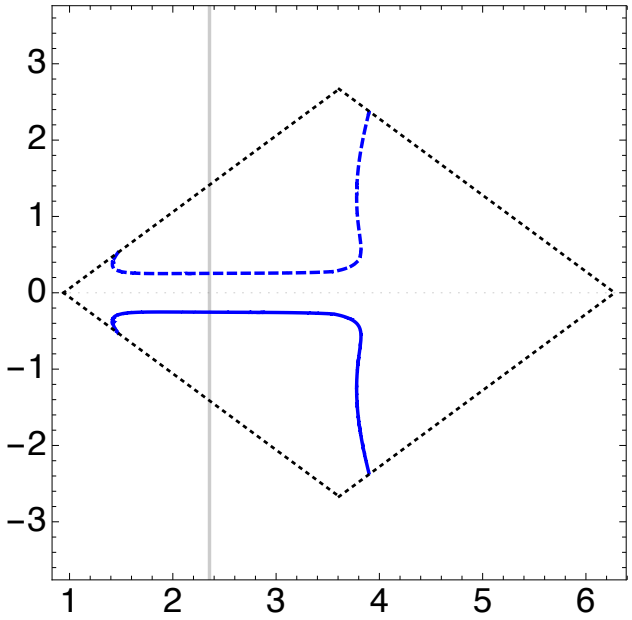

Figure 39: This is the third one of six cases with solutions at the pump wavelength of 800 nm. The phasematching equation is y-odd + y-even → x-even + x-odd. The curve representing the solutions has a set of parallel horizontal line segments, before curving away from the symmetry axis of $\Delta\omega = 0$. The parallel horizontal lines each crosses the vertical line of the 800 nm pump. The two solutions are: $\lambda_s = 722.06\ nm$ and $\lambda_s = 896.81\ nm$. The two predicted photons are at wavelengths far away enough from the pump, and are also within the detection range. We do not detect this photon pair, but this phasematching process is still a candidate if we consider changing the diameter of the microcoupler.

Pump photons are x-polarized, generated photons are y-polarized

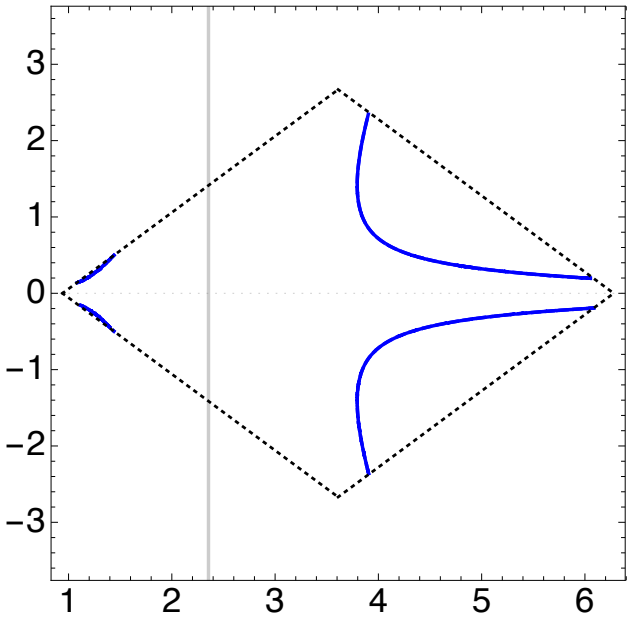

Figure 40: The phasematching equation is x-odd + x-odd → y-odd + y-odd. The plot representing the solutions has two parts within the simulation domain: a symmetric pair of curved lines near the lower limit of the pump frequency, and two symmetric L-shaped curves that approach each other as pump frequency increases. There are no solutions at the pump wavelength of 800 nm for this process.

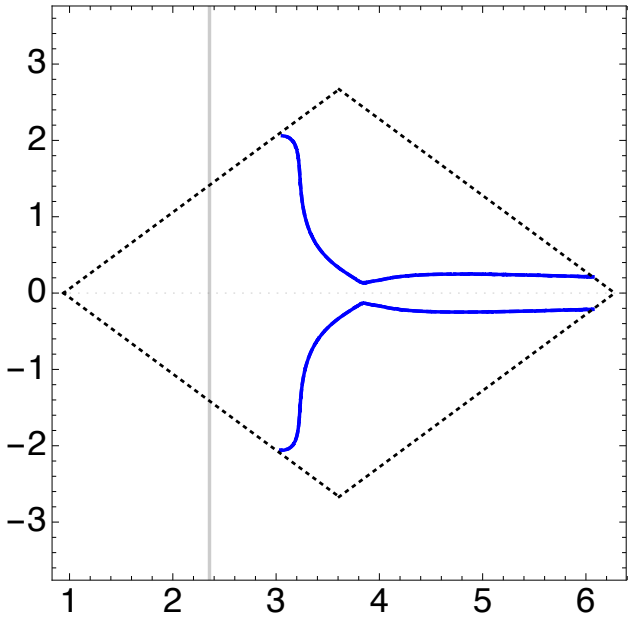

Figure 41: The phasematching equation is x-even + x-even → y-even + y-even. The plot representing the solutions are two symmetric curves with a sharp turn near $\omega_p = 3.5 \times 10^{15}\ Hz$. *The splitting* $\Delta\omega$ *is much smaller at the higher-frequency side of the turning point, and the two curves are close to parallel at the upper frequency limit. There are no solutions at the pump wavelength of 800 nm for this process.*

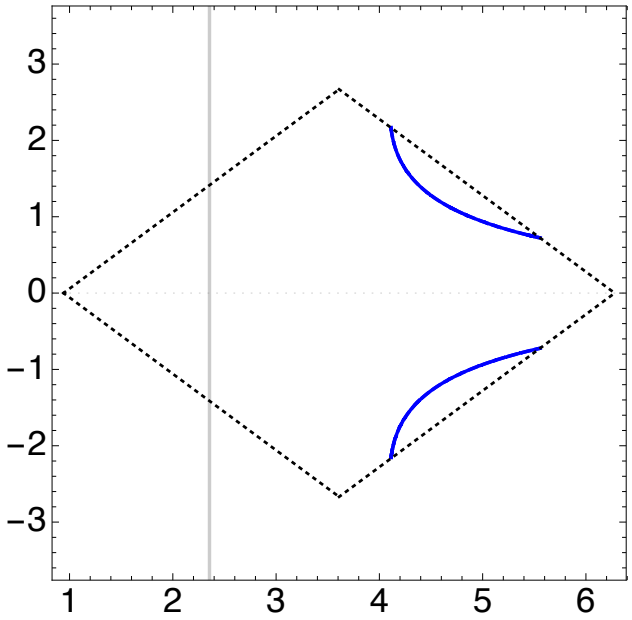

Figure 42: The phasematching equation is x-even + x-even → y-odd + y-odd. The plot representing the solutions consists of two disconnected arcs rotated from the vertical direction, near the maximum pump frequency. The shape of the plot resembles that of Fig. 35, as well as Figs. 31 and 38. There are no solutions at the pump wavelength of 800 nm for this process.

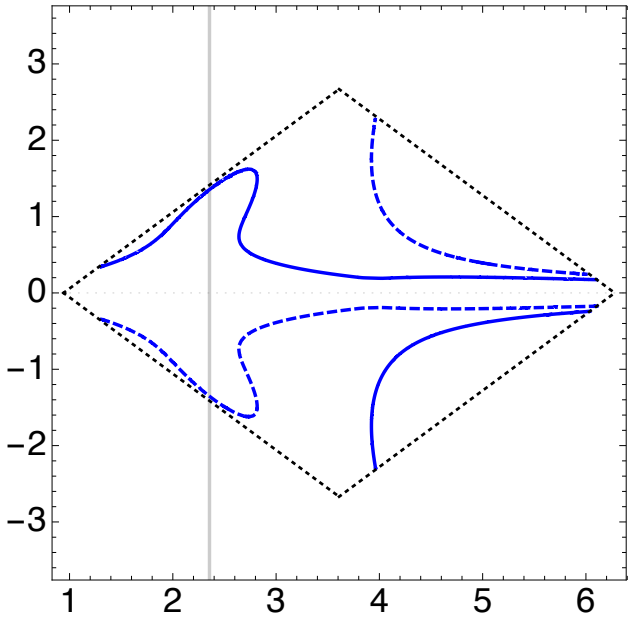

Figure 43: This is the fourth case with 2 solutions at a pump wavelength of 800 nm. The phasematching equation is x-odd + x-even → y-even + y-odd. The plot consists of four curves, making an arrow-like shape on the lower-frequency end, and two symmetric arcs spanning from $\omega_p = 4 \times 10^{15}\ Hz$ *to* $6 \times 10^{15}\ Hz$*. The solutions are:* $\lambda_s = 786.18\ nm$ *and* $\lambda_s = 814.32\ nm$*. These two generated photons are likely too close to the pump spectrum, and would be filtered out by the notch filters we use to block the pump.*

Pump photons are orthogonally polarized, generated photons are orthogonally polarized

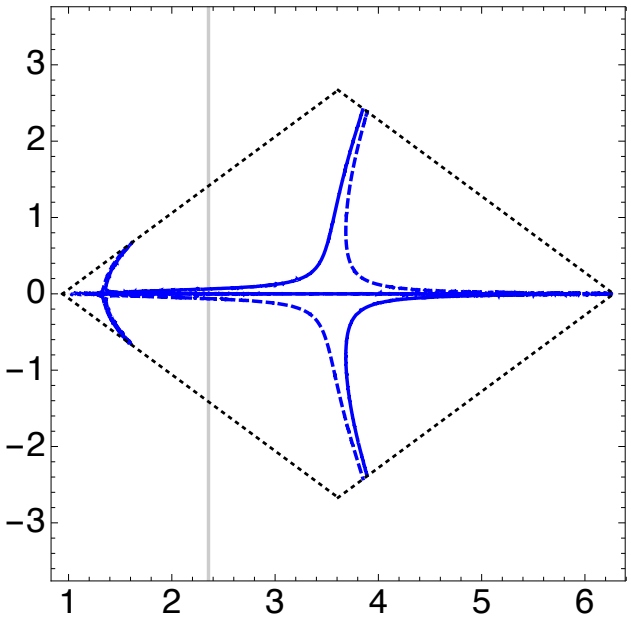

Figure 44: This is the fifth case with 2 solutions at a pump wavelength of 800 nm. The phasematching equation is y-odd + x-odd → x-odd + y-odd. The solutions are: $\lambda_s = 778.75\ nm$ *and* $\lambda_s = 822.44\ nm$*. The frequency splitting between the pump and the generated photons are very small for most of the plot, but the splitting increases rapidly from* $\omega_p = 3.5$ *to* $4 \times 10^{15}\ Hz$*. These two generated photons are likely too close to the pump spectrum, and would be filtered out by the notch filters we use to block the pump.*

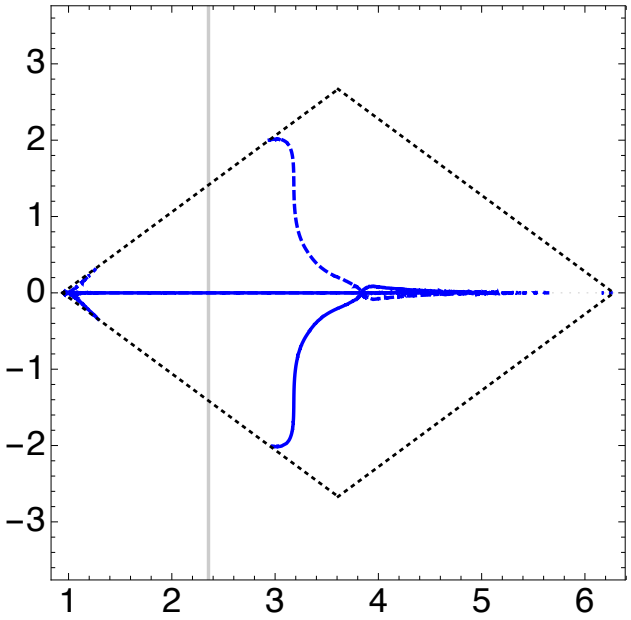

Figure 45: The phasematching equation is y-even + x-even → x-even + y-even. The shape of the plot has three main parts. The first part is a small pair of symmetric line segments at the boundary of the simulation region, on the lower frequency side. These lines make an arrow with the second part, which is a horizontal line overlapping with the $\Delta\omega = 0$ line. The third part has two symmetric curves intersecting at $\omega_p = 3.5 \times 10^{15}$ Hz, with large splitting values before the intersection and splitting $\Delta\omega < 0.2 \times 10^{15}$ Hz after the intersection. There are no solutions at a pump wavelength of 800 nm.

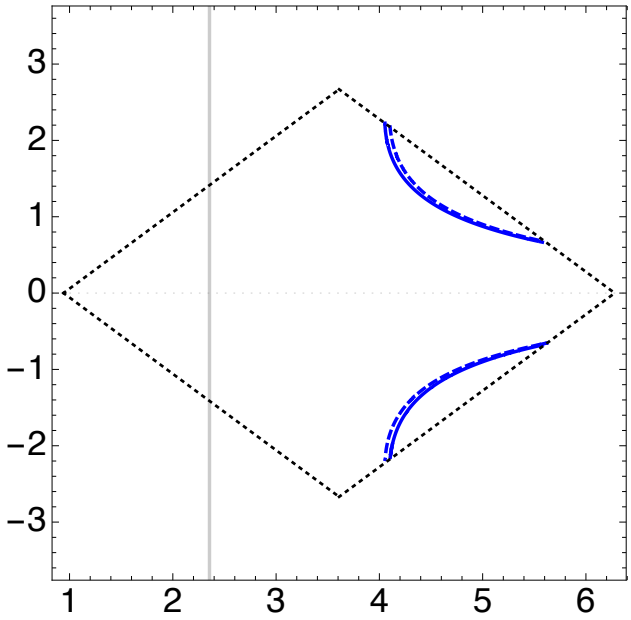

Figure 46: The phasematching equation is y-even + x-even → x-odd + y-odd. The plot representing the solutions consists of two sets of disconnected arcs rotated from the vertical direction, near the maximum pump frequency. One set of symmetric arcs has a slightly smaller radius of curvature. There are no solutions at a pump wavelength of 800 nm.

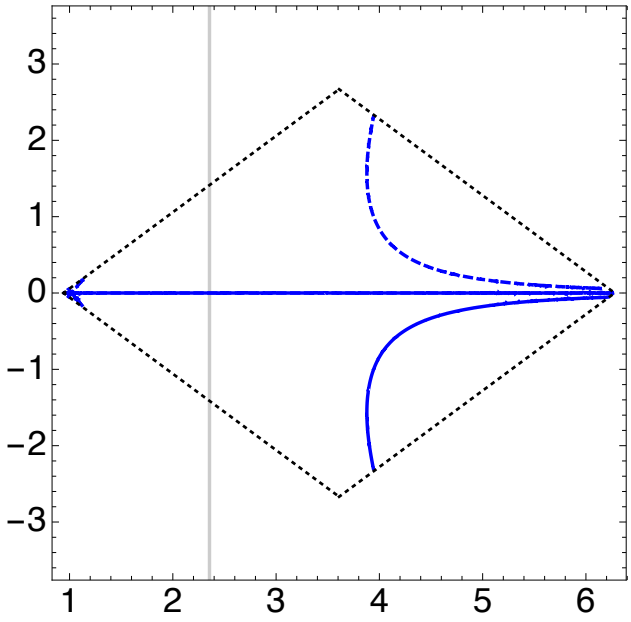

Figure 47: The phasematching equation is y-odd + x-even → x-even + y-odd. The plot has an arrow-like shape at the minimum pump frequency within the simulation region. There are also two large arcs spanning close to half of the pump frequency range. There are solutions on the horizontal line representing $\Delta\omega = 0$. The shape of this plot resembles those of Figs. 32 and 36. There are no solutions at the pump wavelength of 800 nm.

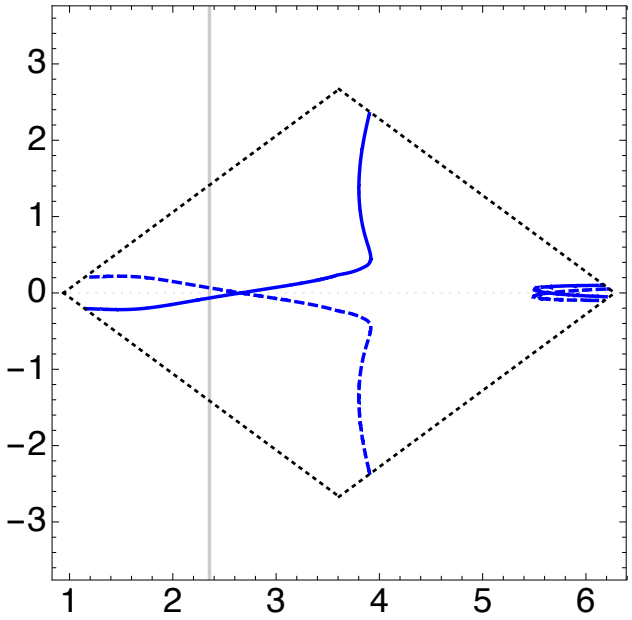

Figure 48: This is the sixth case with 2 solutions at a pump wavelength of 800 nm. The phasematching equation is y-odd + x-even → x-odd + y-even. The solutions are: $\lambda_s = 777.98\ nm$ and $\lambda_s = 823.31\ nm$. The curves that all the possible solutions lie on intersect twice in the simulation region. The frequency splittings between the pump and the generated photons changes rapidly near $\omega_p = 4$. The two generated photons in the solution for 800 nm pump are too close to the pump spectrum, and are filtered out by the notch filters.

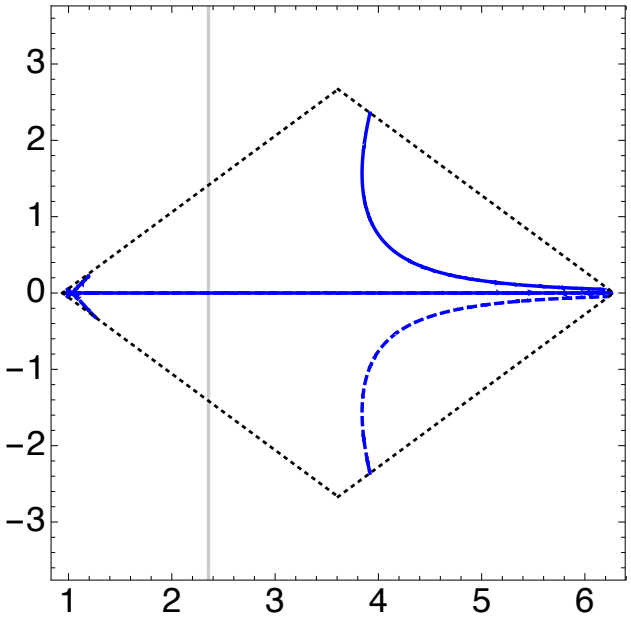

Figure 49: The phasematching equation is y-even + x-odd → x-odd + y-even. The plot has an arrow-like shape at the minimum pump frequency within the simulation region. There are also two large arcs spanning close to half of the pump frequency range. There are solutions on the horizontal line representing $\Delta\omega = 0$. The shape of this plot resembles those of Figs. 32, 36, and 47. There are no solutions at a pump wavelength of 800 nm.

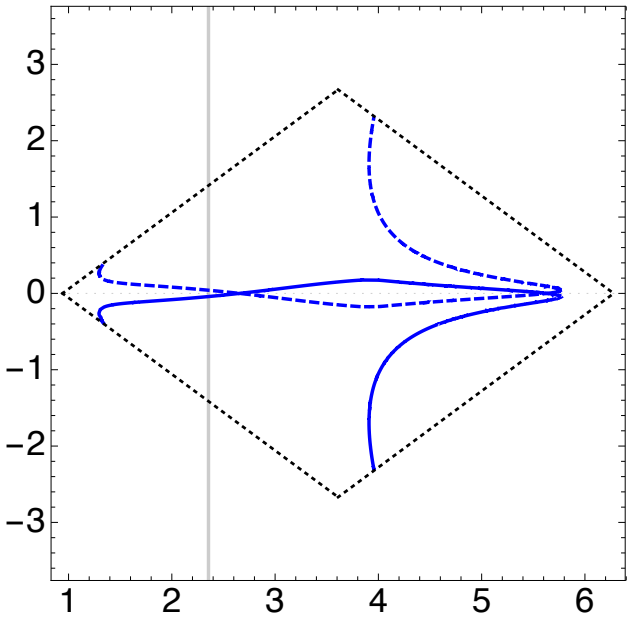

Figure 50: This is the seventh case with 2 solutions at a pump wavelength of 800 nm. The solutions are: $\lambda_s = 786.18$ nm and $\lambda_s = 814.32$ nm. The phase-matching equation is y-even + x-odd $\rightarrow$ x-even + y-odd. The solid and dashed curves that map out all the signal and idler photon locations at different pump frequencies intersect twice. The two regions overlap over an elongated region with a small frequency splitting and over a large range of pump frequency. They cross the 800 nm pump line near the first intersection point at low pump frequency. These two generated photons are too close to the pump spectrum, and are filtered out by the notch filters.

References

[1] J. C. F. Matthews, A. Politi, A. Stefanov, and J. L. O'Brien. Manipulation of multiphoton entanglement in waveguide quantum circuits. *Nat. Photon.*, 3(6):346–350, 2009.

[2] J. W. Silverstone, D. Bonneau, K. Ohira, N. Suzuki, H. Yoshida, N. Iizuka, M. Ezaki, C. M. Natarajan, M. G. Tanner, R. H. Hadfield, V. Zwiller, G. D. Marshall, J. G. Rarity, J. L. O'Brien, and M. G. Thompson. On-chip quantum interference between silicon photon-pair sources. *Nat Photon*, 8(2):104–108, 2014.

[3] B. J. Smith, P. Mahou, O. Cohen, J. S. Lundeen, and I. A. Walmsley. Photon pair generation in birefringent optical fibers. *Optics Express*, 17(26):23590–23602, 2009.

[4] D. J. Wineland, C. Monroe, W. M. Itano, D. Leibfried, B. E. King, and D. M. Meekhof. Experimental issues in coherent quantum-state manipulation of trapped atomic ions. *J. Res. Natl. Inst. Stand. Technol.*, 103(3):259–328, 1998.

[5] D. J. Wineland and R. Blatt. Entangled states of trapped atomic ions. *Nature*, 453:1008–1014, 2008.

[6] R. Hanson, L. P. Kouwenhoven, J. R. Petta, S. Tarucha, and L. M. K. Vandersypen. Spins in few-electron quantum dots. *Rev. Mod. Phys.*, 79:1217–1265, 2007.

[7] Y. Nakamura, Yu. A. Pashkin, and J. S. Tsai. Coherent control of macroscopic quantum states in a single-cooper-pair box. *Nature*, 398:786–788, 1999.

[8] E. Knill, R. Laflamme, and G. J. Milburn. A scheme for efficient quantum computation with linear optics. *Nature*, 409(46-52), 2001.

[9] J. W. Silverstone, D. Bonneau, J. L. O'Brien, and M. G. Thompson. Silicon quantum photonics. *IEEE J. Sel. Top. Quantum Electron.*, PP(99), May 2016.

[10] K. Garay-Palmett, H. J. McGuinness, Offir Cohen, J. S. Lundeen, R. Rangel-Rojo, A. B. U'Ren, M. G. Raymer, C. J. McKinstrie, S. Radic, and I. A. Walmsley. Photon pair-state preparation with tailored spectral properties by spontaneous four-wave mixing in photonic-crystal fiber. *Optics Express*, 15(22):14870–14886, 2007.

[11] A. Politi, J. C. F. Matthews, M. G. Thompson, and J. L. O'Brien. Integrated quantum photonics. *IEEE J. Sel. Top. Quantum Electron.*, pages 1–12, 2009.

[12] T. D. Ladd, F. Jelezko, R. Laflamme, Y. Nakamura, C. Monroe, and J. L. O'Brien. Quantum computers. *Nature*, 464(4):45–53, March 2010.

[13] B. J. Eggleton, C. Kerbage, P. S. Westbrook, R. S. Windeler, and A. Hale. Microstructured optical fiber devices. *Opt. Express*, 9(13):698–713, 2001.

[14] J. G. Rarity, J. Fulconis, J. Duligall, W. J. Wadsworth, and P. St. J. Russell. Photonic crystal fiber source of correlated photon pairs. *Optics Express*, 13(2):534–544, 2005.

[15] Q. Lin and G. P. Agrawal. Silicon waveguides for creating quantum-correlated photon pairs. *Optics Letters*, 31(21):3140–3142, 2006.

[16] C. Söller, O. Cohen, B. J. Smith, I. A. Walmsley, and C. Silberhorn. High-performance single-photon generation with commercial-grade optical fiber. *Phys. Rev. A.*, 83, 2011.

[17] K. Garay-Palmett, D. Cruz-Delgado, F. Dominguez-Serna, E. Ortiz-Ricardo, J. Monroy-Ruz, H. Cruz-Ramirez, R. Ramirez-Alarcon, and A. B. U'Ren. Photon-pair generation by intermodal spontaneous four-wave mixing in birefringent, weakly guiding optical fibers. *Phys. Rev. A.*, 93(3):033810, March 2016.

[18] E. Meyer-Scott, V. Roy, J-P. Bourgoin, B. L. Higgins, L. K. Shalm, and T. Jennewein. Generating polarization-entangled photon pairs using cross-spliced birefringent fibers. *Optics Express*, 21(5):6205–6212, 2013.

[19] C. Xiong, C. Monat, A. S. Clark, C. Grillet, G. D. Marshall, M. J. Steel, J. Li, L. O'Faolain, T. F. Krauss, J. G. Rarity, and B. J. Eggleton. Slow-light enhanced correlated photon pair generation in a silicon photonic crystal waveguide. *Opt. Lett.*, 36(17):3413–3415, Sep 2011.

[20] D. Cruz-Delgado, J. Monroy-Ruz, A. M. Barragan, E. Ortiz-Ricardo, H. Cruz-Ramirez, R. Ramirez-Alarcon, K. Garay-Palmett, and A. B. U'Ren. Configurable spatiotemporal properties in a photon-pair source based on spontaneous four-wave mixing with multiple transverse modes. *Opt. Lett.*, 39(12):3583–3586, June 2014.

[21] D. Cruz-Delgado, R. Ramirez-Alarcon, E. Ortiz-Ricardo, J. Monroy-Ruz, F. Dominguez-Serna, H. Cruz-Ramirez, K. Garay-Palmett, and A. B. U'Ren. Fiber-based photon-pair source capable of hybrid entanglement in frequency and transverse mode, controllably scalable to higher dimensions. *Scientific Reports*, 6, June 2016.

[22] I. Jizan, L. G. Helt, C. Xiong, M. J. Collins, D.-Y. Choi, C. J. Chae, M. Liscidini, M. J. Steel, B. J. Eggleton, and A. S. Clark. Bi-photon spectral correlation measurements from a silicon nanowire in the quantum and classical regimes. *Scientific Reports*, 5, 2015.

[23] M. A. Ciampini, A. Orieux, S. Paesani, F. Sciarrino, G. Corrielli, A. Crespi, R. Ramponi, R. Osellame, and P. Mataloni. Path-polarization hyperentangled and cluster states of photons on a chip. *Light: Science and Applications*, 5, 2016.

[24] L. Sansoni, K. H. Luo, C. Eigner, R. Ricken, V. Quiring, H. Herrmann, and C. Silberhorn. A two-channel, spectrally degenerate polarization entangled source on chip. *arXiv*, (1604.03430v2), 2016.

[25] A. Yariv and P. Yeh. *Photonics: Optical Electronics in Modern Communications*. Oxford University Press, sixth edition, 2006.

[26] O. Cohen. *Generation of uncorrelated photon-pairs in optical fibers*. PhD thesis, University of Oxford, 2009.

[27] G. P. Agrawal. *Nonlinear Fiber Optics*. Academic Press, fifth edition, 2012.

[28] R. W. Boyd. *Nonlinear Optics*. Academic Press, third edition, 2008.

[29] Peter W. Milonni and Joseph H. Eberly. *Laser Physics*. Wiley, second edition, 2010.

[30] R. H. Stolen, M. A. Bösch, and Chinlon Lin. Phase matching in birefringent fibers. *Opt. Lett.*, 6(5):213–215, 1981.

[31] C. Baker and M. Rochette. A generalized heat-brush approach for precise control of the waist profile in fiber tapers. *Opt. Mater. Express*, 1(6):1065–1076, October 2011.

[32] W.-P. Huang. Coupled-mode theory for optical waveguides: an overview. *J. Opt. Soc. Am. A*, 11(3):963–983, 1994.

[33] K. Yasumoto. Coupled-mode analysis of two-parallel circular dielectric waveguides using a singular perturbation technique. *Journal of Lightwave Technology*, 12(1):74–81, 1994.

[34] W. Żakowicz. Two coupled dielectric cylindrical waveguides. *J. Opt. Soc. Am. A*, 14(3):580–587, 1997.

[35] Chinlon Lin, W. A. Reed, H.-T. Shang, and A. D. Pearson. Phase matching in the minimum-chromatic-dispersion region of single-mode fibers for stimulated four-photon mixing. *Opt. Lett.*, 6(10):493–495, October 1981.

[36] E. Merzbacher. *Quantum Mechanics*. Wiley, third edition, December 1997.

[37] R. H. Stolen and J. E. Bjorkholm. Parametric amplification and frequency conversion in optical fibers. *IEEE J. Quantum Electron.*, 18(7):1062, 1982.

[38] O. Cohen, J. S. Lundeen, B. J. Smith, G. Puentes, P. J. Mosley, and I. A. Walmsley. Tailored photon-pair generation in optical fibers. *Phys. Rev. Lett.*, 102, 2009.

[39] V. O. Lorenz, B. Fang, and O. Cohen. Generation of polarization-entangled photons in a standard polarization-maintaining fiber. *Journal of Physics: Conference Series*, 414(1):012007, 2013.

[40] J. E. Sharping, K. F. Lee, M. A. Foster, A. C. Turner, B. S. Schmidt, M. Lipson, A. L. Gaeta, and P. Kumar. Generation of correlated photons in nanoscale silicon waveguides. *Optics Express*, 14(25):12388–12393, 2006.

[41] J. L. O'Brien. Optical quantum computing. *Science*, 318:1567–1570, December 2007.